Hybrid Energy Harvesting System for a Condition Monitoring Mote

D.J. de Villiers

Supervisor: Dr R.H. Wilkinson
Co-supervisor: S. Kaplan
Centre for Instrumentation Research

Submitted in fulfilment of the
requirements for the
degree of Magister Technologiae
in the Department of Electrical Engineering

Cape Peninsula University of Technology
Cape Town

© June 2009

Declaration

I, Daniel de Villiers, declare that the contents of this thesis represent my own unaided work, and that the thesis has not previously been submitted for academic examination towards any qualification. Furthermore, it represents my own opinions and not necessarily those of the Centre for Instrumentation Research and Cape Peninsula University of Technology.

Signature of author ....

Cape Town

Acknowledgements

The completion of this thesis would not have been possible without the support, inspiration and encouragement of the following people and groups:

Synopsis

Traditional high voltage power transformers feature sensors measuring basic parameters from oil and gas and are limited to on-site monitoring. Unforeseen failures and breakdowns on these transformers have led to extensive financial losses even with planned maintenance schedules in place. A distinct need has arisen to actively monitor and identify causes of such failures. However, no or little infrastructure exists for effective remote condition monitoring.

Wireless sensor networks can be introduced to actively monitor and identify causes of such failures. Sensor motes in the network are battery operated and therefore constrained by limited energy in these batteries. An alternative to battery-powered sensor motes is the conversion of available energy harvested from the surrounding environment into useable electrical energy powering the sensor motes.

The primary objective of this research was to examine methods to harvest energy from both the environment and high voltage power transformer. A low cost and feasibly sized hybrid energy harvesting power management prototype was successfully developed that enabled sustained sensor mote operation for prolonged condition monitoring of high voltage transformers.

The sensor mote utilised a piezoelectric cantilever to generate usable electrical energy from the transformer tank vibration. Together with solar energy harvesting, the system allowed for a battery-less self-sustained wireless sensor mote capable of autonomously monitoring its surroundings.

The power management system's modular architecture provided for the inclusion of additional energy harvesting techniques. This allowed condition monitoring solutions not exclusively for power transformers but proposed an extensible condition monitoring solution for various applications.

List of Abbreviations

ADC - Analogue to Digital Converter

DLC - Double Layer Capacitor

DMFC - Direct Methanol Fuel Cell

DoD - Depth of Discharge

DUT - Device Under Test

EHS - Energy Harvesting System

ESR - Equivalent Series Resistance

FFT - Fast Fourier Transform

IEEE - Institute of Electrical and Electronics Engineers

IP - Ingress protection

LDO - Low-Dropout

Li-ion - Lithium-ion

Li-Po - Lithium-Polymer

MPPT - Maximum Power Point Tracking

NiCd - Nickel-Cadmium

NiMH - Nickel-Metal Hydride

PD - Partial Discharge

PFC - Piezoelectric Fiber Composites

PMS - Power Management System

PV - Photovoltaic

RF - Radio Frequency

SCA - Storage Capacitor Array

SEH - Solar Energy Harvesting

VEH - Vibration Energy Harvesting

WSM - Wireless Sensor Mote

WSN - Wireless Sensor Network

Contents

List of Figures

List of Tables

Chapter 1

Introduction

1.1 Background

Large high voltage power transformers are used in distribution networks. Such transformers represent a large portion of capital investment in transmission and distribution substations. Taking these power transformers out of service for unexpected maintenance or repairs is extremely expensive. It is therefore essential to install a condition monitoring system to predict failures and imminent fault conditions using data gathered from sensors on the transformer. Such sensors for transformer monitoring include acoustic sensors to detect partial discharge (PD) which covers corona, oil PD and surface PD events, together with vibration sensors.

1.2 Problem statement

Traditional high voltage power transformers have no or little form of remote condition monitoring let alone the ability to predict failures that might occur. Unforeseen failures and breakdowns have led to extensive financial losses even with planned maintenance schedules. A distinct need has arisen to actively monitor and identify causes of such failures on these transformers. For such a system to be realised, a wireless sensor network was proposed to allow for distributed condition monitoring of transformers. A wireless sensor network comprises of individual sensor motes that are microprocessor transceiver units with sensors interacting with one another by relaying information wirelessly.

However, wireless sensor motes (WSMs) are battery operated and therefore have a limited operating life. The replacement of depleted batteries is not always feasible often due to inaccessibility of remote and hazardous locations in which the motes are situated. As the battery is depleted, operation becomes unpredictable compromising sensor data integrity.

An alternative to battery-powered sensor motes is the use of available energy harvested from the surrounding environment. This energy can be converted through various transducers and stored as needed to permit sustainable delivery of power to the sensor mote. By enabling prolonged and predictable operation of sensor motes, reliable condition monitoring of high voltage transformers can be realised and malfunctions minimised.

1.3 Objectives of the research

The primary objective was to examine methods to harvest available energy from the environment and a high voltage power transformer. Energy from the environment such as solar radiation and wind can be harvested to power the mote. Vibration and inductive energy can be harvested from the transformer through piezoelectric materials and surrounding magnetic fields respectively.

A further objective was to examine the effectiveness of multiple energy harvesting techniques supplying power for one mote. Potential types of energy reservoirs for the mote such as batteries and supercapacitors were researched, investigating characteristics such as power densities, charge times, physical size and complexity of charge cycles. Supercapacitors as alternative energy storage devices or hybrid storage systems using both supercapacitors and batteries were examined.

With the main objectives of this project introduced, the following research questions are significant:

- What harvesting techniques can be implemented on the mote that will allow for a low cost, lightweight and feasibly sized system while maintaining reliable operation?

- What is the optimal configuration for an energy source or combination of sources for a transformer monitoring mote?

- Will the proposed power management system effectively harvest and store available energy independent from the sensor mote state (low-power, sleep or shutdown)?

- Will the proposed system's architecture allow additional energy sources to be added to the existing system?

- Will the proposed system be limited to transformer condition monitoring or could it cater for a wider application field?

As a future research objective, data from the sensor mote can be made available to the network such as existing energy, average and peak power consumptions and rate of charge from which energy efficient routing protocols can be implemented.

1.4   Research methodology

A literature search on implementing energy harvesting methods for condition monitoring of high voltage transformers was performed. This led to further investigation into different energy storage techniques such as supercapacitors and assorted battery chemistries.

A comparison between feasible harvesting techniques was made from where future recommendations and improvements were suggested. Subsequently, feasible harvesting methods relating to high voltage power transformers and their surroundings were identified from where various prototype designs were constructed. Laboratory simulations and test scenarios on these solutions were executed and the feasibility of these designs evaluated.

1.5   Delineation of the research

This research was based around energy harvesting for WSMs for condition monitoring of high voltage transformers and did not provide a generic energy harvesting solution for motes in a network. The proposed solution was also limited to the South African environment.

Although the research offered a brief comparison study of feasible energy harvesting techniques as reference, the energy harvesting techniques implemented were limited to solar radiation and vibration based energy harvesting as detailed in sections 3.9 and 3.10. The sensors used were limited to those suitable for high voltage transformer monitoring. These were typically acoustic sensors that measured partial discharge, vibration sensors and stray magnetic flux sensors.

The research was based on energy harvesting techniques on the sensor motes themselves and did not include low power and energy efficient network routing algorithms.

1.6   Significance and contributions of the research

This study offered possibly the first South African prototype wireless sensor network for high voltage transformer condition monitoring that featured energy harvesting techniques to enable sustainable network operation. Recommendations were made as to what energy harvesting method or combination of methods provided a feasible solution for high voltage transformer monitoring applications.

Since the majority of WSMs are designed to operate from batteries they are fundamentally bounded by finite quantities of energy. For a truly self-sustained WSM a replenishable energy source is essential to power the mote. This research provided a better understanding into

energy harvesting techniques for self-sustained sensor motes allowing for reliable continual transformer condition monitoring.

1.7   Structure of the thesis

The structure of the document, shown in Figure 1.1, is as follows: First, an overview of wireless sensor networks is given in chapter 2, highlighting applications, sensor motes, energy management and limitations of battery operated sensor motes.

Feasible energy harvesting techniques together with technology trends in energy reservoirs are classified in chapter 3. Chapter 4 covers vibration energy harvesting by looking into vibration characteristics, theory of output power and the selected piezoelectric generator. In chapter 5 solar energy harvesting is discussed highlighting photovoltaic fundamentals, maximum power point tracking and solar panel performance.

Chapters 6 and 7 review the hybrid power management system's architecture, design and performance from where the prototype is evaluated empirically. Finally, in chapter 8 conclusions and future recommendations are presented.

Problem statement
⇩
Objectives & research methodology

Overview of wireless sensor networks

Energy harvesting for WSNs
⇩
Investigation of potential power sources

Vibration energy harvesting (VEH)

Energy harvesting from power transformer
⇩
Piezoelectric theory & characteristics of vibration source
⇩
Generic conversion model
⇩
Model verification & output power experiments

Solar energy harvesting (SEH)

Energy harvesting from environment
⇩
PV technology & principle of power generation
⇩
Solar panel characteristics & performance
⇩
Output power experiments

Hybrid power management system design

System overview & architecture
⇩
Prototype design & layout
⇩
Prototype evaluation

VEH subsystem performance
SEH subsystem performance

Hybrid system performance

Conclusions: Assessment of initial objectives

Figure 1.1: Thesis structure

Chapter 2

Overview of Wireless Sensor Networks

A wireless sensor network (WSN) is a generic term given for a system consisting of small, low-cost sensors interacting with one another by collecting environmental data. They allow monitoring and controlling of particular surroundings from remote locations. WSNs have many applications such as environmental condition monitoring, medical and military monitoring purposes and gathering information in remote as well as hazardous locations.

2.1   Outline of WSNs

Traditionally, sensor networks consisted of only a few sensors and were typically wired to a central processing station whereas presently the attention tends more to distributed wireless sensing. Distributed sensing allows for an enhanced method to measure the phenomenon of interest more closely than a single sensor would (Bharathidasan & Ponduru, 2003).

Recent technological advances have made the development and deployment of small, low-power sensing devices that can perform local processing and communicate wirelessly possible. These wireless sensing devices are called wireless sensor motes (Bharathidasan & Ponduru, 2003). Each sensor mote or node features limited processing capabilities, but when coordinated with other nodes they have the ability to accurately monitor a given environment. Therefore, with a collection of sensor motes distributed over a region they form a wireless sensor network by interacting with one another to co-ordinate specific tasks.

Multiple wireless sensor motes have the ability to relay data from remote and inaccessible locations not requiring existing infrastructure such as wiring and mains power. This makes WSNs advantageous to traditional sensor networks by having the potential to be implemented in more environments more effectively.

Common WSN topologies, detailed in Figure 2.1, include star, mesh and cluster tree or hybrid networks. The star network have the advantage of simplicity. As the name suggests it is formed in a star configuration with outlying nodes communicating with a central node.
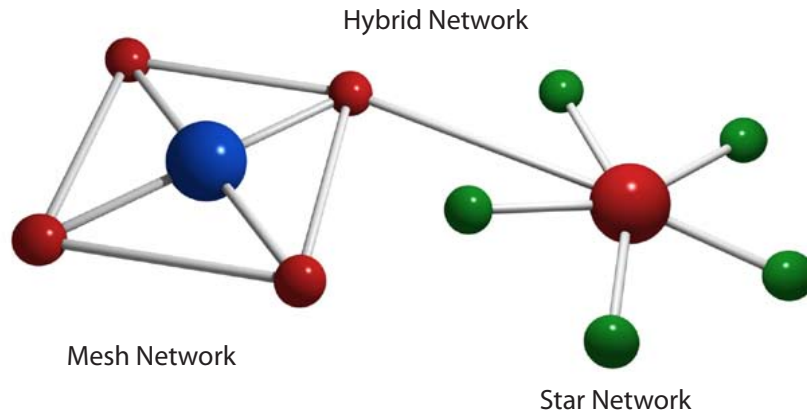
Figure 2.1: Wireless sensor network topologies

Mesh networks enable a higher degree of reliability. This topology consists of a variety of nodes able to communicate with neighbouring nodes within their transmission range. Information may be routed across the network using different nodes as relays. There is usually a choice of routes that can be used making the network more robust than a star network topology. Several network standards exist that define self-healing mesh networks which allow nodes to be added, removed, replaced or relocated without the need for traditional network administration. These network protocols are often based on the IEEE 802.15.4™ wireless personal area network (WPAN) standard that specifies compatible interconnection for data communication devices using low data rate, low power and low complexity, short-range radio frequency (RF) transmissions (IEEE Computer Society, 2007).

2.2   Applications for WSNs

WSNs were initially designed to cater for military applications but evolved into broader application fields such as industrial condition monitoring, agriculture and habitat monitoring (Chalard, Helal, Verbaere, Wellig & Zory, 2007). More recently, several technological advances allowed for promising alternative applications such as home automation, security, healthcare, industrial plant control and monitoring, to name a few. Figure 2.2 highlights common applications.

Due to modern day advances in pervasive sensors, the applications for WSNs are to some extent limitless. With microsensors being embedded into physical systems and structures, sensor networks have the potential to transform the way we traditionally monitor, understand and construct such systems.
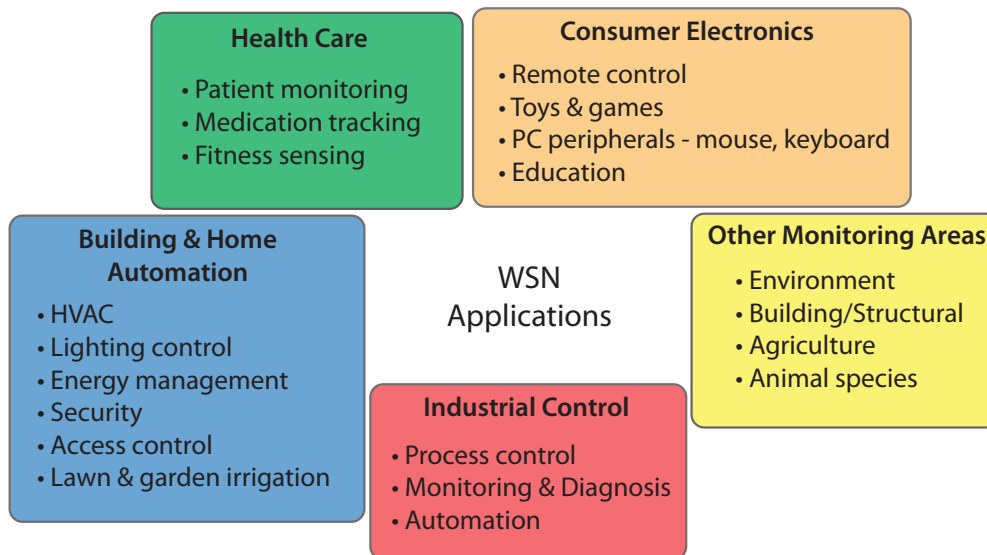
Figure 2.2: Wireless sensor network applications

2.3 The wireless sensor mote

It is essential for individual wireless sensor motes to operate on small amounts of energy and communicate through a wireless channel so as to not be constrained by traditional infrastructure requirements such as wires. Some form of local processing is also necessary to minimise transmission time. This is important since wireless communication is a major contributer to the overall energy consumption. Since these end devices are typically battery operated, they need to be ultra low-power. One such low-power technique that significantly reduces energy consumption is achieved by duty-cycling the on/off transmission time of the transceiver. WSMs would typically relay data out of harsh environmental conditions and therefore need robust communication techniques. This is crucial to overcome interference from noise and other wireless peripherals to guarantee high data integrity.

The last few years have seen the development of commercially available WSMs from companies such as Crossbow® Technology (2009), Arch Rock (2008) and Enocean® (2009).

Figure 2.3: TelosB wireless sensor mote platform from Sentilla™ (2009)

One such WSM platform is the TelosB sensor mote as shown in Figure 2.3. The TelosB is an open source WSM platform that is widely adopted by educational institutions for sensor network research. The TelosB sensor mote as a whole is characterised as the load for the proposed power management system. Performance capabilities as well as typical power consumption modes of the TelosB motes are highlighted in chapter 6 section 6.4.

2.4   Energy management

Sophisticated energy management techniques are essential in a WSN since the network is expected to operate for several years with the majority of motes functioning only off a primary battery. Due to this finite amount of available energy per mote it is crucial for energy optimisation not only on network level but especially on mote level. Network energy optimisation involves low-power energy efficient routing protocols that effectively manage energy consumption on a network level. Investigating these low-power network routing algorithms is beyond the scope of this research and further study only involved energy management on mote level. Energy awareness on mote level can be divided into four key categories:

Computing - The microcontroller unit (MCU) is responsible for controlling the various sensor inputs, processing and storing the data as well as communicating the data to other motes via a transceiver. The MCU is capable of functioning under different operating modes for power management purposes. This allows energy conservation between duty-cycles of measurements and transmissions.

Communication - The mote consists of a short range radio transceiver used to communicate to neighbouring motes. It can operate under modes such as transmit, receive, standby and sleep. The radio is by far the dominant energy consumer on the mote. A comparison done by Pottie & Kaiser (2000) in terms of energy cost of computation to communication reveals that 3000 instructions can be executed for the same energy cost as transmitting one bit over 100m. Power consumption can be significantly reduced by duty-cycling the on/off transmission time of the transceiver. Additionally, the gain or transmission strength of the radio can be adjusted and should be set to a minimum while still retaining the required transmission distance to the neighbouring mote. The radio should also be disabled whenever not needed.

Sensing - This includes onboard sensors such as temperature and light sensors to various external sensors. These sensors connect the mote to the world around it measuring, monitoring and controlling respective parameters. Energy consumption can be reduced by using low-power components. Disabling the sensors between measurements can contribute to preserving available energy.

Power supply management - Low-power voltage regulators and DC/DC converters are key building blocks in the implementation of power management techniques. This is especially

important to efficiently convert and store collected energy when utilising energy harvesting methods to power a sensor mote. By monitoring available energy the mote can adaptively schedule measuring and transmission duty-cycles to extend the operating life of the mote.

2.5   Limitations of battery operated motes

Battery technology has advanced in the last decade in several parameters such as performance, physical size, weight, recharge cycles and operating life. Despite these advances, portable and wireless electronics demands are seldom satisfied due to complex systems with increased processing capabilities. Even so, batteries continue to be the main source of power to portable electronics. This is largely due to advantages such as international standardisation, wide availability and relatively high energy density (Jansen, Fridstedt & Weernink, 2000).

Batteries have the disadvantage of being limited energy sources. Primary or non-rechargeable batteries often feature higher energy densities than secondary or rechargeable batteries but with the drawback of a single manufactured charge. Secondary batteries can however be recharged but are restricted to a number of recharge-cycles and would still need the energy from an external source to be recharged. Both primary and secondary batteries also have a limited operating life.

However, even with low-power components and energy aware protocols, energy consumed by the sensor mote can never be reduced to zero. Therefore, for a truly autonomous and maintenance-free WSM a "continuous" energy source would be needed. The closest this can be realised is to harvest available energy from the mote's surrounding environment.

The idea behind this is that the sensor mote would convert ambient energy in its environment into usable electricity to power itself. This technique has been named *energy harvesting* due to the way the mote is harvesting or scavenging unused available ambient energy. However, as mentioned by Roundy (2003), it is potentially difficult to develop a generic energy harvesting solution because each environment features different forms and amounts of ambient energy. Despite the challenges of effectively converting available ambient energy into usable electrical energy, energy harvesting is an appealing field of research. By introducing energy harvesting techniques for WSMs, sensor motes could become self-sustained with their operation limited not by their energy source but by the failure of their own hardware.

In order to understand energy harvesting for wireless sensor networks, the following chapter will highlight the fundamentals of energy, energy storage reservoirs and potential energy harvesting techniques feasible for transformer condition monitoring.

Chapter 3

Energy Harvesting for Wireless Sensor Networks

3.1   Fundamentals of energy and power

Energy, a fundamental concept in science and engineering and a common term referred to in everyday life, has it's origins from the Greek word *energeia* translated into *activity*, *working* or *capacity to do work*. Importantly, the term energy does not represent work but an association with work as indicated by Harper (2009).

The conservation of energy principle states; while the conversion of energy from one form to another exists, energy can never be created or destroyed. This early 19th century principle is however only true for the universe as an entirety (Jewett & Serway, 2008). Therefore, energy at a specific point may vary but the total energy remains constant over time for a closed system. Energy conservation can be stated as follows:

$$\sum_i U_i = K \tag{3.1}$$

where the summation over i refers to the total sum of any form of energy U in a system, and K is a constant to that system as stated by Flipsen (2005).

Energy is often denoted by the symbol E and measured in joule. The rate at which energy is transferred is given by equation (3.2).

$$P = \frac{dE}{dt} \tag{3.2}$$

The rate of energy transferred with reference to a time interval Δt is referred to the average power (P_{avg}) and defined by equation (3.3).

$$P_{avg} = \frac{E}{\Delta t} \tag{3.3}$$

The SI unit of power is joule per second (J/s), also called watt (W) named after James Watt (Jewett & Serway, 2008).

Energy is a scalar physical quantity that exists in a wide variety of forms such as thermal, light, chemical, kinetic, potential, nuclear, etc. One form of energy can be converted into another form of energy within certain limits. Figure 3.1 highlights most of the common known conversion techniques.
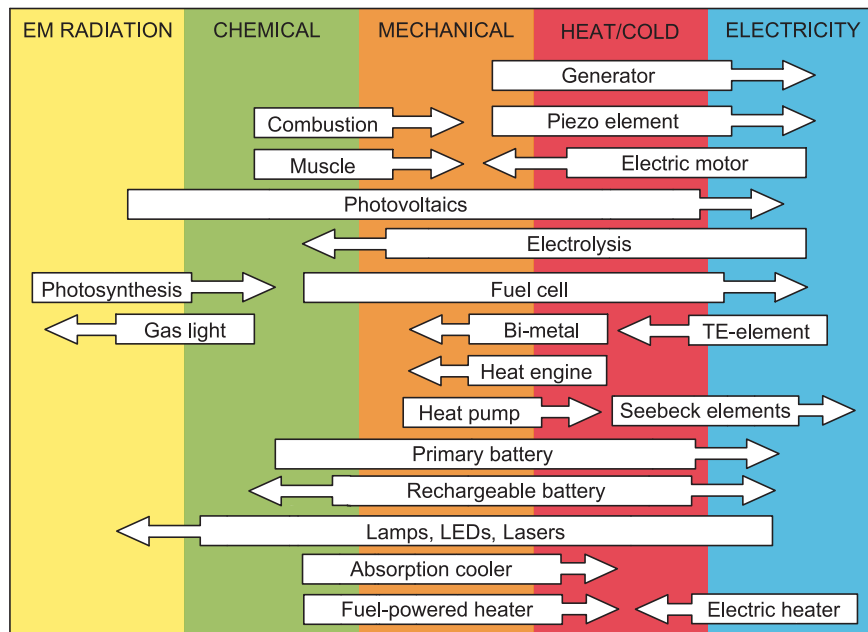
Figure 3.1: Energy conversion techniques redrawn from Flipsen (2005)

Familiar conversion examples are solar panels that implement photovoltaic technology to convert sunlight into useable electricity and electric motors converting electricity into mechanical rotation.

3.2   Energy reservoirs

An important parameter for all energy storage systems is the storage capacity. The storage capacity refers to the amount of energy stored that is needed for later use in a certain energy form (Jensen & Sørensen, 1984). Common energy storage devices are batteries, capacitors, supercapacitors and fuel cells. When energy capacities of different systems are compared the term *energy density* is used and defined as follows:

Energy density   -   The amount of energy the device can store per unit volume.

Since volume is a function of weight, energy density-per-weight is a term often associated with energy reservoirs. Storage devices can be characterised by a second parameter namely *power density*. The term *power density* is associated with the output energy transfer process and not the energy density of the storage device (Jensen & Sørensen, 1984).

Power density   -   The rate at which the device can deliver energy to the load per unit volume.

Batteries and fuel cells possess the capacity to store large amounts of energy but feature long charging and discharging times. Standard capacitors have the ability to deliver large amounts of power for brief periods of time but can only store small amounts of energy. Different sized batteries and capacitors provide various combinations of energy and power densities. Supercapacitors are a unique promising new technology that feature a combination of relatively high energy density with high power density. As seen in Figure 3.2, supercapacitors offer a middle ground with the positive characteristics of both batteries and standard capacitors.
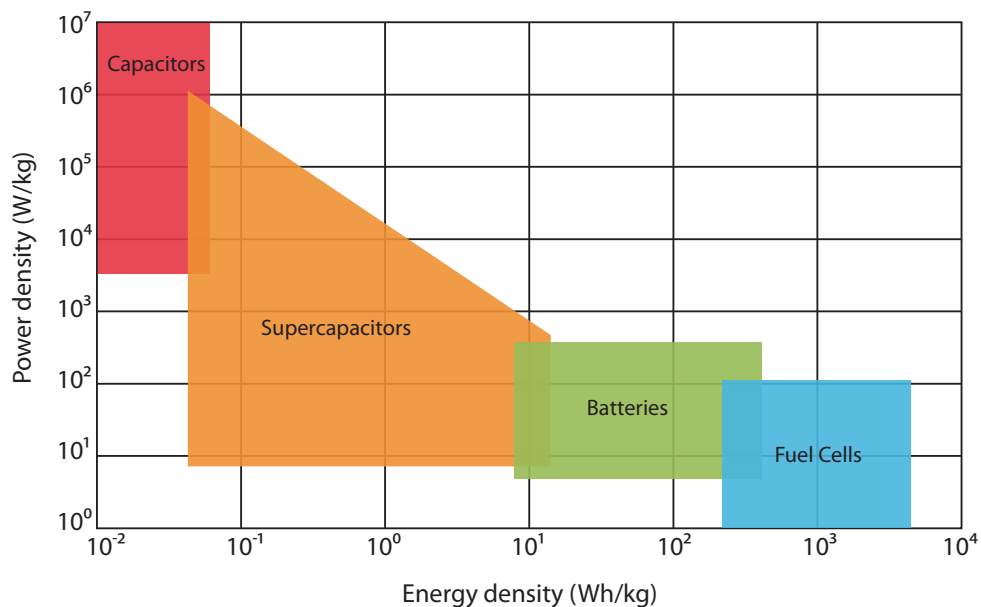
Figure 3.2: Power vs Energy for various energy reservoirs redrawn from Cap-XX (2008)

The amount of average power energy reservoirs such as batteries can deliver is a function of their operating life determined by the actual material, chemical reaction, operating temperature, recharge cycles and battery leakage. However, the power output of energy harvesting sources such as solar panels and piezoelectric generators is not a function of their operating life because their performance is not influenced by parameters such as recharge cycles and leakage (Roundy, 2003).

3.3 Batteries

A battery is a portable energy reservoir that converts chemical energy into electrical energy. The basic architecture of a battery consists of multiple voltaic cells stacked together with each cell having an anode and cathode with connecting electrolyte. Battery properties such as energy density, performance, size, weight and recharge cycles are directly related to the type of chemistry implemented. Batteries are generally classified into primary or non-rechargeable and secondary or rechargeable energy storage devices.

Primary batteries often feature higher energy densities for the same size secondary battery due to much higher impedance corresponding to longer energy storage. Primary batteries are however constrained to one discharge cycle from where they are either recycled or destroyed. Common chemistries for primary batteries are alkaline, carbon-zinc, lithium metal and silver oxide (Crompton, 2000).

However, due to the single discharge nature of primary batteries, energy harvested from the environment cannot be used to replenish the battery. Adding a primary battery to the energy harvesting management system will therefore not address the issue of limited energy on a sensor mote as described in the problem statement in section 1.2. A replenishable energy reservoir is needed for enhanced performance and prolonged system sustainability.

Current secondary or rechargeable batteries can be recharged between 500 and 1000 times depending on battery chemistry and usage. The type and duration of charging for secondary batteries are dependent on battery chemistry, condition of battery, depth of discharge (DoD) and temperature. Some higher energy density secondary batteries require complex charging techniques adding additional electronic circuitry to the system. Other limitations that could hinder long term deployment are operating life, limited recharge cycles and environmental conditions such as excessive low and high temperatures.

The following section will give a brief description of the most common types of secondary batteries highlighting advantages, limitations and typical applications of each chemistry.

3.3.1 Lead-Acid

Lead-acid batteries are the oldest type of rechargeable battery and feature poor energy-to-weight and energy-to-volume ratios. These batteries are nevertheless still widely adopted today due to their ability to deliver high surge currents, typically several ampères at times.

Several advances have been made in lead-acid batteries in the last few years to recover from depth of discharges down to around 50% of the battery's capacity. Therefore, an application requiring a battery capacity of 500Wh would need twice the capacity due to 50% DoD limitations. Lead-acid batteries also suffer from low energy efficiencies requiring an additional

40% of energy to fully charge the battery (Crompton, 2000).

The lead-acid battery is usually implemented in higher power applications such as automotive engine starting and back-up power for alarm systems. The relatively large physical size and weight compared to wireless sensor motes together with high self-discharge and low energy efficiency makes this chemistry not a common option as energy reservoirs in WSN applications.

3.3.2 Nickel-Cadmium (NiCd) and Nickel-Metal Hydride (NiMH)

Higher energy densities can be obtained from NiCd and NiMH batteries than lead-acid batteries. NiCd is an older technology and not as widely implemented as NiMH batteries. NiCd batteries operate well in extreme temperatures and achieve around 1000 charge-discharge cycles. However, they suffer from the memory effect. This effect in a battery is the tendency of the battery to adjust its electrical properties when subjected to a certain level of DoD for an extended period of time (Crompton, 2000). The memory effect is caused by regularly charging or topping up when the battery is not fully discharged resulting in a gradual loss in total energy capacity of the battery. NiCd batteries also have disposal concerns affecting the environment due to heavy metals in the manufacturing process.

NiMH batteries weigh less, do not suffer from the memory effect and last about 40% longer per charge compared to NiCd batteries. NiMH batteries are extensively used in portable consumer electronics such as wireless PC peripherals and toys available in common sizes such as AA and AAA. NiMH batteries can produce a near-constant output voltage for 90% of their energy capacity due to the low internal resistance. Another advantage is they do not require complex charging circuitry making NiMH batteries a feasible chemistry for low power energy harvesting applications.

3.3.3 Lithium-ion (Li-ion)

Lithium based batteries are currently amongst the most popular battery chemistries for portable consumer electronics ranging from cell phones and cameras to laptops. Li-ion batteries have no memory effect and feature superior energy density-to-weight ratios to NiMH batteries and also offering around double the energy per charge.

Li-ion batteries have a slow self-discharge rate with approximately 500 charge-discharge cycles depending on usage. Li-ion batteries have the advantage that they can be fashioned into various shapes and sizes to cater for specific applications by effectively filling available space in portable devices. Due to the high energy density growing interest are shown by automotive and aerospace industries to implement lithium based batteries (Thurston, 2003).

Li-ion batteries are however not very efficient at temperatures below 0°C and struggle to deliver high currents at low temperatures. Li-ion batteries are limited by their shelf life of typically 2 - 3 years. The shelf life of the battery is irrespective of the number of charge/discharge cycles and depends on time of aging since manufactured.

To avoid permanent damage, it is important not to exceed the maximum DoD of Li-ion batteries. Additional circuitry is often necessary to circumvent the battery from being discharged below a threshold.

3.3.4 Lithium-Polymer (Li-Po)

Li-Po technology progressed from Li-ion batteries with advantages of improved robustness to physical damage as well as reduced manufacturing costs. The same as with Li-ion batteries, Li-Po batteries can be manufactured into thin, flat and semi flexible shapes to be form fitted for individual applications. Another advantage of Li-Po batteries is they do not leak corrosive electrolytes.

Li-Po batteries can supply approximately 500 charge/discharge cycles depending on usage and prefer to be operated in a temperature range of 0 - 65°C. It is important that Li-Po batteries are closely monitored when being charged to ensure stability preventing excessive damage or explosion. Therefore, applications that feature Li-Po batteries are often higher power applications that require more complex circuitry. Lithium based batteries are still relatively expensive compared to chemistries such as NiMH.

3.4 Fuel Cells

Fuel cells feature a similar principle as batteries by converting chemical energy into electrical energy. Unlike batteries however, fuel cells have a separate fuel supply much like a fuel tank for an internal combustion engine in a motor vehicle. The external supply, typically consisting of hydrogen, is fed to the fuel cell from where the hydrogen is converted into water and electricity.

Fuel cells offer a wide range of power outputs from powering small portable electronics to megawatt stations for high power applications. Traditionally higher power fuel cells require various external components such as fuel pumps, re-circulators and cooling and control systems prohibiting power delivery in small portable devices. Fuel cells are often used in conjunction with rechargeable batteries or supercapacitors improving overall performance by providing a high energy high power solution (Flipsen, 2005).

Recent developments in fuel cell technologies have led to the small direct methanol fuel

cell (DMFC). The DMFC disposes of many of the external components in traditional fuel cells making portable power delivery a reality in small devices such as the PEMFC from Horizon fuel cells (Horizon Fuel Cell Technologies, 2007) shown in Figure 3.3.
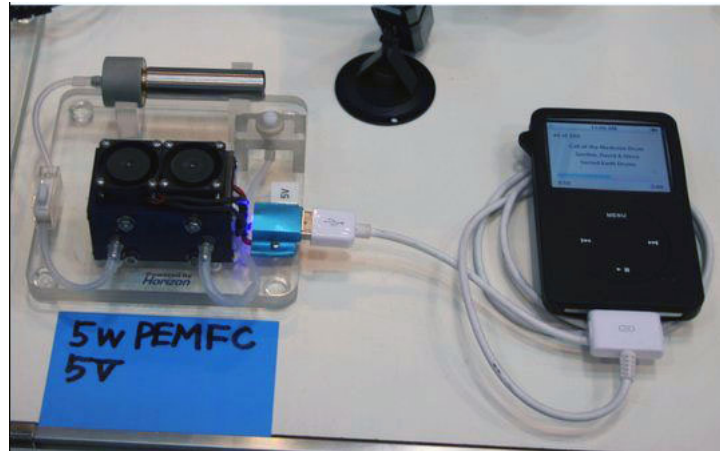
Figure 3.3: Horizon fuel cell powering an Apple® iPod® (Biggs, 2007)

Micro fuel cells seem to be a promising developing area for powering small portable devices in the future. Although fuel cells are limited to the energy in their fuel supply tank, it is possible to achieve longterm deployment when powering low-power devices such as WSMs. However, current fuel cells fall short of one of the objectives of this research; the design of a low cost power management system.

3.5 Capacitors

Capacitors consist of an insulating material; referred to as dielectric, layered between two conductive electrode sides. Energy is stored in an electric field by means of charge separation in the dielectric when a voltage potential difference is present across the electrodes. The amount of capacitance is a function of the surface area overlapping the two electrodes and type of dielectric medium. Capacitors are often configured in a layered arrangement with a small separation of opposing charges (Peebles & Giuma, 1991).

In terms of storing energy, electrolytic capacitors feature one of the largest capacitance per volume of any capacitor. They rely on a micrometer scale thick ionic conductive material deposited on one of its metal plates. Capacitors have high power density and can sustain high currents for very short periods. However, they have poor energy densities per volume compared to batteries and with energy density values of two orders of magnitude lower than supercapacitors (Jensen & Sørensen, 1984).

Even though the WSM requires small amounts of energy it is still large in comparison to the potential energy storage in normal capacitors.

3.6 Supercapacitors

Supercapacitors, often referred to as ultra capacitors or double layer capacitors (DLC), have similar characteristics to normal capacitors but offer significantly higher capacitance values per unit volume. Energy is stored the same way as in conventional capacitors by electrostatic charge separation unlike the electrochemical process in batteries (Flipsen, 2005). Figure 3.4 shows the physical size advantage of a 220mF supercapacitor compared to a 1mF conventional capacitor.
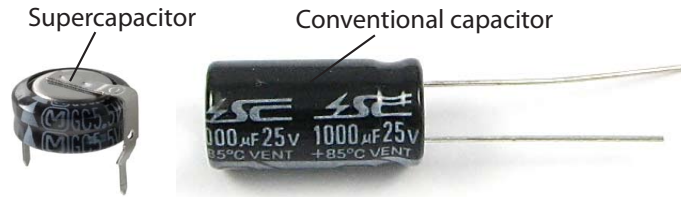
Figure 3.4: Physical size advantage of supercapacitors

The increased capacitance in supercapacitors is achieved by the high surface area with a molecule thin layer of electrolyte. There are three suitable types of electrode used for the manufacturing of supercapacitors namely: high surface area activated carbons, metal oxide and conducting polymers (Cap-XX, 2008). The most common supercapacitor technique uses the least expensive manufacturing process implementing high surface area activated carbons. The energy is stored in the double layer formed through the separation of charge at an electrified interface at a nanometer level unlike micrometer level for conventional capacitors.

Compared to batteries, supercapacitors can be used to deliver frequent pulses of energy without any detrimental effects or reduced operating life. Supercapacitors charge very quickly and safely where batteries are damaged by fast charging and certain chemistries require specific charging methods. Supercapacitors can be recharged hundreds of thousands of times without significant degradation in performance.

Supercapacitors have the life expectancy of standard capacitors if kept within their design limits with energy efficiency rarely falling below 90%. Although energy densities of supercapacitors are lower than batteries, the majority of the energy is available unlike batteries with DoD restrictions (Cap-XX, 2008).

3.6.1 Typical characteristics

The energy stored in supercapacitors can be calculated as for conventional capacitors. The stored energy is a function of the capacitance and voltage potential across the conductive plates. The energy stored in a supercapacitor can be calculated using equation (3.4) (Peebles & Giuma, 1991).

$$E = \frac{1}{2}CV^2 \tag{3.4}$$

where: E = energy available in supercapacitor (joule)

C = capacitance of the supercapacitor (farad)

V = steady-state potential across supercapacitor (volt)

The RC time constant is the time required to charge a capacitor to 63.2% or to discharge to 36.8% of the applied voltage across the capacitor. Figure 3.5 shows the charge and discharge curves of a capacitor RC circuit. RC is the term used for the time constant and refers to R (ohm) x C (farad) = τ (second).
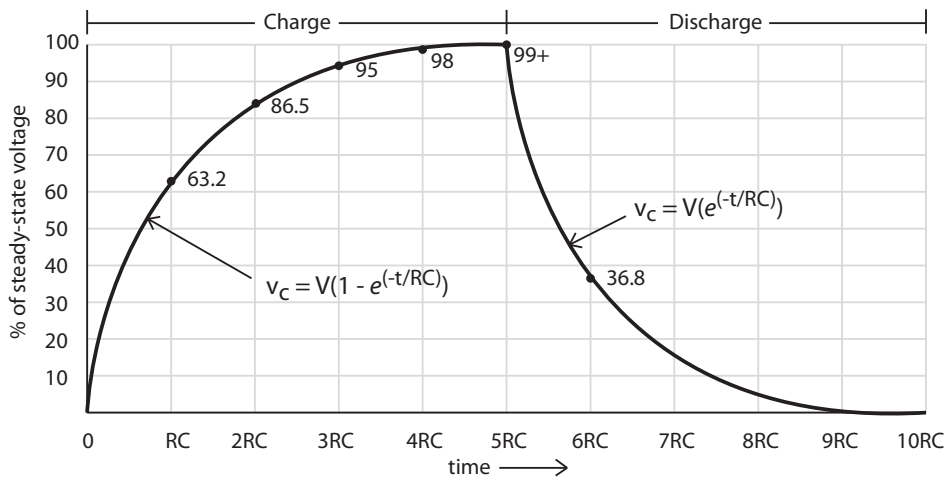
Figure 3.5: Capacitor RC time constant

The exponential equation for the voltage across the capacitor at any time t when charged is given by:

$$v_c = V(1 - e^{(-t/RC)}) \tag{3.5}$$

where v_c is the instantaneous voltage across the capacitor, V is the applied voltage and e is the base for the natural exponent with an approximate value of 2.7182818 (Fogiel, 2004).

Theoretically, the capacitor will never fully charge to the applied voltage, V. The capacitor will charge to 63.2% in the first RC time constant. During the second, third and fourth time constant, C will charge to 86.5%, 95% and 98% respectively of the applied voltage. When reaching the fifth RC time constant, v_c will be charged above 99% and is considered fully charged for all practical purposes. The potential across the capacitor is in steady-state after the fifth RC time constant if the applied voltage is still present.

19

When the applied voltage is removed, the capacitor will discharge according to the equation given by:

$$v_c = V(e^{(-t/RC)}) \qquad (3.6)$$

where V refers to the steady-state starting voltage across the capacitor. The capacitor will discharge to 36.8% in the first RC time constant and is considered fully discharged after five time constants (Fogiel, 2004).

Capacitors and supercapacitors alike behave entirely differently from rechargeable batteries when charged and discharged. Unlike the potential across the plates, a cell voltage of a battery is chemically defined. The voltage is for the most part constant during charge and discharge cycles. The voltage across a capacitor increases and decreases linearly with respect to the charge across the plates (Flipsen, 2005). Figure 3.6 shows the different charge and discharge characteristics for a capacitor and a rechargeable battery.
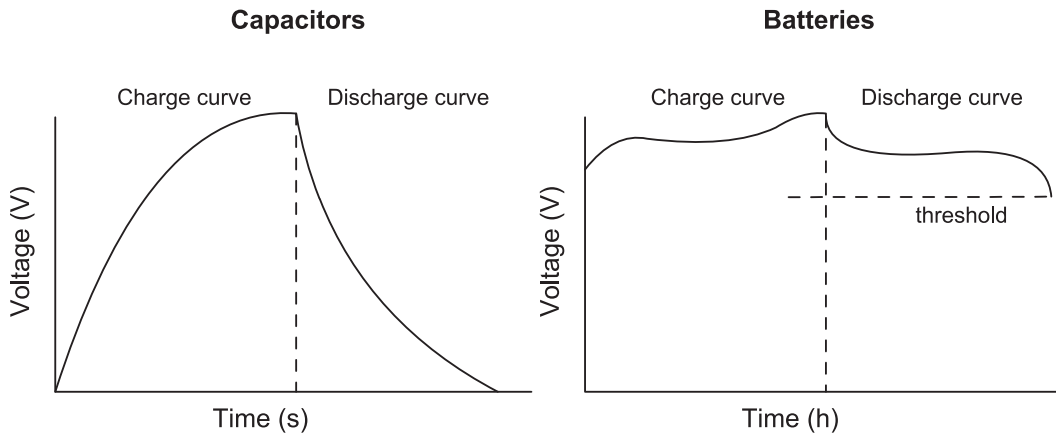
Figure 3.6: Charge and discharge characteristics redrawn from Flipsen (2005)

Cooper Electronic Technologies (2005) stated that high pulse power applications and short-term hold-up power applications benefit significantly from supercapacitors. Pulse power applications are defined by brief bursts of high current demands such as the transmission period of a wireless sensor mote. Hold-up applications are characterised by the requirement to deliver continual load power for a defined period of time.

Each of these applications emphasises different performance parameters of the device. Wireless sensor motes can be characterised as both a pulse power and hold-up power application. They would typically be in a low power sleep mode and wake-up at regular intervals therefore being a pulse power application. Secondly, with sustainability in the network as a requirement the wireless mote also qualifies as a hold-up power application. High pulse power applications benefit primarily from the low equivalent series resistance (ESR) of the storage medium, while hold-up power applications benefit from the supercapacitor's large capacitance value.

3.6.2 Hold-up power

In order to incorporate the correct sized supercapacitor for a specific application, an approximate calculation is given by Cooper Electronic Technologies (2005). The energy required during hold-up (E_{HOLD}) and the energy decrease (E_{DEC}) in the supercapacitor are evaluated in terms of working voltage (V_{WV}) and minimum operating voltage (V_{MIN}).

Energy needed during hold-up period:

$$E_{HOLD} = \frac{1}{2}I_{LOAD}(V_{WV} + V_{MIN})t \tag{3.7}$$

Energy decrease in supercapacitor:

$$E_{DEC} = \frac{1}{2}C(V_{WV}^2 - V_{MIN}^2) \tag{3.8}$$

Therefore, if E_{HOLD} equals E_{DEC}, equation (3.7) and (3.8) can be reworked to get the minimum capacitance that guarantees hold-up to V_{MIN} (neglecting voltage drop due to internal resistance):

$$C = \frac{I_{LOAD}(V_{WV} + V_{MIN})t}{(V_{WV}^2 - V_{MIN}^2)} \tag{3.9}$$

3.6.3 Pulse power

Pulse power can be defined by an application having a relatively low continuous current with respect to short bursts of higher currents, typically several orders of magnitude larger. The duration of these pulse power currents can range from milliseconds to a couple of seconds with a low duty-cycle of the pulses often less than 10%, depending on the application demand.

If we assume the supercapacitor is the sole supplier of energy during the pulse, the drop in working voltage (V_{DROP}) is dependent on two parameters: the instantaneous voltage drop due to the load current supplied through the internal resistance (R) of the supercapacitor and secondly the drop in capacitor voltage at the end of the pulse period. This relationship is shown in equation (3.10) (Cooper Electronic Technologies, 2005).

$$V_{DROP} = I_{LOAD}(R + \frac{t}{C}) \tag{3.10}$$

where t is the required hold-up time or pulse duration in seconds.

Upon inspection of equation (3.10), it reveals that in order to minimise the voltage drop of the supercapacitor, the internal resistance (R) must be low and the capacitance (C) high.

3.7 Significance of energy harvesting for WSNs

Currently the majority of WSMs are primarily powered by limited energy reservoirs such as batteries. This poses a serious problem when operating for extended periods such as several years. Lots of research has gone into power-down modes and energy efficient routing protocols to minimise energy consumption. However, as highlighted by Kansal, Hsu, Zahedi & Srivastava (2007), the energy consumption of the WSM can never be reduced to zero. This has led to a new field of interest namely: energy harvesting or energy scavenging. A key advantage of harvested energy to stored energy is that it is potentially inexhaustible. Although harvested energy is potentially free in most cases, a limit often exists on the rate the energy can be extracted and converted into usable electrical energy.

In an effort to realise self-sustained wireless condition monitoring sensor motes, techniques for harvesting available energy were explored. Various feasible energy harvesting methods for sensor motes already exist as reported in (Roundy, Otis, Chee, Rabaey & Wright, 2003; Shenck & Paradiso, 2001; Raghunathan, Kansal, Hsu, Friedman & Srivastava, 2005; Morias, Fernandes, Matos, Serodio, Ferreira & Reis, 2008; Ottman, Bhatt & Lesieutre, 2002; Buric, Kusic, Clark & Johnson, 2006; Alippi & Galperti, 2008; Cuadras, Gasulla, Ghisla & Ferrari, 2006; Chao, Tsui & Ki, 2007; Guilar, Chen, Kleeburg & Amirtharajah, 2006; Vijayaraghavan & Rajamani, 2007; Ang, Tan & Panda, 2007; Mehraeen, Jagannathan & Corzine, 2008; Wu, Chen, Chen, Wang & Chen, 2006). The proposed research investigated relevant harvesting methods optimised to cater for remote high voltage transformer condition monitoring.

In a WSM powered solely with a primary battery, the main power management goal is to minimise energy consumed by meeting minimum required performance demands (Kansal *et al.*, 2007). By introducing energy harvesting on the device the operating life can be extended by reducing the energy demand from the battery. A possibility for truly autonomous operation can be to eradicate the battery altogether. The device will harvest all necessary energy from the environment and not be constrained to battery life.

With the battery eliminated, perpetual operation is possible if the energy is harvested at the same rate that the device consumes it. This mode of operation is referred to by Kansal *et al.* (2007) as energy neutrality.

Power management design considerations for energy neutrality differ from maximising operating life in two ways:

1. Energy Neutral Operation: Operate mote in such a way that consumed energy is always less than harvested energy.

2. Maximum Performance: What is the maximum maintainable performance in a particular environment, while guaranteeing energy neutrality?

An ineffective approach might be to select an energy harvester capable of delivering sufficient energy to the load under maximum energy demand. This approach may not be a feasible option in many situations due to size and cost constraints. Furthermore, in some cases such as solar energy harvesting, the energy output is zero at night.

Kansal *et al.* (2007) suggested a more reasonable approach by adding a power management system featuring an energy reservoir for storage between the harvesting source and load. This way the system was buffered by matching the energy harvesting source and load more effectively.

Energy Harvesting Source - This refers to any transducer capable of converting various forms of available energy into usable electrical energy. Typical energy harvesting technologies include solar cells, piezoelectric and thermo-electric generators, wind turbines and other transducers extracting available energy from the environment. In the majority of cases, the output of the harvested energy is irregular and beyond the control of the designer as shown in Figure 3.7. More than one harvesting source may well be present at any particular mote allowing for a hybrid energy harvesting system.
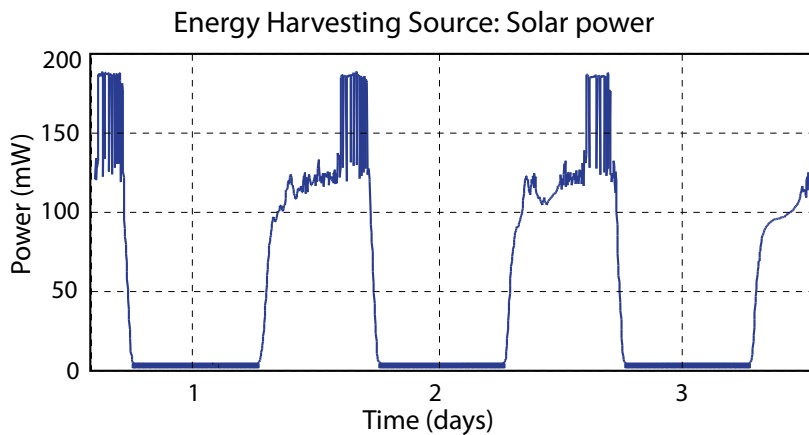
Figure 3.7: Power output of energy harvesting source

Load - This refers to the device consuming the harvested energy, in this case the WSM. Sensor motes are capable of operating in different modes such as sampling sensor values, transmitting and receiving data and relaying data from adjacent motes, all consuming energy at different rates. Figure 3.8 shows different power levels of a TelosB WSM such as sleep state, processor enabled and the radio transmitting and receiving. Another share of energy consumption often neglected is the energy consumed by the harvesting system itself. In some cases this can have a significant effect on the overall energy consumption. For example, a harvesting system incorporating digital maximum power point tracking relies on a microcontroller to operate. This influences shutdown modes of the load which consequently affects the overall energy consumption.
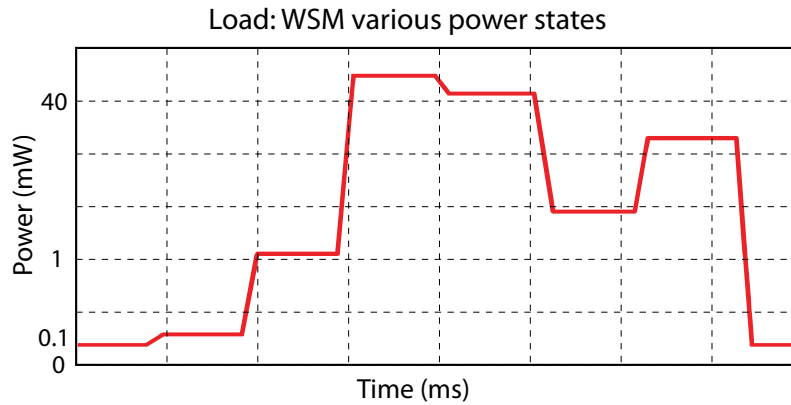
Figure 3.8: Power requirement of load

Energy Harvesting System - This refers to the system designed to match the variable power output of the energy harvesting source to the inconsistent power demand from the load by collecting, converting and storing energy. The energy harvesting system typically features an energy storage reservoir such as a rechargeable battery or supercapacitor to collect the harvested energy. This is necessary to buffer the often higher instantaneous power demand from the load from the energy output of the harvesting source. The importance of an energy buffer is evident by comparing Figure 3.7 and 3.8. The power magnitudes and the time frame over which the power is harvested from the energy harvesting source differs considerably to the power required by the load.

Possible methods of providing power for WSMs can be classified into three groups (Roundy, Otis, Chee & Rabaey, 2004) namely: mote based energy storage, off-mote energy storage and ambient energy harvesting

1. *Mote based energy storage:* (e.g. battery, micro fuel cell) Currently the most widely adopted method of supplying power to the mote would be through batteries. This group also covers more exotic onboard power sources such as micro-fuel cells (Matsuo, Matsuo, Tuji, Kobayashi & Sekine, 2006) and radioisotopes (Lal, Duggirala & Li, 2005). Many of these solutions however either involves limited chemical energy that requires refueling or their radioactive nature poses additional user concerns that prevent wider implementation.

2. *Off-mote energy storage:* (e.g. via electromagnetic power or physical wire) This group classifies methods of distributing energy to the mote by an external power source. Electromagnetic power emission is extensively used in Radio Frequency Identification (RFID) tags, powered by a nearby source that transmits RF energy (Sample, Yeager, Smith, Powledge & Mamishev, 2006). WSMs feature much more complex processing and networking algorithms, consequently consuming considerably more power. The amount of RF radiation needed to flood an entire network of sensor motes would not be a feasible option as the radiation would exceed safety regulations. Distribution of power via wire only applies to exceptional cases and in the majority of applications

somewhat defeats the purpose of wireless sensor networks.

3. *Ambient energy harvesting:* (e.g. solar, vibration, wind) An abundance of freely and to some extent limitless available energy often exists in the environment surrounding the sensor mote. Common ambient conversion technologies are available such as solar and wind. In addition to environmental energy harvesting, the source of energy can also be from the monitoring subject itself such as vibrations experienced on the transformer's outer tank and inductive or capacitive coupling to high voltage transmission lines.

3.8   Importance of energy storage

For a truly self-sustained WSM a replenishable energy source is essential to power the mote. Limited energy reservoirs such as primary batteries fall short of this requirement. Rechargeable batteries are also inadequate due to their restricted operating life and charge-cycles, typically between 500 and 1000.

Power sources such as solar, wind and vibration energy harvesting are needed to execute these requirements to enable several years of operational life. However, the energy output of these power sources varies with time and depends on environmental conditions typically outside the control of the designer. A form of energy storage must therefore be present to buffer the varying harvested energy while delivering higher instantaneous power to the load.

The operating life of the WSM can be extended by implementing supercapacitors as energy reservoirs for harvested energy. Supercapacitors represent a compromise between rechargeable batteries and standard capacitors. Although higher energy densities can be achieved by rechargeable batteries, supercapacitors retain many of the favorable characteristics of standard capacitors such as increased operating life and straightforward charging (Roundy *et al.*, 2004). Most supercapacitors offer more than half a million charge-cycles and beyond 10 year operating life after which 80% of the useful energy is still available due to the very low ESR. The significantly higher ESR in a battery at this point lowers the amount of useful energy to 50% causing premature end of life. By designing the mote to operate on 50% energy capacity and utilising supercapacitors as the sole energy storage medium, the operational life time can be extended to 20 years (Simjee & Chou, 2006).

3.9   Summary of potential power sources and energy harvesting technologies

Comparing various types of power sources to one another is a difficult task, such as evaluating the efficiency of a piezoelectric generator against the efficiency of a rechargeable battery. Roundy *et al.* (2004) made an effort to provide a general understanding of the wide variety of

potential power sources for WSMs by introducing comparison metrics such as power density, energy density, power density per year of operation, complexity of required power electronics, need for secondary storage and common availability of the power source.

Potential energy harvesting technologies and common energy storage methods are shown in Table 3.1 . The values in the table are derived from a combination of published studies (Roundy, 2003; Roundy *et al.*, 2004) and information commonly available in textbooks and datasheets.

Table 3.1: Summary of power sources and energy storage reservoirs for WSMs

Power Sources	W/cm^3	J/cm^3	Secondary Storage	Voltage Regulation	Commonly Available
Primary Battery	-	2880	No	No	Yes
Secondary Battery	-	1080	-	No	Yes
Micro-Fuel Cell	-	3500	Maybe	Maybe	No
Supercapacitor	-	50-100	No	Yes	Yes
Solar (outside)	15000*	-	Usually	Maybe	Yes
Solar (inside)	10*	-	Usually	Maybe	Yes
Air flow	380	-	Yes	Yes	No
Vibrations	200	-	Yes	Yes	No

*   Denotes sources whose fundamental metric is power per square centimeter rather than power per cubic centimeter.

Table 3.1 contains energy harvesting power sources and therefore the amount of power available is not a function of the life-time over which the device operates. However, it should be noted that the energy storage technologies displayed in the table contained a fixed amount of energy and the available power decreases over operating life. Table 3.1 is by no means comprehensive. It does however provide a broad overview of potential methods to harvest and store available energy for the present application. Other potential power sources were also considered but were believed to be outside the scope of the present project for reasons explained in section 3.10.

From the investigation on potential power sources and energy harvesting technologies, two questions arise:

- In the event of choosing an energy harvesting technology, what type of energy reservoir would be feasible for an extended operating life?

- Which would be preferable to use; a rechargeable battery or a energy storage medium such as a supercapacitor?

A battery powered WSM is often more feasible for operating durations typically in the range of 2 years or less (Simjee & Chou, 2006). However, often much longer operating life-times are demanded from these devices. For the present application condition monitoring is expected beyond 10 years. A battery as power source is limited to ageing and the number of

recharge cycles requiring replacement after one to two years (Simjee & Chou, 2006). With such recurring maintenance batteries can become a costly option for larger WSNs. Moreover, access to deployed motes are often difficult, limited or even hazardous further prohibiting maintenance. Therefore, incorporating battery technology into the design criteria will not enhance the longevity of these wireless condition monitoring applications.

Since these harvesting technologies collect rather small amounts of energy at any given time, it is necessary to store the harvested energy. This is especially true in the case of vibration based harvesting since the sensor mote is not capable of operating straight from the piezoelectric generator as detailed in section 6.5. Furthermore, in the case of solar energy harvesting it is necessary to store available energy gathered in the day to sustain the sensor mote by night. Energy reservoirs described in section 3.2 are therefore a critical part of any energy harvesting system to enable effective operation over extended periods of time. With the many advantages of supercapacitors, it promises to be a viable option as energy reservoir.

3.10 Feasible energy harvesting techniques

The feasibility of energy harvesting techniques is very application specific. Solar radiation energy harvesting might be a viable option for sensor nodes deployed outside but not for condition monitoring of machinery below deck in a ship. In many cases, where solar energy harvesting is present, vibration energy harvesting is not. For instance, vibration energy harvesting often occurs on machinery inside buildings, a place where solar energy harvesting is minimal.

An application that would largely benefit from both solar and vibration energy harvesting would be machinery situated outside. Since the proposed research project is based around condition monitoring for high voltage power transformers situated outside, it fits ideally into both energy harvesting categories. A decision was made to pursue both solar and vibration based solutions for the development of a hybrid energy harvesting power management system. By introducing a hybrid energy harvesting system this allowed for a more flexible design catering for a wider application spectrum and not necessarily limited to transformer condition monitoring.

In the event of harvesting available energy surrounding a high voltage power transformer a few factors need to be looked at.

Will this specific energy harvesting technique be feasible in terms of:

- physical size?
- location of transformer?
- cost of development?

- commercial availability of components?

The power transformer is situated outdoors, making solar an obvious choice of power to supply the WSM. Solar energy harvesting is already a mature technology and has a relatively high power density compared to other energy harvesting methods such as vibration and inductive coupling. Solar energy harvesting can however only supply power during the day and is not particularly effective in extended low light intensity conditions.

An additional energy harvesting method that can be implemented is vibration energy harvesting. In the last few years there has been extensive research done into vibration energy harvesting (Priya, 2007; James, Tudor, Beeby, Harris, Glynne-Jones, Ross & White, 2004; Roundy *et al.*, 2003; Shu & Lien, 2006). This is largely due to the decrease in power requirements from wireless sensors making vibration energy harvesting a feasible option as power source. Vibration energy harvesting is an attractive option due to the common occurrence of vibrations on the outside tank of high voltage power transformers. The vibration is often associated with the "hum" generated by machinery operating on AC voltage. As shown in Table 3.1, the potential output power from vibration energy harvesting is much smaller in comparison to solar energy harvesting. Nonetheless, vibration energy harvesting allows for continual energy generation given the transformer is operational.

3.11   Summary

With these considerations in mind, it was concluded that solar and vibration based energy harvesting appeared to be the most promising methods of power sources to the WSM. These two harvesting technologies were selected as viable techniques to enable a hybrid energy harvesting solution for the prototype design. As set out in the delineation of the research detailed in section 1.5, the project was limited to and only investigated solar and vibration energy harvesting further as possible solutions. Chapters 4 and 5 will highlight these two possible energy harvesting methods respectively by harvesting energy through the mechanical vibrations from the power transformer and solar radiation from the environment.

Chapter 4

Vibration energy harvesting

4.1 Energy harvesting from the power transformer

Vibration-to-electricity conversion offers the potential for WSMs to operate autonomously in many vibration rich environments. Low level vibrations are a common occurrence on industrial machinery, large commercial buildings and various transportation methods such as automobiles, aircraft, trains and ships. Therefore, given the many applications for vibration based power generation, the industry can significantly benefit from the development of such a system.

The feasibility of vibration-to-electricity conversion has recently become more evident with examples of real world applications implementing vibration as a power source. Leland, Lai & Wright (2004) designed a self-powered wireless temperature sensor node. The sensor node was mounted on a wooden staircase and used a piezoelectric cantilever to generate electricity from vibration in the staircase. Continuous human traffic for 50 minutes on the staircase produced an output of 30μW from the piezoelectric generator and was sufficient to transmit two temperature measurements.

Another application highlighting the feasibility of vibration energy harvesting is shown by Discenzo & Chung (2006). The objective of the project was to establish the viability of a vibration energy harvesting system for condition monitoring of machinery below deck in a ship. The self-powered wireless motes were designed to continuously harvest energy from a vibrating machine using a piezoelectric cantilever beam. The harvested energy was stored in a capacitor bank and used to power the external accelerometer and a commonly available WSM. The sensors were left unattended for four months to gather vibration data from the machines. Subsequent to the sea trial all the sensors were removed from the ship with more than 8000 data files captured to examine the vibrations on the machines.

The author is aware that other potential energy harvesting methods exist such as through

inductive coupling, capacitive coupling and thermocoupling. However, to keep the design as generic as possible for implementation in other applications, vibration energy harvesting was found to be a promising conversion method. Due to the expandability of the proposed design, covered in chapter 6, a future addition to the present research could investigate adding energy harvesting techniques that will contribute to the overall collected energy harvested.

4.2 Piezoelectric theory

Piezoelectricity, meaning *pressure* -electricity in Greek, was discovered by the Curie brothers more than 100 years ago. They found that the physical dimensions of quartz changed when subjected to an electrical field and conversely generated electrical charge when mechanically deformed. One of the first applications of the piezoelectric effect was made in the 1920's by Langevin, who developed the first sonar by implementing an underwater quartz transmitter and receiver system (Taylor, 1985).

Piezoelectric materials have been used extensively in passive transducers such as microphones, hydrophones, strain gauges and resonators. However, due to the advances in low power electronics, another feature of piezoelectric materials became popular, that being the ability to harvest electrical energy from vibrations to power electronics.

The piezoelectric effect is the respective material's capacity to convert mechanical energy into electrical energy and vice versa. When an external force mechanically strains the piezoelectric element, the ions in these unit cells are aligned in a regular pattern. The discrete dipole effect accumulates, resulting in an electrostatic potential developing across the piezoelectric element (Taylor, 1985). Piezoelectric material is generally operated in two different modes, 31 and 33, shown in Figure 4.1.
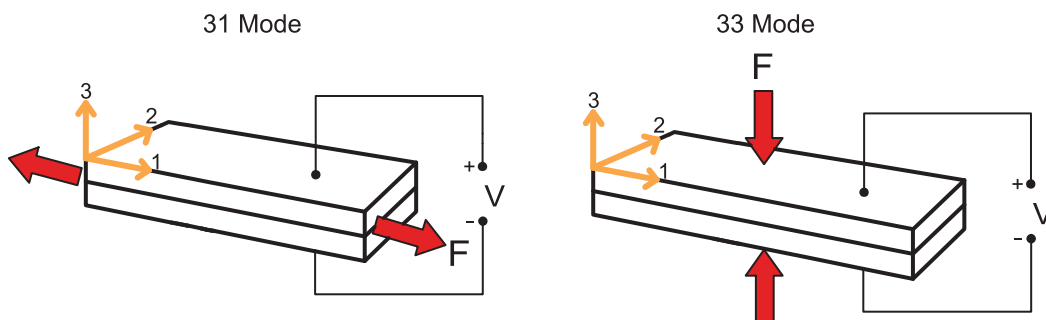
Figure 4.1: Piezoelectric operation modes redrawn from Roundy (2003)

The conventional axes x, y and z are labeled 1, 2 and 3 respectively. Therefore, 33 mode means both the voltage and force act in direction 3. The material can also be operated in 31 mode, meaning the voltage is poled in direction 3 and the mechanical force in direction 1. Piezoelectric material operating in 31 mode is often called cantilevers and features two thin bending elements with a centre metal shim to add flexibility to the brittle nature of

the piezoelectric material. As the cantilever bends, the top layer of the element is in tension while the bottom element is in compression or vice versa. Therefore, if the layers are poled in the same direction and electrodes connected properly, the current produced by each layer will add. This configuration is called parallel poling. Also, if the layers are poled in opposite directions, the voltage will add creating series poling. In theory, the poling and number of layers only affect the current to voltage ratio and the potential for power conversion therefore stays the same (Roundy, 2003).

The coupling in 31 mode is lower than 33 mode, but there is a key advantage operating in 31 mode. Firstly, larger strains can be produced using smaller input forces. Secondly, a much lower resonance frequency can be achieved in 31 mode compared to the same size device operating in 33 mode. A fairly large and impractical proof mass or end weight would be needed for the 33 mode to reach the same low resonance frequency (Taylor, 1985). As it turns out coupling in 31 mode was essential in our case as the frequency of interest was 100Hz.

4.3   Characteristics of vibration source

A generic vibration-to-electricity model detailed in section 4.5 can roughly estimate the power output given by the magnitude and frequency of the input vibration together with the size and mass of the mechanical-to-electrical converter. In order to predict an expected power output from the vibration, information about the vibration source needs to be obtained.

4.4   Measured transformer vibration

The material of transformer cores exhibits magnetostrictive properties that cause the core to strain or shrink on both the positive and negative cycle of the supply frequency. The straining produces a relatively large vibration component at double the supply frequency (Masti, Desmet & Heylen, 2004). This vibration component double the supply frequency is a common vibration occurrence in machines and is referred to as the fundamental vibration frequency (Shengchang, Yongfen & Yanming, 2006). In the present case the fundamental vibration frequency of the power transformer is 100Hz. With ageing of the transformer more harmonics or multiples of the fundamental frequency become evident (Bartoletti *et al.*, 2004). Some of the measurements also revealed a rather large vibration magnitude at 300Hz, as shown in Figure 4.7.

The transformer under test was a 30 year old 500MVA power transformer shown in Figure 4.2. The vibrations were measured on different parts on the outside tank of the transformer. All the measurements were taken either by the ADXL330 accelerometer or the piezoelectric cantilever. While the accelerometer gave an accurate value of acceleration at various vibra-

tion frequencies, the piezoelectric transducer allowed for a more practical approach in terms of the expected amount of energy to be harvested. The data was acquired with a Tektronix® TPS2014 battery operated oscilloscope and the respective frequency components were obtained by applying the built-in FFT[1] function to the time domain waveforms.

Figure 4.2: 500MVA power transformer

A vibration frequency spectrum of the transformer is shown in Figure 4.3. The spectrum shows frequency components up to 1500Hz. All phenomena of interest occur inside this band of frequencies. It is evident that above 1kHz the vibration magnitudes[2] start dropping off in the order of tens of dBs. The vibration signals above 1kHz therefore become negligible and do not contribute to any useful mechanical-to-electrical conversion. Moreover, lower frequency peaks have the largest potential for power generation as explained in section 4.5.

Bartoletti *et al.* (2004) stated that old transformers showed an increase in the harmonics with frequency multiples of the fundamental. The device under test (DUT) was a 30 year old transformer with evidence of increased magnitudes of harmonics clearly visible between 200Hz and 500Hz in Figure 4.3. The dotted graph at the bottom of Figure 4.3 shows a measurement taken next to the transformer. From this it could be clearly seen that there were no significant peaks especially at the critical frequency of 100Hz and multiples of 100Hz. This verified the source of the vibration measured being on the transformer tank and was therefore no external source of interference or noise.

It is important to measure the vibration strength for further theoretical verification as well as to accurately replicate the vibrations of the power transformer in a laboratory setup.

---

[1]A frequency span of 2.5kHz and Hanning window for best frequency resolution were selected for all FFT measurements.

[2]0 dB is referenced to $1V_{rms}$ for all frequency magnitudes.
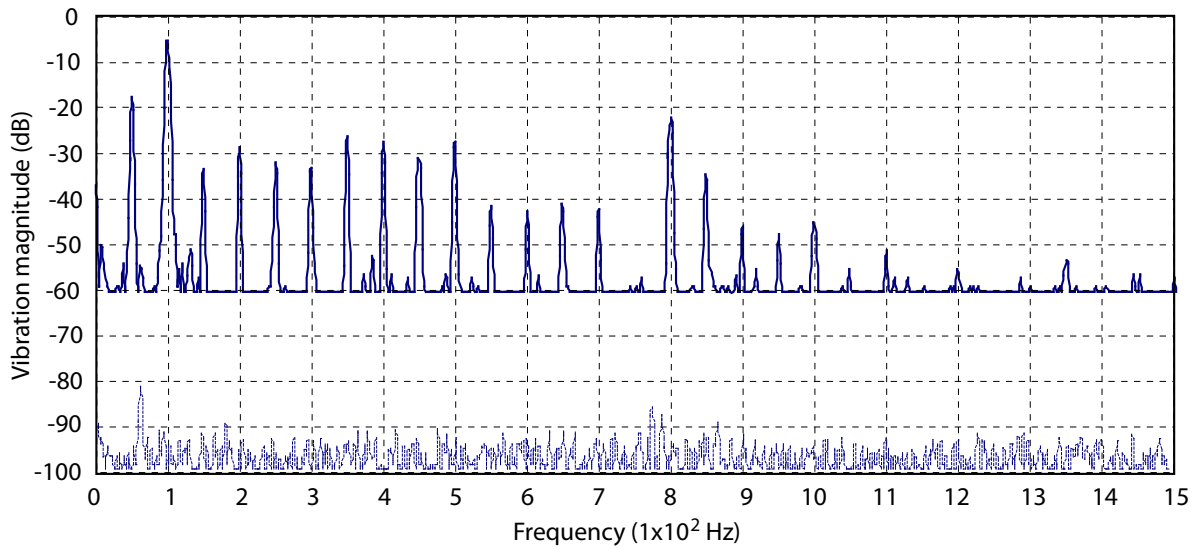
Figure 4.3: Frequency spectrum of measured transformer tank vibration

Figure 4.4 displays the output signal of the accelerometer attached to the tank of the transformer. Magnitudes of $600mV_{P-P}$ were measured with values peaking at $900mV_{P-P}$ at particular positions on the power transformer. The ADXL330 accelerometer has a sensitivity of 300mV/g, thereby corresponding to a powerful acceleration of 2 - 3g or roughly 20 - $30m/s^2$.
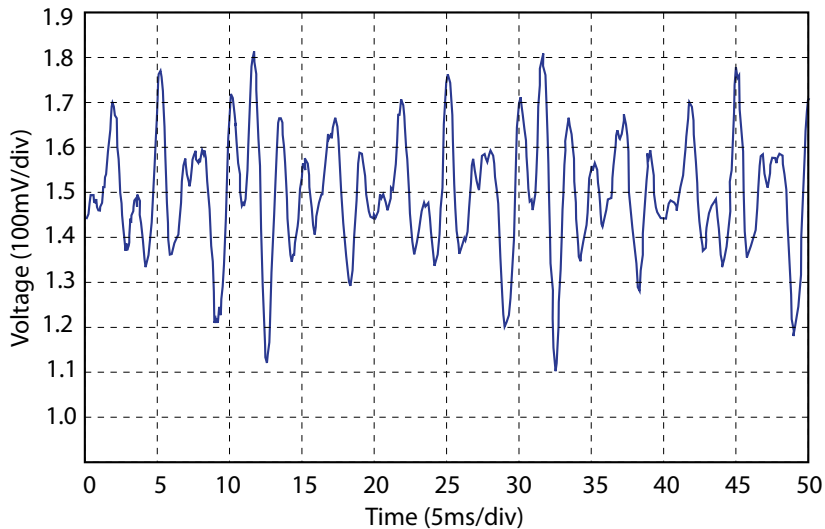
Figure 4.4: Vibration magnitudes measured by the ADXL330

With piezoelectric energy harvesting we are especially interested in the fundamental frequency since the output power of the piezoelectric cantilever is inversely proportional to the frequency, as will be explained with the generic conversion model in section 4.5.

The measured output voltage from the piezoelectric generator is shown in Figure 4.5. The piezoelectric generator is inherently a mechanical low pass resonance structure. This explained the near sinusoid in the time domain with some deformation evident due to intro-

duced harmonics.
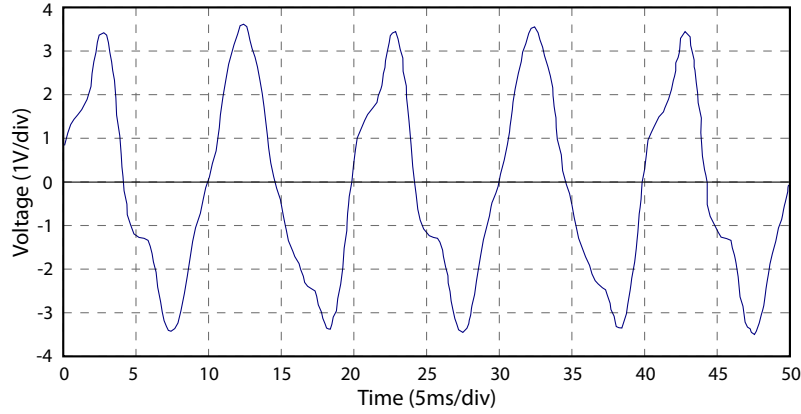
Figure 4.5: Measured piezoelectric cantilever voltage subjected to transformer vibration

It should be noted however that the way the piezoelectric generator was coupled to the transformer tank dramatically influenced the amount of acceleration and resultant output power. Experiments were done by attaching the piezoelectric cantilever and accelerometer enclosures with thin double-sided tape. The output voltage of the piezoelectric generator was considerably less than the laboratory experiments subjected to the same amount of acceleration. This could be largely construed to the damping effect of the double-sided tape, inertia of the piezoelectric cantilever and possible discrepancies between the tuned resonance frequency of the piezoelectric generator and the actual fundamental frequency of the power transformer at that position.

Vibration measurements on the power transformer were taken primarily at three positions as shown in Figure 4.6. Peak vibration frequencies proved sensitive in positioning of the accelerometer on different parts of the power transformer as detailed by Figures 4.8 and 4.7. Although powerful vibrations were present in abundance, the peak frequency values varied considerably in magnitude at the different positions. According to Mechefske (1995), vibration measurements may prove complicated due to the complex interaction of the vibrations on the mechanical structure of the transformer.
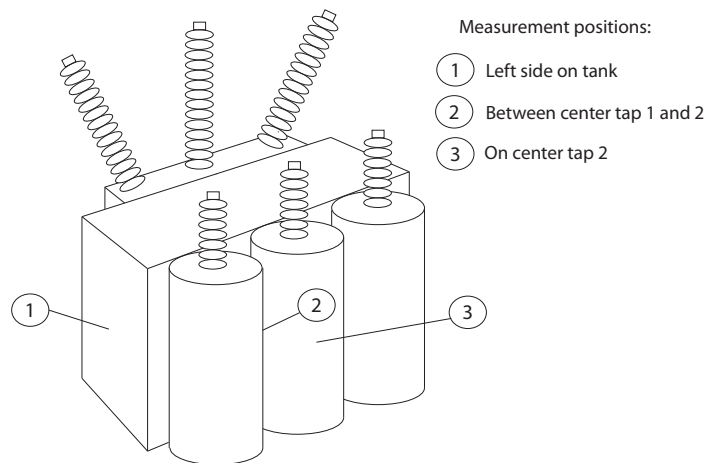
Figure 4.6: Positions of transformer vibration measurements

34
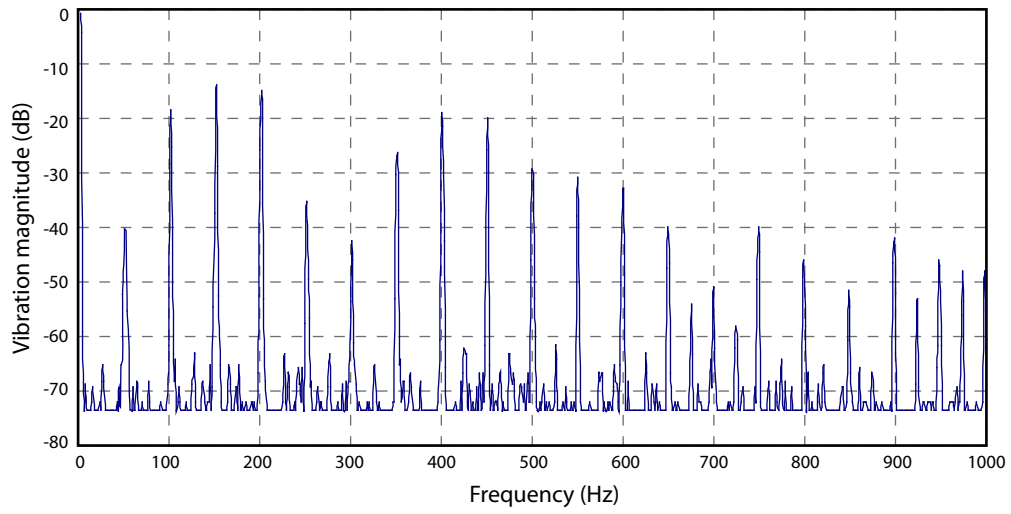
Figure 4.7: Vibration measurement at position 1 as detailed in Figure 4.6
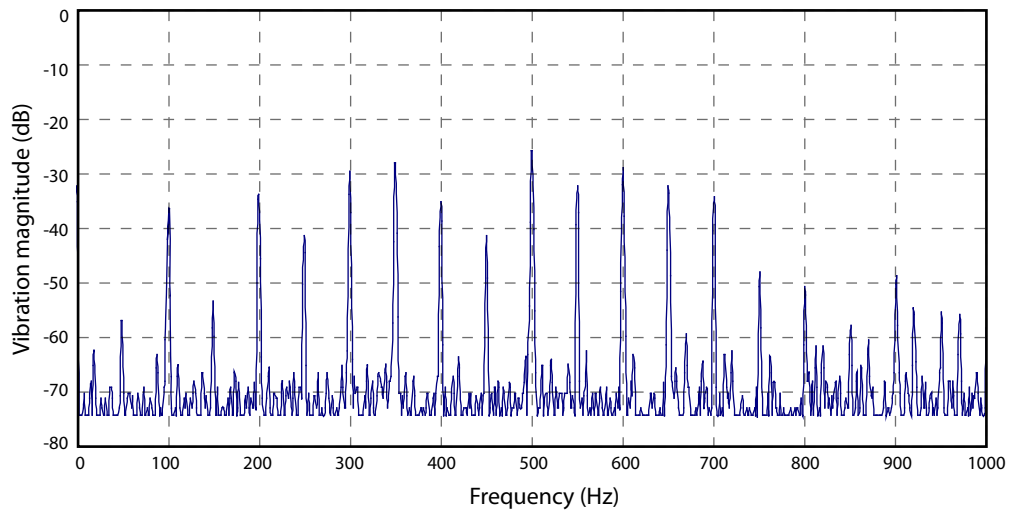
Figure 4.8: Vibration measurement at position 2 as detailed in Figure 4.6

Important fundamental vibration frequencies such as 100Hz, dropped almost 20dB[1] in magnitude from the center position to the left side of the transformer tank. It is suggested that location specific measurements be made with the actual installation of the piezoelectric generator on the power transformer. The piezoelectric generator could consequently be optimised accordingly, maximising output power at the particular position.

For all practical reasons an acceleration magnitude of 1g or 10m/s^2 at 100Hz will be used as the reference source vibration. This is considerably less than the measured vibrations stated earlier. However, it was suggested to design the power conditioning system according to a lower than average acceleration as a larger input vibration only contributes to an improved operational duty-cycle of the WSM. In other words, if a system can operate with the minimum amount of input vibration it will only benefit from larger input vibrations as the amount of energy generated to power the mote would increase.

The actual design of a piezoelectric cantilever for energy harvesting is beyond the scope of the present project. However, some of the basic theory behind piezoelectric material, generic model of mechanical-to-electrical conversion and estimated output power of the particular cantilever was needed to understand the influence that different parameters had on the generated output power.

4.5   Generic vibration-to-electricity conversion model

Figure 4.9 shows the diagram of a generic model of a mass-spring-damper for conversion of mechanical-to-electrical energy (Williams & Yates, 1995).
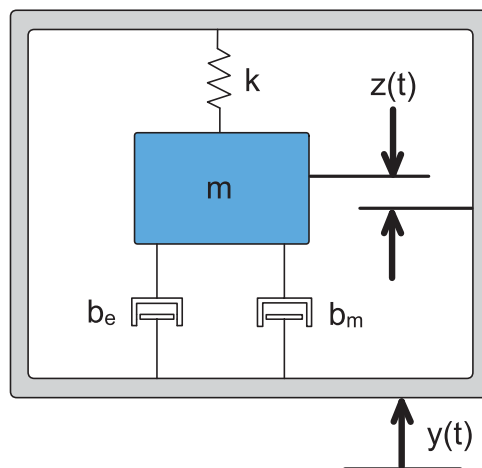
Figure 4.9: Generic conversion model redrawn from Roundy (2003)

The generator consists of an object mass, m, on a spring, k. The transducer is depicted as a damper combination of electrically induced (b_e) and mechanically induced (b_m) damping.

---

[1]0 dB is referenced to $1V_{rms}$ for all frequency magnitudes.

The reason for this is that the conversion of mechanical energy into electrical energy and visa versa damps the system. When the generator is vibrated or subjected to an external force $y(t)$, the mass will move out of phase with respect to the generator housing in a sinusoidal nature $z(t)$. The differential equation of motion for the generic model is given by (4.1) (Williams & Yates, 1995):

$$m\ddot{z}(t) + (b_e + b_m)\dot{z}(t) + kz(t) = -m\ddot{y}(t) \tag{4.1}$$

where: $z(t)$ = spring deflection

$y(t)$ = input displacement

m = mass

b_e = electrically induced damping (piezoelectric effect)

b_m = mechanically induced damping (internal friction)

k = spring constant

In converters such as piezoelectric systems the effect of the electrical transducer on the mechanical system is not necessarily linear and proportional to the velocity of the vibration. However, the conversion process will always constitute a loss of mechanical energy and can therefore be broadly seen as electrically induced damping. Even though the generic model does not accurately represent the piezoelectric converter, important conclusions can be made through its analysis.

For analysis of this model it is assumed that the mass of the vibration source is much larger than the mass of the generator. This is very true in the case of this project, as the transformer weighs considerably more than the piezoelectric generator. Secondly it is also assumed that the vibration source is an infinite source of power, meaning that the vibration source is unaffected by the movement of the generator and that the generator will not damp the vibration source. This assumption also holds true as the attached piezoelectric generator has minimal effect on the vibration of the power transformer.

There exists a net transfer of mechanical power into electrical power due to the damping of the electrical transducer. The instantaneous output power is the product of force (F) and velocity (v) experienced on the mass if F and v are both constants. When F and v are not constants, the power is given by:

$$P = \int_0^v F dv \tag{4.2}$$

With the electrically induced force $F = b_e v$, (4.2) becomes:

$$P = b_e \int_0^v v dv = \frac{1}{2} b_e v^2 \tag{4.3}$$

Replacing v in (4.3) with the electrically induced force $\dot{z}$ yields:

$$P = \frac{1}{2} b_e \dot{z}^2 \tag{4.4}$$

An analytical expression for power was derived by Roundy (2003) by solving (4.1) for $\dot{z}$ and substituting that into (4.4). The Laplace transforms were taken for the spring deflection (Z) and the input displacement (Y) from where the magnitude of output power $|P|$ was derived:

$$|P| = \frac{m \zeta_e \omega_n \omega^2 \left(\frac{\omega}{\omega_n}\right)^3 (Y_0)^2}{\left[2\zeta_T (\frac{\omega}{\omega_n})\right]^2 + \left[1 - \left(\frac{\omega}{\omega_n}\right)^2\right]^2} \tag{4.5}$$

where ζ_T is the combined damping ratio $(\zeta_e + \zeta_m)$, ω_n is the natural resonant frequency in radians per second, Y_0 is the maximum displacement magnitude of the input vibration and ω the frequency of the input vibration in radians per second.

The derivation was based on the assumption that the vibration source is a single input frequency. This assumption holds true since the input vibration frequency is concentrated at 100Hz. According to Roundy (2003) if the resonance frequency of the spring mass system matches that of the input vibration $(\omega_n = \omega)$, an expression can be obtained for maximum power generation by simplifying (4.5) to (4.6):

$$|P| = \frac{m \zeta_e \omega^3 Y_0{}^2}{4(\zeta_T)^2} \tag{4.6}$$

For a sinusiodal input vibration, the displacement (Y) can be mathematically represented by $Y_0 sin(\omega t)$. From this the acceleration is the second time derivative of the input displacement and can be expressed by:

$$\ddot{Y} = -Y_0 \omega^2 sin(\omega t) \tag{4.7}$$

The acceleration magnitude, $\left|\ddot{Y}\right|$ or commonly refered to as A, is therefore $Y_0 \omega^2$. Substituting this into equation (4.6) yielded:

$$|P| = \frac{m\zeta_e A^2}{4\omega(\zeta_T)^2} \tag{4.8}$$

where: m = proof mass (kg)

A = acceleration magnitude of input vibration (m/s^2)

ω = frequency of operation (s^{-1})

ζ_e = electrically induced damping (piezoelectric effect)

ζ_T = combined damping ratio ($\zeta_T = \zeta_e + \zeta_m$)

ζ_m = mechanically induced damping (internal friction)

It can be seen from the maximum power equation (4.8) that it is desirable to use the largest proof mass feasible for the specific application as the output power is proportional to the proof mass. With further inspection it can be revealed that the resonance peak which maximises the A^2/ω ratio has the largest potential for power generation. Therefore, even though there is often a higher peak vibration component at 300Hz than at 100Hz, the 100Hz peak is still more desirable. This is due to the A^2/ω ratio at 100Hz being roughly 3 times larger than that corresponding to 300Hz for the same levels of acceleration.

In order to calculate an expected maximum output power of the piezoelectric cantilever at the given acceleration magnitude of 10m/s^2, the parameters from (4.8) need to be obtained. All of the parameters are known except the electrical and mechanical damping. Roundy (2003) stated that the output power is optimised when the mechanical damping ζ_m is kept at a minimum and when ζ_m equals ζ_e. The electrical damping is normally a function of circuit parameters and can be designed to equal the mechanical damping if ζ_m for the system is known. In order to calculate the mechanical damping ratio, an impulse experiment was conducted. This is explained in section 4.6.

4.6 Generic conversion model verification with piezo-electric prototype

The PCFC-100 piezoelectric cantilever from Advanced Cerametrics Incorporated (2009), shown in Figure 4.10, was used to verify the generic conversion model and equation (4.8) in section 4.5. The PCF-100 transducer was also implemented in harvesting available energy from the transformer vibrations.

As mentioned earlier, the actual design of a piezoelectric transducer falls outside the scope of this project. It was therefore opted for a commercially available piezoelectric cantilever that would fit the requirements. The piezoelectric cantilever of choice consisted of two piezoelectric fibre composites (PFC) connected in series, with a thin metal shim between the two PFCs.
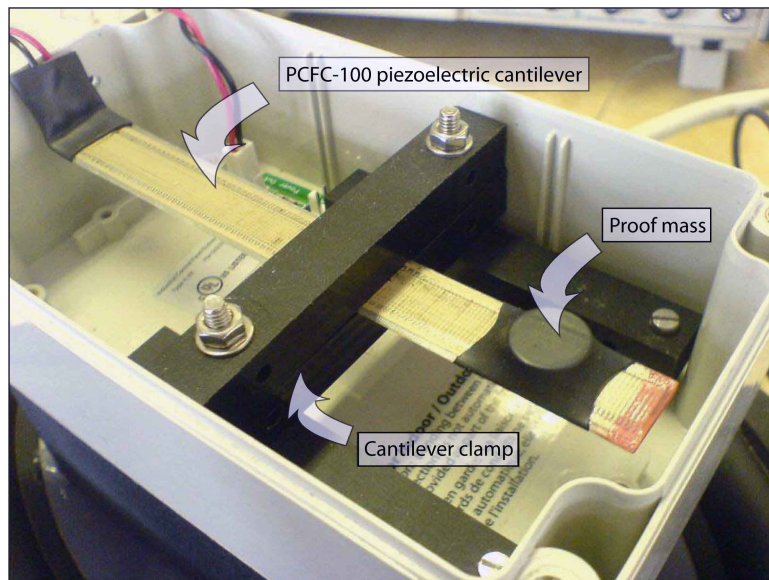
Figure 4.10: PCFC-100 Piezoelectric energy harvester

A 3g copper proof mass came fixed to the end of the PCF-100 cantilever which was clamped by nylon plastic bars as detailed in Figure 4.11.
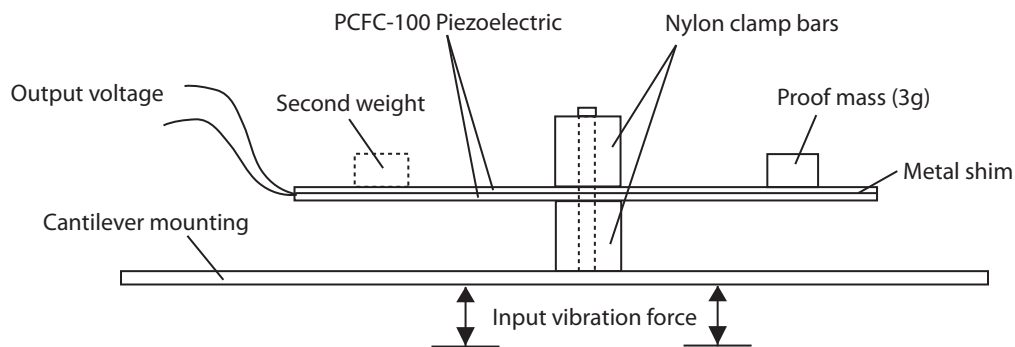
Figure 4.11: PCFC-100 cantilever configuration

The resonance frequency of the generator was originally much lower and tuned to harvest energy from vibrations around 16 - 20Hz. A variety of experiments were conducted to extract maximum power from the piezoelectric cantilever configuration at 100Hz. The resonance frequency was increased from 20Hz to 100Hz by decreasing the distance between the clamp and proof mass. In an addition to increase the output voltage from the cantilever, it was believed that by adding a second weight on the opposite side as indicated in Figure 4.11 it would enable a double cantilever configuration. However, Figure 4.12 shows the reduced output voltage of the piezoelectric cantilever at 100Hz with different second weights attached on the cantilever.

The highest output voltage was achieved by a single proof weight of 3g. The resonance frequency of the cantilever was experimentally optimised to match the reference vibration signal by decreasing the distance from the proof mass to the clamp. The graph in Figure 4.13 shows experiments conducted on the piezoelectric cantilever at different clamp positions.
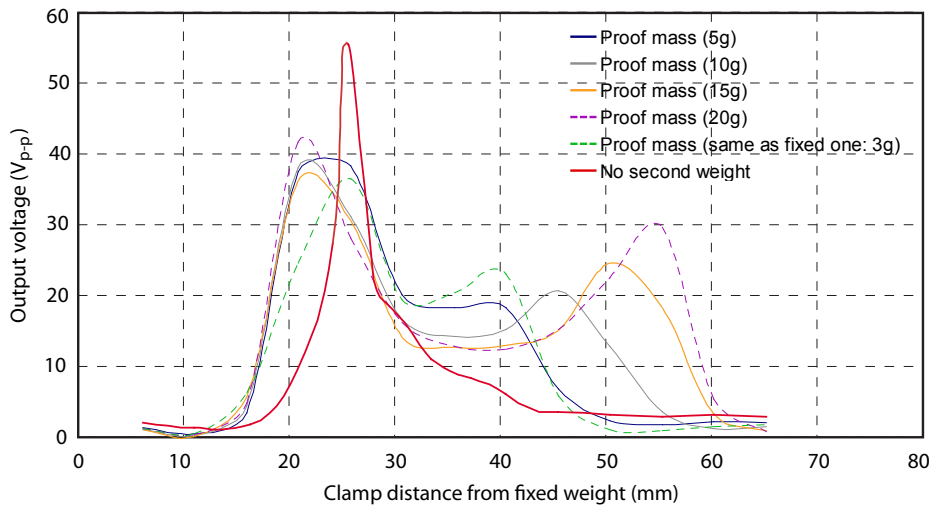
Figure 4.12: Cantilever output against clamp distance with various second weights

To achieve maximum output power, it is crucial to operate at resonance by clamping the piezoelectric generator at the correct position.
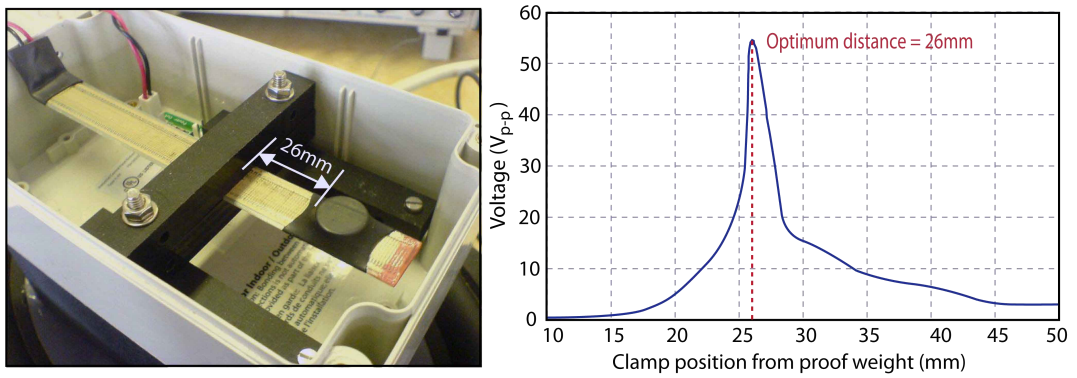
Figure 4.13: Clamping distance effect on output voltage at 100Hz

The 100Hz vibration experiments and resonance tests were simulated by feeding a signal generator through a Crest Audio® power amplifier into a speaker. A flat bed was glued onto the speaker to attach the PCFC-100 piezoelectric energy harvester box. The test setup is shown in Figures 4.14 and 4.15 with the summary of equipment used listed in Table 4.1.
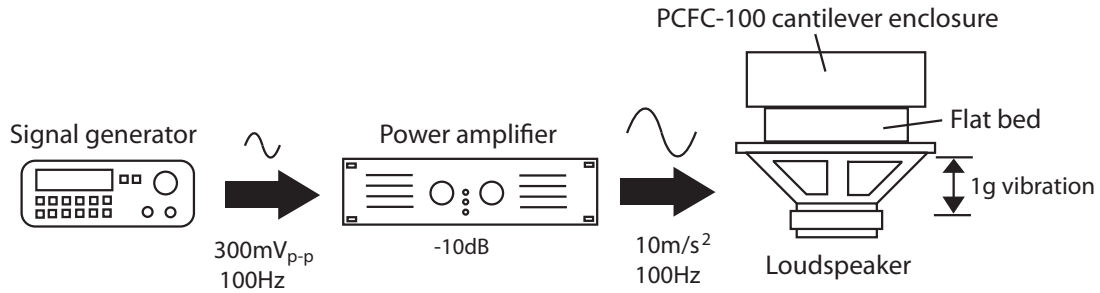
Figure 4.14: Vibration test setup for PCFC-100 cantilever
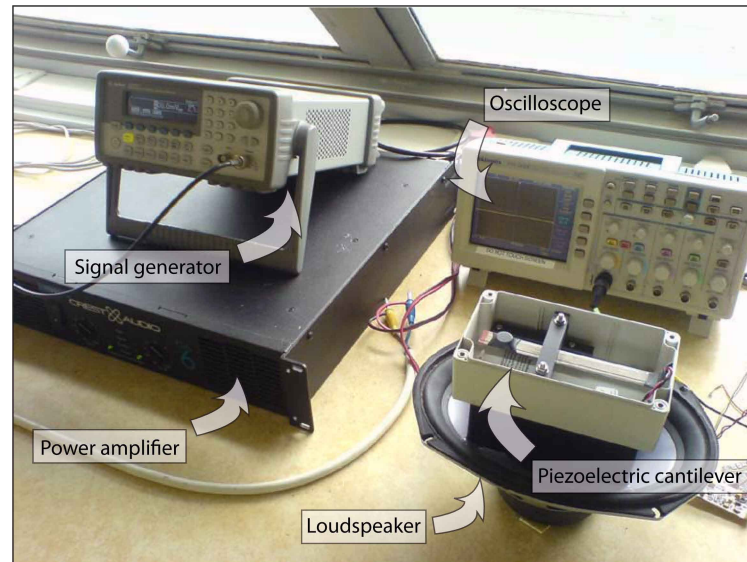
Figure 4.15: Vibration test setup

Table 4.1: Vibration test equipment

Equipment	Description
Signal generator	Agilent 33220A 20MHz Function/Arbitrary waveform generator
Power amplifier	Crest Audio® CA6 400W in 8Ω stereo power amplifier
Loudspeaker	Calibra 90W RMS 8Ω speaker
Piezoelectric	Advanced Cerametrics PCFC-100 cantilever
Oscilloscope	Tektronix® TPS 2014 100MHz digital storage oscilloscope

The piezoelectric generator was driven at a vibration frequency of 100Hz and acceleration of 10m/s². The acceleration was calibrated by the same accelerometer that measured the acceleration magnitudes on the transformer as detailed in section 4.4. As mentioned earlier the simulated vibration signal is a good representation of below average vibration frequencies and acceleration magnitudes experienced on the power transformer. The mechanical damping ratio, ζ_m, was calculated to be an average of 0.032. This was achieved by applying the reference vibration signal with a single period to the device and observing the decay of the output signal. The damped oscillation can be seen in Figure 4.16.
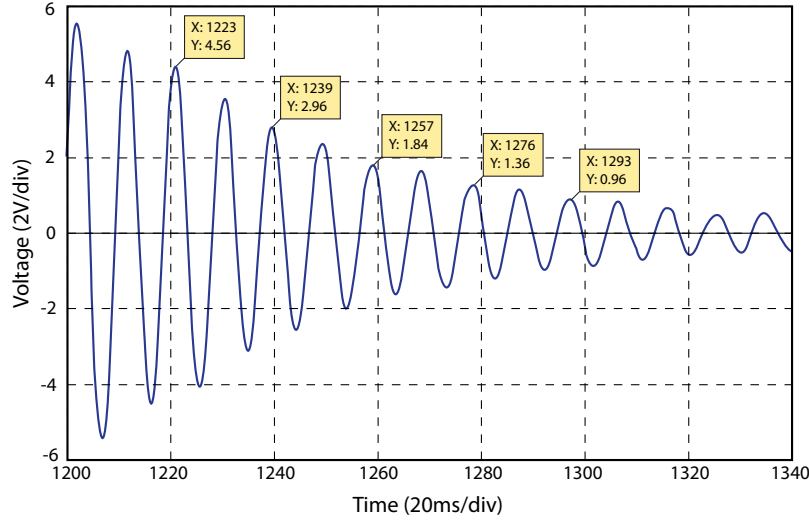
Figure 4.16: Damping of piezoelectric cantilever

In order to calculate the mechanical damping ratio, a logarithmic decrement was used (Thomson, 1972). The damping ratio is a function of two magnitudes and the number of periods as shown in (4.9).

$$\zeta_m = \frac{1}{2\pi n} ln \left[\frac{x_1}{x_2} \right] \tag{4.9}$$

where: x_1 = magnitude of a arbitrary point on the damped oscillation

x_2 = magnitude of the damped oscillation n periods later

Using the power equation (4.8), a theoretical estimation of maximum power output from the piezoelectric cantilever was calculated.

$$|P| = \frac{m\zeta_e A^2}{4\omega(\zeta_T)^2} = \frac{(0.003)(0.032)(10)^2}{4(2\pi(100))(0.032+0.032)^2} = 932\mu\text{W}$$

An acceleration magnitude of 10m/s^2 at 100Hz, proof mass of 3g and mechanical damping ratio average of 0.032 predicted a maximum power output of $932\mu\text{W}$, provided the electrical damping equals the mechanical damping ratio.

4.7 Resistive and capacitive load tests

A theoretical estimation of $932\mu\text{W}$ was predicted using the power equation (4.8). The output power of the piezoelectric transducer into a purely resistive load correlated well with the

theoretical results with a maximum output power of 897μW at an optimal load resistance of 300kΩ. Figure 4.17 shows how the maximum output power is affected under various resistive loads.
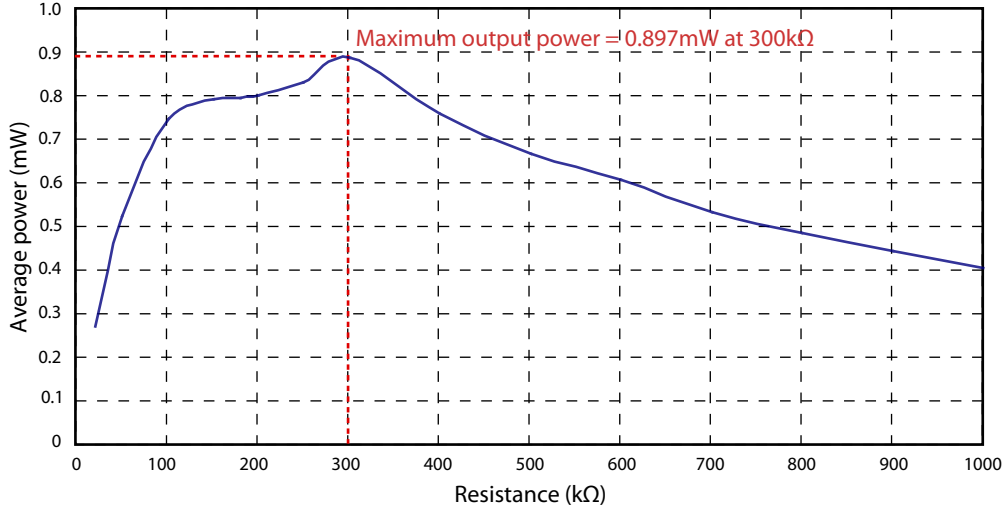
Figure 4.17: Maximum output power into purely resistive load

A purely resistive load is not a reasonable approach for an electrical load such as a WSM. The AC nature of the piezoelectric cantilever's output voltage first has to be rectified from where the energy will be stored, typically into a capacitor. This is necessary to produce a DC voltage with sufficient energy to supply a regulated voltage within the operating range of the sensor mote. Therefore, a more realistic approach would be to measure the output power into a capacitive load rather than a purely resistive one. The piezoelectric cantilever was excited with the reference vibration of 10m/s^2 at 100Hz. The output voltage from the cantilever was fed through a rectifier bridge connected to a 1000μF capacitor (C_{in}). Figure 4.18(a) shows the setup together with the output voltage accumulated across capacitor C_{in} in Figure 4.18(b).

The piezoelectric cantilever was able to charge C_{in} from 400mV to 5.12V in 38 seconds as seen in Figure 4.18(b). This constituted a collected total energy of 13.02mJ in C_{in}. The average output power of the piezoelectric cantilever can be calculated taking the amount of energy harvested and dividing that with the period over which the energy was collected. This resulted in an output power of 342.8μW into a capacitive load.

As explained by Roundy (2003) and also verified by the author, the size of the storage capacitor does not have an effect on the level of power transfer as long as the storage capacitance is two to three orders of magnitude larger than the capacitance of the piezoelectric cantilever used. The measured capacitance of the PCFC-100 piezoelectric device is between 6.5 - 7.5nF in a frequency range of 100Hz to 1kHz. The capacitance therefore does not have an effect on the power transfer since the storage capacitor used is in the mF range representing a size several magnitudes larger.

The measured output power into the capacitive load is significantly lower than for the
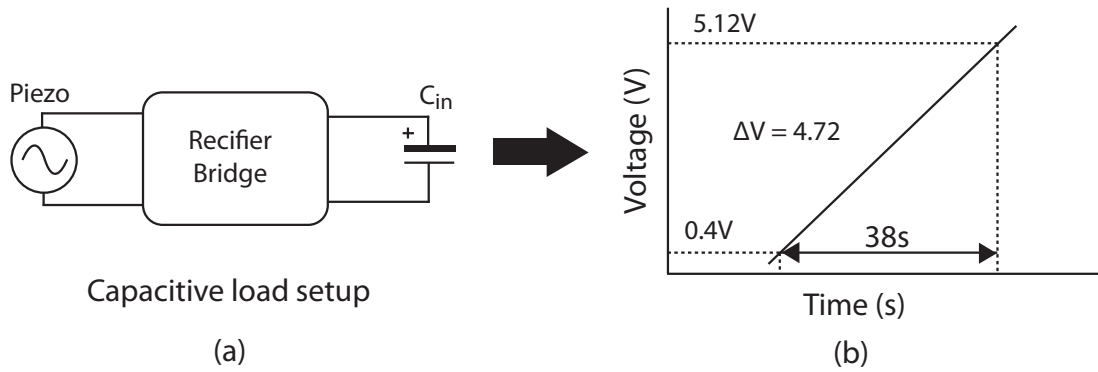
Figure 4.18: Piezoelectric cantilever output power into capacitive load

resistive load. According to Roundy (2003), the best achievable power transfer for a capacitive load is still lower than a resistive load even if the design is optimised for the capacitive load. Moreover, Roundy (2003) stated that the discrepancies between the resistive and capacitive load output powers can be largely construed to the voltage drop across the diodes present in the bridge rectifier.

This statement is supported by the various experiments conducted in this project to calculate the loss of power into a resistive load when the bridge rectifier was present in the circuit and when not. Experiments concluded that at least 60 - 75% of power was consumed by the bridge rectifier. This explained the discrepancy experienced between the measured output power into a resistive load to a capacitive load. Further research into optimising the rectifier section, would significantly improve the overall efficiency of vibration energy harvesting.

4.8 Summary

This chapter detailed that the generic vibration-to-electricity conversion model predicted an output power from the PCFC-100 piezoelectric cantilever of 932μW when subjected to the reference acceleration of 10m/s^2 at 100Hz. The output power of the piezoelectric cantilever into a purely resistive load correlated well with the generic conversion model with a maximum output power of 897μW at a load resistance of 300kΩ. The piezoelectric cantilever was capable of generating an output power of 342.8μW into a capacitive load. The performance of the piezoelectric generator would be further evaluated in conjunction with the vibration energy harvesting subsystem in chapter 6.

Chapter 5

Solar energy harvesting

5.1 Energy harvesting from the environment

Some of the most common environmental and ambient energy sources include solar, radio frequency (RF) and thermal radiation as well as natural elements such as wind and rain. Radiation may come from natural energy sources such as the sun or artificial energy sources such as an RF transmitter. Thermal energy depends on the existence of a temperature gradient while wind presents a feasible option to harvest energy in an environment subjected to high volumes of wind. With the power transformer situated outdoors, the WSMs are subjected to high levels of available solar energy.

5.2 Introduction to photovoltaic technology

The principle of converting sunlight into electricity is called the photovoltaic (PV) effect, where "photo" refers to light and "voltaic" to voltage. Light consists of photons whose energy depends upon the wavelength. Some semiconductor materials such as crystalline silicon or amorphous silicon exhibit a property known as the PV effect. These materials absorb the photons and release electrons. The free electrons result in an electric current producing energy for an electrical load. The PV effect was discovered by Becquerel in 1839. Further development in the 1950's enabled the first solar cell application to be implemented in the space industry. This formed the basis for current commercial applications (Flipsen, 2005).

Solar radiation varies over the earth's surface due to weather conditions and location (longitude and latitude). For each location there exists an optimal inclination angle and orientation of the solar cells in order to obtain the maximum radiation on the surface of the solar cell. The power conversion efficiency of a solar cell is defined as the ratio between the solar cell output power and the solar power (irradiance) imposed on the solar cell surface.

Harvesting energy from solar radiation is becoming increasingly important as a renewable energy source since it offers many advantages such as converting freely available energy, requiring no fuel costs, is non-polluting, requires little maintenance and emits no noise (Jiang, Polastre & Culler, 2005).

5.3 Principle of power generation

The principle of power generation consists of the utilisation of the photovoltaic effect of semiconductors. A Silicon (Si) plate is exposed to sunlight that contains photons. When these photons hit the surface of the semiconductor, energy frees electron-hole pairs. Each photon with enough energy will free exactly one electron which results in one free positive charged hole. The negatively charged electrons move to the n-type semiconductor while the positively charged holes move to the p-type semiconductor. They collect at both electrodes to form a potential difference. Solar cells are made by bonding together p-type and n-type semiconductors. When the n- and p-sides are short-circuited, electrons will flow through the connected path to the p-side. At the p-type side these electrons will recombine with the holes (Flipsen, 2005). This principle enables electron flow producing a current that can be transferred to an outside application or load.
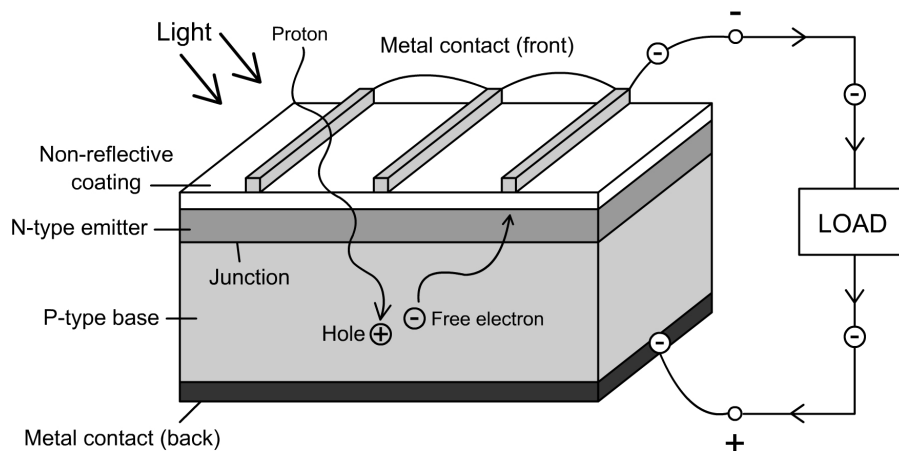
Figure 5.1: Basic operation of photovoltaic cell redrawn from Flipsen (2005)

5.4 Output characteristics of solar cells

The output characteristics of solar cells are expressed in the form of voltage-current (V-I) and voltage-power (V-P) curves. These curves are produced by varying a load resistance from zero to a high impedance and measuring the current and voltage. Solar cells are characterised by two parameters, the open-circuit voltage (V_{OC}) and short-circuit current (I_{SC}). These form the x- and y- intercepts of the V-I curve. It is clear from the V-I curve in Figure 5.2 that

a solar cell behaves as a voltage limited current source as opposed to a battery which is a voltage source.
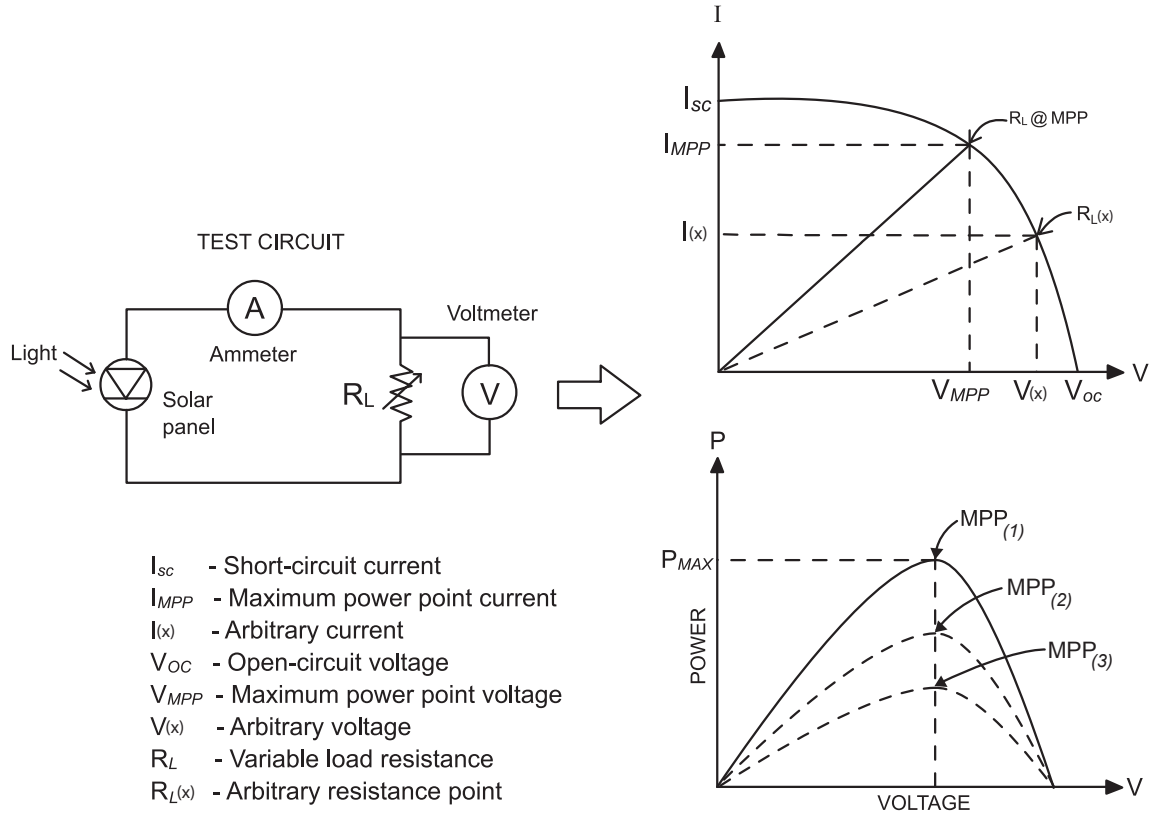
Figure 5.2: Test circuit and V-I and V-P curves adapted from Panasonic (1998).

The point at which the V-I curve and resistance (R_L) intersects is the operating point of the solar cell. The voltage and current at this point is V_{MPP} and I_{MPP} respectively. The product of V_{MPP} and I_{MPP} produce a maximum power point (MPP) for the solar cell at the respective solar radiation. The MPP is a function of solar radiation and will vary directly proportionate with respect to light intensity as detailed by arbitrary light intensity levels given by $MPP_{(1)}$, $MPP_{(2)}$ and $MPP_{(3)}$ in Figure 5.2.

Due to the its current source like behaviour, it is difficult to power a target system such as a WSM directly from the solar panel, since the supply voltage would depend on the time varying load impedance. Hence, an energy storage element, such as a battery or supercapacitor is used to store the energy harvested by the panel to provide a stable voltage to the particular load (Raghunathan *et al.*, 2005).

The building block of a PV array is the solar cell. The solar cell in its simplest form is a p-n junction semiconductor as shown in Figure 5.3. According to Huang *et al.* (2005), the output voltage and current or V-I characteristics of a PV array are given by (5.1):

$$I = I_{SC} - I_d \left\{ e^{\left[\frac{q(V+R_sI)}{nkT_K} \right]} - 1 \right\} - \frac{V + R_sI}{R_{sh}} \tag{5.1}$$
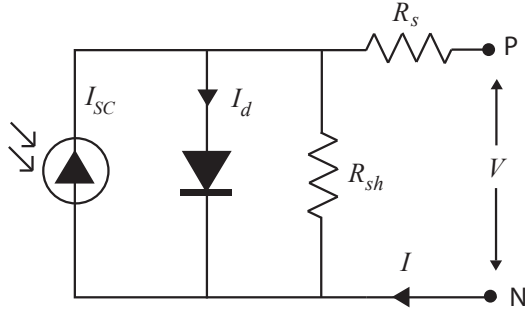
Figure 5.3: Equivalent electrical circuit of a PV array redrawn from Huang *et al.* (2005)

where V and I represent the output voltage and current respectively; R_s and R_{sh} are the series and shunt resistance of the cell; q is the electron charge (1.602×10^{-19}C); I_{SC} is the photon-generated current; I_d is the reverse saturation current; n is a dimensionless factor; k is Boltzman's constant (1.381×10^{-23}J/K), and T_K is the temperature in Kelvin (K).

5.5 Solar panel characteristics

In the process of doing research on various solar panels, several aspects influenced the choice of solar panel such as output voltage, physical size, operating current and life expectancy.

The solar panel of choice was the MP3-37 flexible solar panel from PowerFilm®, shown in Figure 5.4. The solar panel was chosen for its good performance to size ratio. The panel has a V_{OC} of 4.1V and I_{SC} of 60mA with a maximum operating current of 50mA. The flexible solar panel's physical dimensions are 114mm x 37mm with a thickness of 0.2mm. The MP3-37 solar panel proved to be a good choice for remote wireless sensing applications, due to features such as small form factor, lightweight (1.2g), flexible and maximum output power (150mW).
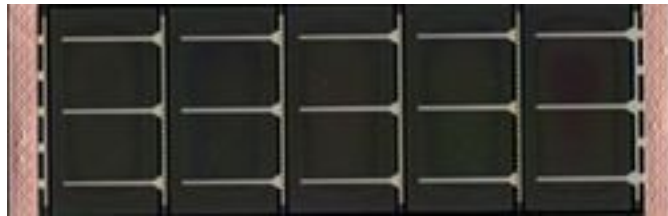
Figure 5.4: MP3-37 flexible solar panel from PowerFilm® (2009)

5.5.1 Temperature characteristics

The performance of solar cells is a function of temperature. The short-circuit current (I_{SC}) increases and the open-circuit voltage (V_{OC}) decreases as the ambient temperature rises as

detailed in Figure 5.5. The V_{OC} decreases at a much higher rate than what the I_{SC} increases. Hence the maximum output from the solar cell drops with an increase in temperature. Solar cells are designed so that the operating current peaks at around room temperature and deviate slightly below and above according to temperature changes (Panasonic, 1998).
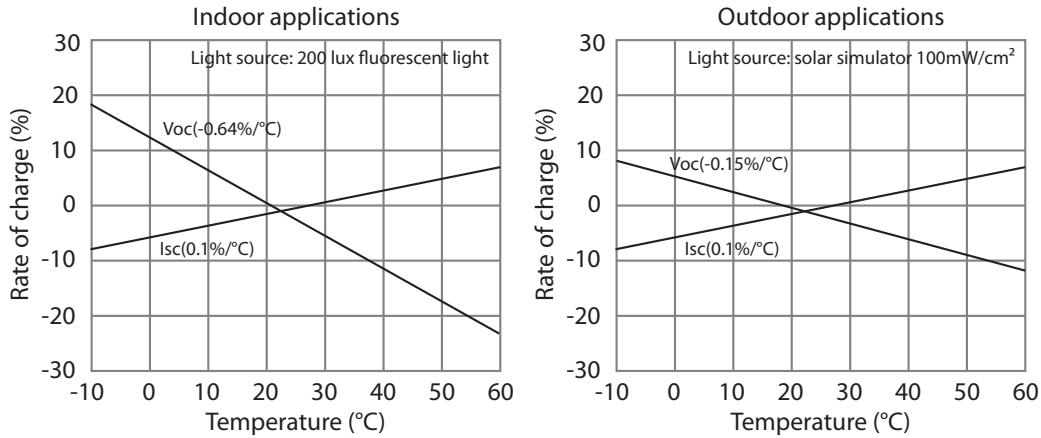
Figure 5.5: Temperature characteristics of solar cells redrawn from Panasonic (1998)

5.6 Maximum power point tracking (MPPT)

Due to the essentially limitless nature of the energy source it is desirable to harvest as much energy as possible from solar cells, this ability being particularly important in cloudy conditions. Direct connection of the solar cell to converters, batteries and supercapacitors prevent maximum power transfer, due to impedance mismatch. The purpose of a maximum power point tracker (MPPT) is to perform a load transformation to enable the solar cell to operate at its optimal point (Duncan, 2005).

PV modules still have relatively low conversion efficiencies. It is therefore especially important to harvest the maximum amount of available energy from any solar panel. The amount of power generated depends on the operating voltage of the solar cell array. A solar panel's maximum power point (MPP) varies with the level of solar radiation and temperature. As mentioned in section 5.4, the V-I and V-P characteristic curves specify a unique operating point at which maximum power is delivered. At the MPP, the solar panel also operates at its highest efficiency.

Consequently, many methods have been developed to effectively determine and track the MPP (Huang *et al.*, 2005). MPPT can be divided into two broad categories, namely digital and analogue power point tracking. Each having their respective advantages and disadvantages.

5.6.1 Digital MPPT techniques

A common digital MPPT algorithm that is extensively used is the perturbation and observation (P&O) method. Figure 5.6 presents a simplified flow chart of the P&O algorithm. It operates by periodically comparing two points, the current operating point and the preceding point. It does this by calculating the instantaneous power (`P_new`) and comparing that to the previously logged power (`P_old`). If the newly calculated power value is larger than the older power value, the new value replaces the old. The duty-cycle (`Duty`) of the system, typically that of the regulator, is then increased (`Duty`$^+$) by a predetermined constant which in turn increases the solar output voltage. Conversely, if the new power value is lower, the duty-cycle is reduced (`Duty`$^-$), decreasing the solar output voltage. Therefore by adjusting the duty-cycle, the system is continually searching for the maximum power point.

Start

Set Duty out

Read V, I

P_new = V*I

P_new > P_old

No

Duty = Duty$^-$

Yes

P_old = P_new

Duty = Duty$^+$
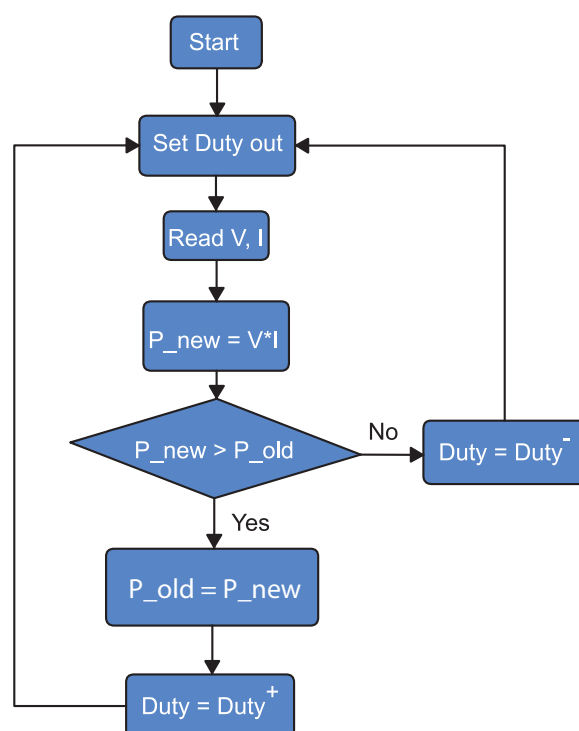
Figure 5.6: Perturbation and observation flow chart algorithm redrawn from Huang *et al.* (2005)

However, this algorithm experiences a loss of PV power in rapidly changing solar radiation. Huang *et al.* (2005) proposed a three-point weight comparison method to eliminate this problem.

A real-time Estimate-Perturb-Perturb (EPP) algorithm for MPPT control was developed (Yafaoui, Wu & Cheng, 2007). The proposed system incorporated digital signal processing techniques for improved efficiency and tracking time. The system is however a promising MPPT control scheme primarily for high power residential PV systems.

A low-power MPPT method was proposed that maximises the energy harvested from small, low power solar cells specifically catered for wireless sensor networks (Alippi & Galperti,

2008). High efficiency was achieved by an ad hoc adaptive algorithm that was particularly effective in critical weather conditions. Although the system featured low-power MPPT, the design required an external microprocessor additional to the wireless sensor mote to run the adaptive MPPT algorithm.

A proposed system named *Everlast* implemented a feedforward, pulse frequency modulated (PFM) converter and open-ciruit solar voltage technique for MPPT (Simjee & Chou, 2006).

Digital MPP trackers are generally more accurate than their analogue counterparts by implementing software algorithms to effectively track maximum power but with the disadvantage of being slower and typically demanding more power. Digital MPPT is more widely implemented in high power applications where the power consumption of the MPPT circuitry itself plays a trivial part compared to the output power generated by the solar energy source. In applications such as low power WSMs this is a completely different situation, since the MPPT circuitry may contribute to a large portion of the overall consumed power.

5.6.2   Analogue MPPT techniques

An analogue MPPT was proposed by introducing a dynamic process for reaching the maximum power point of a solar cell (Midya, Krein, Turnbull, Reppa & Kimball, 1996). The system tracked maximum power transcients on a time scale of a few milliseconds with information gathered from the natural switching ripple instead of external perturbation. Although the system was achieved with a simple analogue control scheme, the design featured a large number of discrete semiconductors. Implementing the proposed design in a low power system such as WSNs would not be feasible.

A trade-off needs to be made regarding accuracy of tracking versus power consumption. Also it is desirable that the wireless module still efficiently harvests maximum energy even when the mote is inactive in a low power sleep mode between monitoring and data transmissions.

With this conclusion, it was decided to design an analogue MPPT circuit that would allow tracking completely independent of the state of the mote. The sensor mote can therefore be in any low power mode or even completely off for that matter and the power management system (PMS) will still harvest available energy. The maximum power point tracking may not be as accurate but in the case of power consumption of analogue circuitry and independent operation of the MPPT from the sensor mote, the analogue MPPT proves to be more beneficial. This was verified and explained in more detail in chapter 6 section 6.6.2.

5.6.3 Constant voltage fraction MPPT

As mentioned in section 5.4, the V-I and V-P characteristic curves of the solar panel are such that a voltage exists for which maximum power can be extracted from the solar panel at a particular light intensity. The analogue MPPT method pursued in the present project is constant voltage fraction (Park & Chou, 2006). This method assumes that the maximum power point voltage (V_{MPP}) is at a constant fraction (k) of the solar panel's open-circuit voltage (V_{OC}) at a specific solar radiation as stated in equation (5.2).

$$V_{MPP} = kV_{OC} + c \tag{5.2}$$

where c is the offset of the linear fit.

In order to determine the fraction constant k, a linear fit or straight line average needs to be made from the calculated maximum power point voltages. MPP tests were conducted on the solar panel at various open-circuit voltages. The circuit used to perform the test was similar to the one shown in Figure 5.2 with the load resistance R_L being a 1kΩ potentiometer. Under incremental light intensities, the resistance of R_L was varied and the voltage across it was measured. Typical data measured when performing the test can be seen in Table 5.1.

Table 5.1: Solar panel performance with V_{OC} = 3.945V

Resistance (Ω)	Voltage (V)	Current (mA)	Power (mW)
100.3	0.986	9.830	9.692
200.2	1.895	9.465	17.937
230.1	2.175	9.452	20.558
260.7	2.642	10.13	26.774
290	2.942	10.14	29.846
301.6	3.079	10.20	31.433
399.8	3.456	8.644	29.874
501	3.619	7.223	26.142
601	3.686	6.133	22.606
700	3.731	5.33	19.886
803	3.754	4.674	17.549
901	3.761	4.174	15.699

The table lists values with V_{OC} of the solar panel at 3.945V. With the given data of Table 5.1, the voltage across the load and output power versus load resistance can be plotted respectively as shown in Figures 5.7 and 5.8. With V_{OC} at 3.945V the solar panel produced a maximum output of 31.433mW at a load resistance of 301.6Ω. From Figure 5.8 it can be clearly seen that a maximum power point exists and that the solar panel does not necessarily generate a larger output power with a higher voltage.

In order to determine the constant k, the experiment was repeated at incremental light intensities producing different maximum power point voltages. With enough data collected
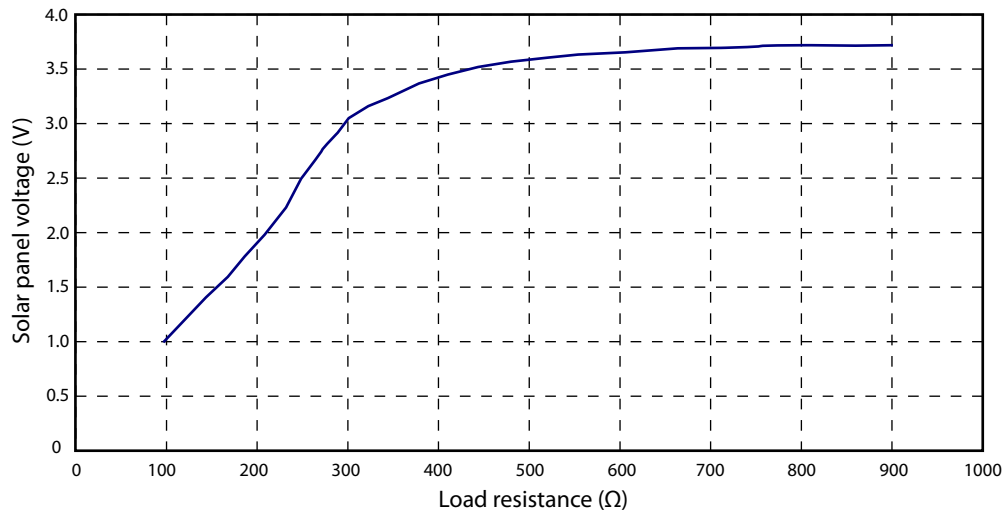
Figure 5.7: Measured output voltage of solar panel for various resistive loads
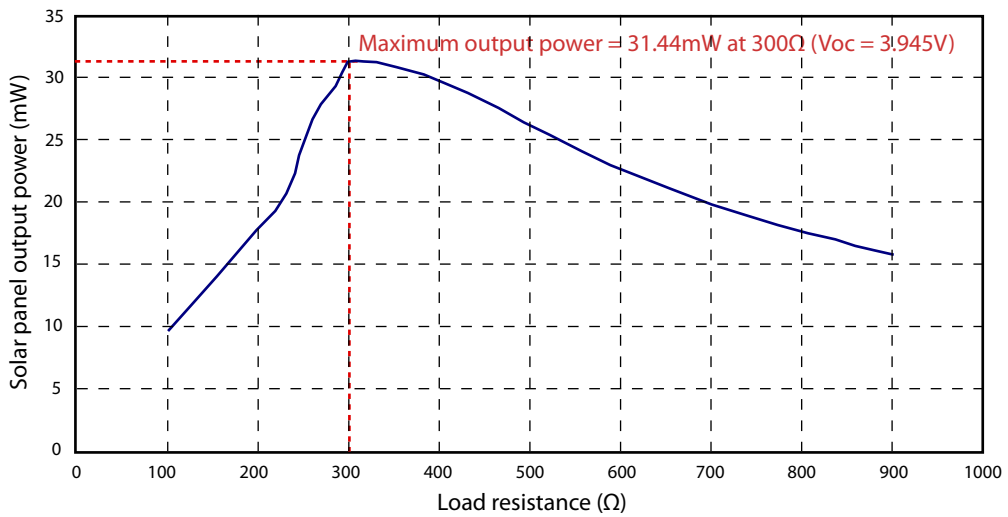
Figure 5.8: Measured solar panel output power for various resistive loads
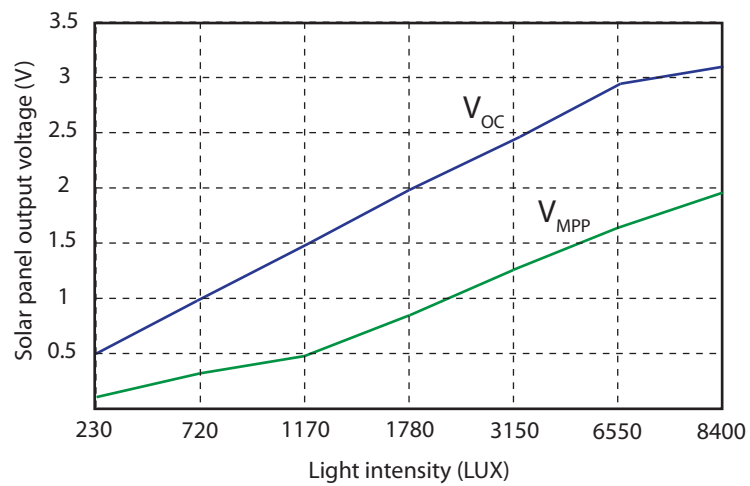
Figure 5.9: Solar panel's V_{OC} and V_{MPP} at different light intensities

Figure 5.9 was plotted, showing how V_{OC} and V_{MPP} functioned across different light intensities. From Figure 5.9 the linearity between V_{OC} and V_{MPP} is evident supporting the MPPT method of constant voltage fraction. The data points in Figure 5.9 were replotted with V_{MPP} as the y-axis and V_{OC} as the x-axis to produce the data graph in Figure 5.10. The data points revealed the constant (k) for the given open-circuit voltages. The gradient of the data graph was approximated across the open-circuit voltage range to determine k.

Figure 5.10 shows the linear fit across the data points done in MatLab®. It was necessary to calculate a linear fit to approximate the constant fraction (k). The gradient or k of the straight line was calculated to be 0.66. The value 0.66 signifies the average scaled fraction of V_{OC} that will produce maximum power output from the solar panel in a range of 1V to 3.5V. The MPPT circuitry that would force the solar panel to operate at 66% of it's open-circuit voltage (V_{OC}) will be discussed in chapter 6 section 6.6.
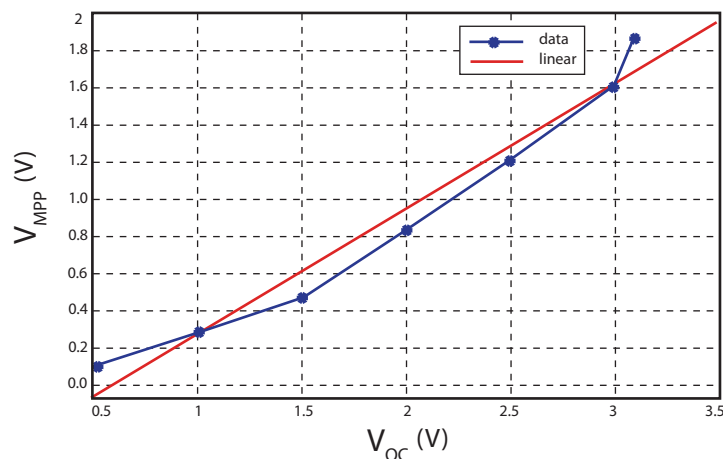
Figure 5.10: Linear fit of MPP data to determine constant k

Constant fraction voltage allowed MPPT to be implemented by monitoring only the solar panel voltage. Simple analogue circuitry, to be discussed in section 6.6, can therefore be implemented without the need for measuring current. However, it should be noted that the accuracy of this technique is dependent on the testing of the particular solar panel and that efficient maximum power point tracking may deviate when using different solar panels from the type described in section 5.5. Furthermore, this method of MPPT is also not adaptable to changing temperatures or internal changes to the solar panel over time. Nevertheless, this technique allowed for independent operation from the sensor mote, a feature significant to enable energy harvesting when the mote is in a sleep or shutdown mode.

5.7   Capacitive load test

As in the case of the piezoelectric generator, a purely resistive load is not a realistic approach. The solar panel would first charge a small input capacitor, from where the accumulated

energy would be fed through a step-up DC-DC switching converter charging the storage supercapacitors. Detailed circuit operation will be explained in chapter 6 section 6.6.

The same setup as for the piezoelectric cantilever was used for calculating output power into a capacitive load. However, due to the nature of the solar panel producing a DC output voltage, the bridge rectifier was removed as shown in Figure 5.11(a).
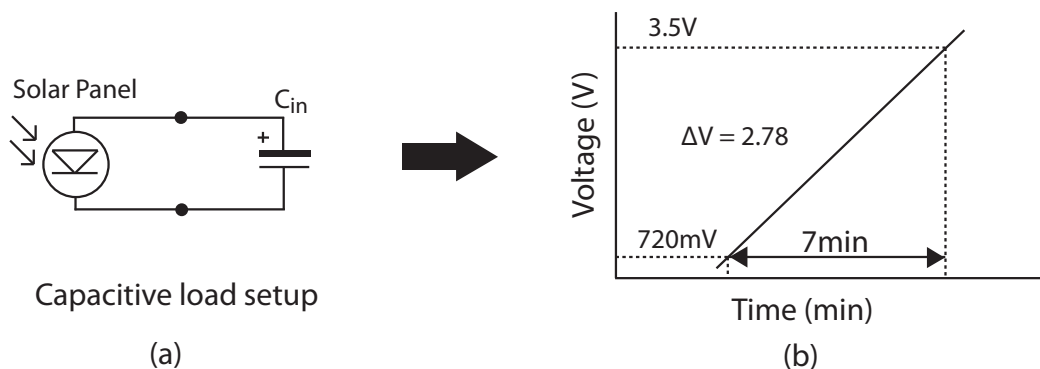
Figure 5.11: Solar panel output power into capacitive load

The solar panel harvested typically one order magnitude more energy than the piezoelectric cantilever. Therefore, C_{in} was increased to 1F allowing a longer charging time to calculate the output power more effectively. The solar panel was able to charge C_{in} from 720mV to 3.50V in 7 minutes as shown in Figure 5.11(b). The solar panel was subjected to direct sunlight and produced an open-circuit voltage (V_{OC}) of 3.69V. A total of 5.86J of energy was collected in C_{in}. The output power of the solar panel over a period of 7 minutes could be calculated from the amount of energy collected and resulted in 13.97mW of power delivered into a capacitive load.

5.8   Summary

To conclude, the solar panel produced a maximum output power at 66% of its open-circuit voltage with relative linearity in a voltage range of 1V to 3.5V. An output power of 13.97mW into a capacitive load with a V_{OC} of 3.69V was achieved. The performance of the solar panel would be further evaluated in conjunction with the solar energy harvesting subsystem in chapter 6.

Chapter 6

Power Management System Design

The characteristics and power output capabilities of both the piezoelectric cantilever and the solar panel were determined and discussed in chapters 4 and 5 respectively. With the knowledge of experimental data gathered from these two energy sources, the prototype of a power management system can now be designed. This chapter details the development of such a system.

6.1 Related work

Raghunathan *et al.* (2005) presented *Heliomote*, a proposed energy harvesting system that had a solar panel directly connected through a diode to two AA type NiMH batteries. Energy harvesting could only occur when the solar panel's output voltage was 0.7V higher than that of the battery. *Heliomote* featured no MPPT and would draw current from the battery even when abundant power from the solar panel was available if the battery voltage was higher than the solar panel's voltage.

A system called *Prometheus*, highlighted by Jiang *et al.* (2005), had a solar panel that charged a supercapacitor as a primary buffer and a Li-Po battery as secondary buffer. Powered by the supercapacitor the WSM would only draw current from the battery when the level of the primary buffer was less than a determined threshold. This feature enabled extended operating life of the battery. However, the solar panel was directly connected to the supercapacitor restricting the solar voltage to the supercapacitor voltage. As a result, the voltage deviated substantially from the MPP. In addition, all control tasks for energy harvesting were managed by the microcontroller of the WSM prohibiting low-power and sleep states.

Everlast, proposed by Simjee & Chou (2006), had a solar panel and a large supercapacitor with no secondary battery. The solar panel charged the supercapacitor while tracking it's MPP. The system, not limited to the operating life of the battery, showed improved harvesting

efficiency to that of *Prometheus*. However, the MPPT algorithm required a microcontroller for operation.

Park & Chou (2006) presented *Ambimax*. This design offered a modular approach by managing multiple power sources such as solar and wind. Energy from these sources was stored in a capacitor array and would charge a Li-Po battery when sufficient power was available. *Ambimax* was able to autonomously track the MPP of each power source independently from the WSM. Performance abilities would however deteriorate over time due to limitations such as number of recharge cycles of the battery, questioning true long-term sustainability.

6.2 System overview

Figure 6.1 gives a block representation of the proposed power management system. The system is capable of harvesting energy from solar radiation (E_e) and vibration (E_t). E_e refers to the solar energy harvested from the environment and E_t the vibration energy harvested from the transformer.
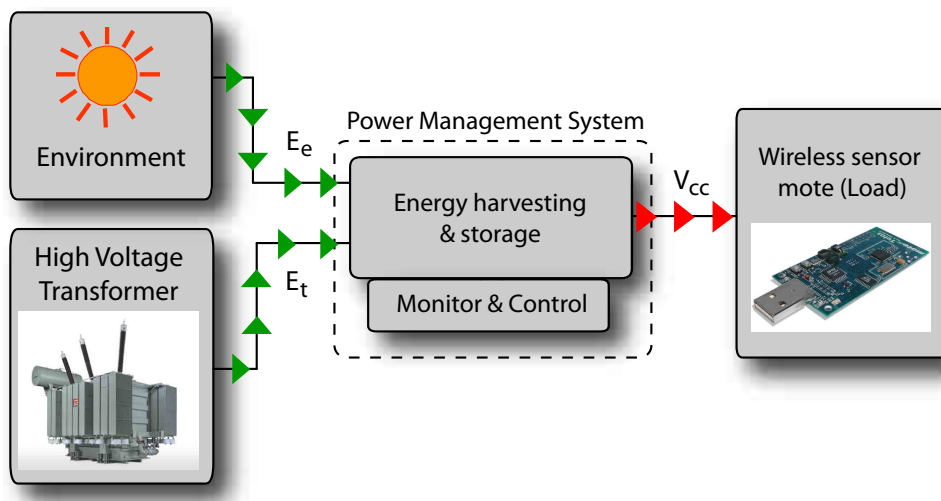
Figure 6.1: System overview

Both E_e and E_t are harvested through their respective converters and stored separately. It should be noted that the monitoring and controlling of the power management system is completely independent from the wireless sensor mote and not reliant on an external microcontroller like in previous designs. Therefore, the system is capable of efficiently harvesting energy as well as producing a regulated output suitable for the load, in this case the wireless sensor mote. This feature also allows the wireless sensor mote to go into low-power sleep states while energy is still being harvested and stored. Due to circuit configurations such as step-up voltage regulators and comparators, the system is capable of harvesting energy even when E_e and E_t are much lower than the stored energy.

To simplify the explanation of the overall system, the solar and vibration designs will

be looked at individually. The next section will first clarify some concepts and principles of operation fundamental to the understanding of the broader design of the system.

6.3   Architecture of power management system

One of the ideas behind the design of the energy harvesting power management system was to develop a generic system. This was achieved through expandability so that additional harvesting sources may be introduced to the system with minimal effect on existing harvesting subsystems.

The block diagram shown in Figure 6.2 highlights the hardware architecture of the power management system. It can be divided into two subsystems namely Energy Harvesting (EH) and Storage Capacitor Array (SCA). The EH subsystem can be further separated into the energy transducer (solar panel, piezoelectric cantilever, etc.) and the regulation circuitry for each respective ambient power source. The use of an SCA system allowed a modular approach in that various EH subsystems could be added to the overall system.
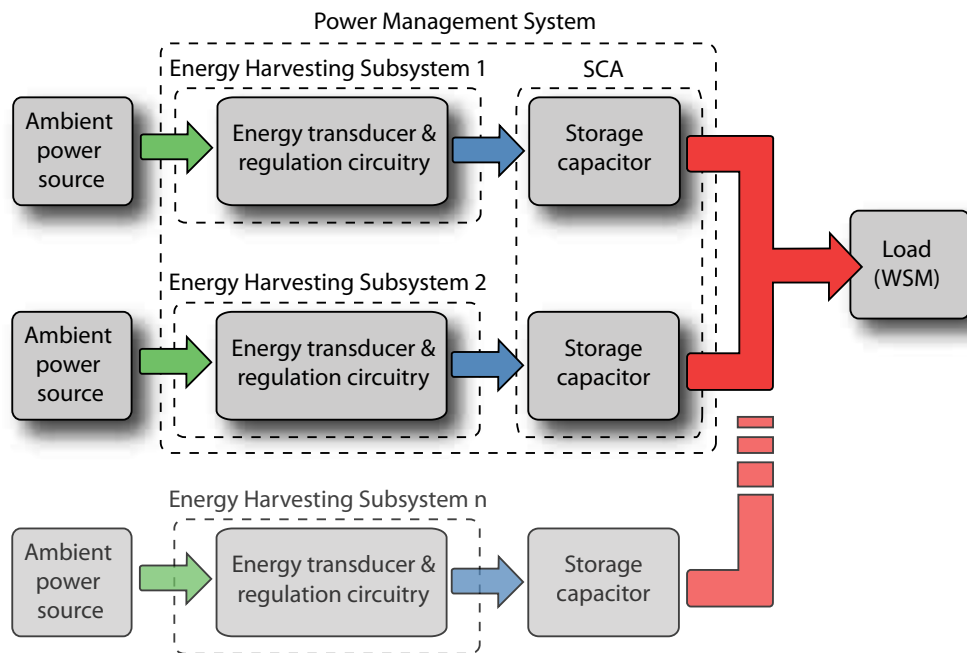
Figure 6.2: System architecture

Each EH subsystem harvests and charges its own storage capacitor independently. The SCA consists of different sized storage capacitors connected in parallel with diodes coupled from each storage capacitor to the load to prevent capacitors charging each other. Each capacitor is sized according to the output power of the ambient power source. The storage capacitor of the piezoelectric cantilever is significantly smaller in capacitance than the solar panel's storage capacitor due to the larger output power of the solar panel. This is necessary to allow the smaller harvesting sources to reach the operating voltage and contribute to the

overall system and not only the larger harvesting sources. The SCA therefore consists of different sizes of storage capacitors connected in parallel. Although not detailed in Figure 6.2, diodes are coupled from each storage capacitor to the load to prevent capacitors charging each other.

The load is solely powered by the SCA with no secondary battery connected to the system. As discussed in section 3.9, the incorporation of batteries into the design would not enhance the longevity of the proposed system due to limited recharge cycles, operating life and additional charging circuitry.

6.4   Load assessment

The application load directly influences the selection of components for the design. The power consumption of a sensor module is not just the microcontroller and radio, but also the auxiliary components and power management circuitry quiescent currents. Typical sensor motes collecting environmental data will alternate between a low-power state about 99% of the time with brief high-power active periods (Taneja, Jeong & Culler, 2008).

The proposed energy harvesting system was designed to cater for the popular TelosB WSM as detailed in section 2.3. The WSM operated on TinyOS, an open source operating system designed for wireless embedded sensor networks (TinyOS, 2004). TinyOS operating on the TelosB mote enabled a low-power operating profile by automatically entering into the low-power modes, making the TelosB platform an attractive choice for solar and vibration energy harvesting. TelosB features low sleep currents and fast wake-up times, enabling harvested energy to be stored more quickly and used for more operations. Capabilities as well as typical power consumption modes of the TelosB mote are listed in Table 6.1.

To ensure sustained operation, as stated by Penella & Gasulla (2007), the following condition needs to be true:

$$\bar{P}_g \geq \bar{P}_c \tag{6.1}$$

where $\bar{P}_g$ and $\bar{P}_c$ are the generated and consumed mean power respectively. The consumed mean power of the sensor mote can be approximated by the typical sleep consumption plus the active power consumption scaled by the operating duty-cycle. Therefore, with a predetermined duty-cycle (D) the required generated mean power is given as:

$$\bar{P}_g \geq (1 - D)P_{sleep} + D.P_{active} \tag{6.2}$$

Table 6.1: TelosB mote specifications and power consumption adapted from Polastre *et al.* (2005)

Microcontroller (MCU)	
Type	TI MSP430
Program memory (kB)	48
RAM (kB)	10
Active Power (mW)	3
Sleep Power (μW)	15
Wakeup Time (μs)	6
Non-volatile Storage	
Type	ST MP25P80
Protocol Type	SPI
Size (kB)	1024
Communication	
Programming Interface	USB
Transceiver Radio	CC2420
Data rate (kbps)	250
Modulation Type	O-QPSK
Radio Encryption Support	128-bit AES
Integrated Sensors	
Temperature & Humidity Sensor	SHT11
Photosynthetic Active Radiation Sensor	S1087
Total Solar Radiation Sensor	S1087-01
Operation	
Minimum Voltage (V)	1.8*
Mote Standby (RTC on) (μA)	5.1
MCU Idle (DCO on) (μA)	54.5
MCU Active (mA)	1.8
MCU + Radio RX (mA)	21.8
MCU + Radio TX (0dBm)(mA)	19.5
MCU + Flash Read (mA)	4.1
MCU + Flash Write (mA)	15.1
Radio Wakeup (μs)	580
Power Consumption	
Receive Power (mW)	38
Transmit Power at 0dBm (mW)	35
Total Active Power (mW)	41

* Voltage must be at least 2.7V when programming the microcontroller flash or external flash memory.

Assuming a 1% duty-cycle according to Taneja *et al.* (2008), with an active power consumption of 41mW and a sleep consumption of 15μW as listed in Table 6.1. The generated mean power would have to be equal or more than 425μW for sustained operation. With many supercapacitors having a maximum operating voltage of 2.5V, supercapacitor designs are feasible since the TelosB mote can operate down to 1.8V. A TelosB mote can effectively operate over 2 days on a single charge of a 2.5V 50F supercapacitor with the above assumptions from (Polastre *et al.*, 2005).

For ease of explanation, the prototype design was subdivided into vibration and solar energy harvesting and described in the following sections 6.5 and 6.6 respectively .

6.5   Vibration Energy Harvesting (VEH) subsystem

The output voltage produced by the piezoelectric generator is AC and varies depending on the magnitude of the vibration source and is therefore not suitable to power the WSM directly (Leland *et al.*, 2004).

The piezoelectric generator produces output voltages ranging from 0 - 80V$_{p-p}$ whereas the WSM requires a stable DC input of 2.2 - 3.6V. The generator also does not produce sufficient power to operate the WSM directly. A circuit is therefore required to fulfill two purposes namely: output a steady usable DC voltage and store sufficient energy to operate the WSM for the duration of at least one transmission.

The schematic circuit in Figure 6.3 rectifies and transforms the output signal of the piezoelectric generator into a usable DC voltage.
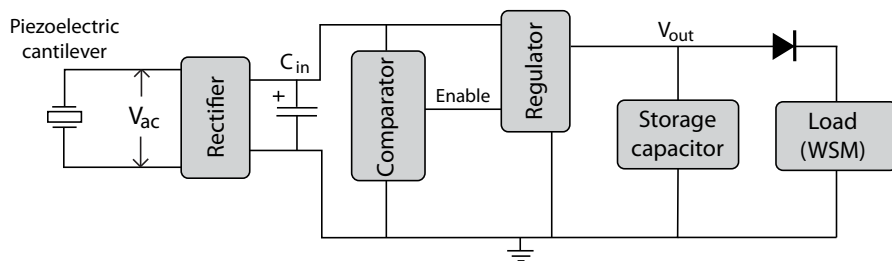
Figure 6.3: Power conditioning circuitry

The output signal of the generator was first rectified from where the energy was then stored in capacitor C_{in}. The WSM cannot be connected directly to C_{in} as the mote will continuously draw energy from the capacitor and not allow the piezoelectric generator to charge the capacitor to the required voltage. The MAX6433 comparator and a TPS76301 step-down low-dropout (LDO) voltage regulator form a buffer to allow C_{in} to charge. The regulator also produced the stable DC voltage needed to operate the WSM. The performance of the VEH subsystem is influenced by the size of C_{in} and not the storage capacitor. The

storage capacitor detailed in Figure 6.3 is simply the output capacitor of the regulator stage since the amount of energy generated by the piezoelectric cantilever is much smaller compared to the solar panel.

With normal operation the piezoelectric generator feeds energy to C_{in} causing the voltage to rise across the capacitor. The MAX6433 is a dual-level user-adjustable monitoring comparator. The comparator only enables the regulator when the top threshold is reached, in this case 5V. This then allowed the C_{in} to charge up to 5V before energy was transferred through the regulator to the mote. The regulator outputs a user defined 4.2V permitting the mote one transmission cycle. Once the voltage of C_{in} dropped to the lower threshold of 4.3V, the comparator would shutdown the regulator and the piezoelectric generator could again charge C_{in}. The value of 4.2V was chosen to maximise the operating duration of the WSM by charging the capacitors to the maximum operating voltage.

The size of C_{in} is application specific and dependent on the energy needed for the duration of at least one transmission cycle of the WSM. This includes start-up, sensing, processing of gathered data and transmitting of data. One transmission period was 2.5s, as will be detailed in section 7.1. To calculate a sufficient capacitance size for C_{in}, a safe measure of 5s was defined for the transmission cycle duration. With the TelosB WSM having an average power consumption (P_{avg}) of 425μW as assumed in section 6.4, the energy required (E_{req}) to sustain the WSM for the period Δt of 5s is given by equation 3.3:

$$
\begin{aligned}
P_{avg} &= (425 \times 10^{-6}) = \frac{E_{req}}{\Delta t} \\
E_{req} &= (425 \times 10^{-6}) \times 5 \\
&= 2.13\text{mJ}
\end{aligned}
$$

The energy required to sustain the WSM for 5s was 2.13mJ. Calculating the capacitance of C_{in} was achieved by reworking equation 3.8:

$$
\begin{aligned}
E_{DEC} &= \tfrac{1}{2}C_{in}\left[(V_{WV})^2 - (V_{MIN})^2\right] \\
C_{in} &= \frac{2(E_{DEC})}{[(V_{WV})^2-(V_{MIN})^2]} = \frac{2(2.13\times10^{-3})}{(5^2-4.3^2)} \\
&= 654\mu\text{F}
\end{aligned}
$$

Therefore, C_{in} required a minimum capacitance of 654μF to sustain the 5s transmission period. C_{in} was chosen as two 470μF capacitors in parallel producing a total capacitance of 940μF. Increasing the capacitance further proved trivial for the particular application program, as C_{in} only demanded a longer charging period between transmissions. As mentioned in section 6.3, diodes were connected from each energy harvesting stage to the load. The voltage drop across the diodes not only prevented the storage capacitors charging each other but also limited the supply voltage of the TelosB mote to a maximum of 3.5V.

The VEH subsystem was designed using the following design sequence:

- Define the characteristics of the source vibrations. What is the average magnitude and frequency? Is the frequency and magnitude consistent over time?

- Define the characteristics of the load (in this case the TelosB wireless sensor mote) by determining parameters such as the operating voltage window, standby current, transmit and receive current, average and peak power dissipation, minimum required duty-cycle for mote operation.

- Choose a suitable piezoelectric cantilever in order to get an acceptable operating voltage range as input to the DC-DC converter.

- Estimate the output power potential generated by the piezoelectric cantilever from the vibrations using the generic power expression given in equation (4.8). Does it produce sufficient output power needed for the load?

- Is the selected piezoelectric cantilever feasible in terms of physical size, mass, and cost? Is vibration conversion still a feasible option? If so, proceed?

- Choose or design a suitable voltage regulator or DC-DC converter that will efficiently regulate the rectified voltage for the particular application.

- Choose C_{in} based on load constraints. Such constraints include volume, cost, maximum power consumption and maximum acceptable voltage drop during transmission state.

- Optimise resulting design with the chosen value of C_{in} to evaluate if sufficient power is generated.

A detailed schematic diagram of the VEH subsystem is included in Appendix A.

6.6 Solar Energy Harvesting (SEH) subsystem

In popular past designs the solar panel was either connected directly to the battery and supercapacitor or utilised a diode between the solar panel and storage medium. This however introduced two major disadvantages. First, the operating efficiency of the solar panel was significantly degraded if the solar panel was directly connected to the storage medium. This was due to the mismatch caused by the solar panel's output voltage being forced to that of the supercapacitor or battery's instantaneous voltage. Even with a diode in-between, the voltage of the solar panel deviated considerably from its maximum power point and resulted in inefficient energy harvesting.

Secondly, the system was unable to harvest energy when the solar panel's voltage was below that of the storage medium. This situation often occurred in low light intensities and it

was therefore crucial that the system was capable of harvesting any energy in such conditions. A step-up voltage buffer was needed to prevent degraded operating efficiency and to harvest energy even when the output voltage of the solar panel was below the voltage of the storage capacitor. A PWM switching regulator with an enable function could be used as a buffer between the ambient power source and storage medium. This served the dual purpose of boosting the output voltage and blocking the reverse current flow from the supercapacitors to the solar panel without the overhead of 0.7V from a typical diode.
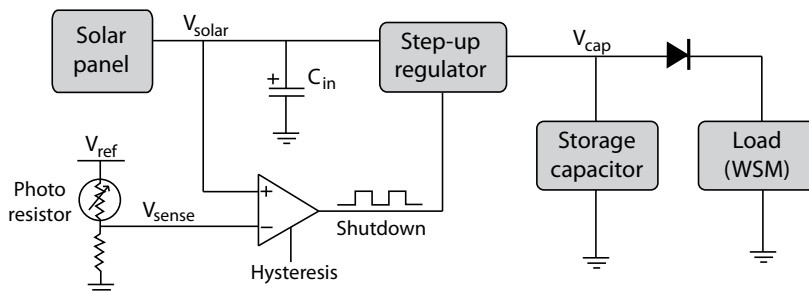
Figure 6.4: SEH subsystem components.

Fig 6.4 shows the major components of the SEH subsystem. A form of maximum power point tracking (MPPT) needs to be implemented in addition to harvest maximum energy from the solar panel at all times. A PWM switching regulator alone is not capable of MPPT and therefore would not efficiently harvest the available energy. However, a switching regulator with a comparator and a sensing device can be used to perform voltage fraction MPPT.

6.6.1 SEH subsystem components

The SEH subsystem circuit consists of three primary components: a solar cell, a component to manipulate the voltage (voltage regulator) and an energy storage reservoir. There are two common types of energy reservoirs for solar power circuits namely: rechargeable batteries and capacitors.

Rechargeable batteries have the advantage of a higher energy density than that of capacitors and also having a more stable output voltage. The disadvantage is that they have a limited operating life of about two to five years depending on charge cycles. Batteries also operate more effectively under controlled charge profiles and therefore need additional charging circuitry. However, capacitors have an almost limitless operating life and do not require any special charging. A stable output voltage from capacitors can also be generated by using a large capacitor of several farad and by positioning the energy reservoir at the output of the voltage regulator. Since one of the objectives of this project was to extend the operating life of the wireless sensor mote, a sensible choice would be opting for a capacitor as the energy reservoir.

A second decision is that of the choice of voltage regulator. Previous designs (Roundy,

2003) implemented linear low-dropout (LDO) voltage regulators, such as the TPS72501 from Texas Instruments (2009). The benefit of linear LDO regulators is that they are small, simple to use and require few external components. The output voltage of these regulators is controlled by monitoring the effective resistance of a pass transistor as power is dissipated by it. Their efficiencies depend on the input to output voltage ratio but are typically lower than DC-DC switching regulators. Unlike linear regulators, the output voltage of switching regulators are determined by incorporating a fast on and off switching of a shunt element between the input and the output. The average value of the output is controlled by the duty-cycle of the switching frequency and normally smoothed by an inductor. With this switching principle, DC-DC switching regulators demonstrate a higher operating efficiency than linear regulators. The disadvantage being that they are more complex and often require more external components.

However, since the efficiency was of higher importance, the MAX1676 DC-DC switching regulator from Maxim Integrated Products (2009) was selected for the SEH subsystem circuit. A simplified version of the SEH circuit highlighting the fundamental components is shown in Figure 6.5.
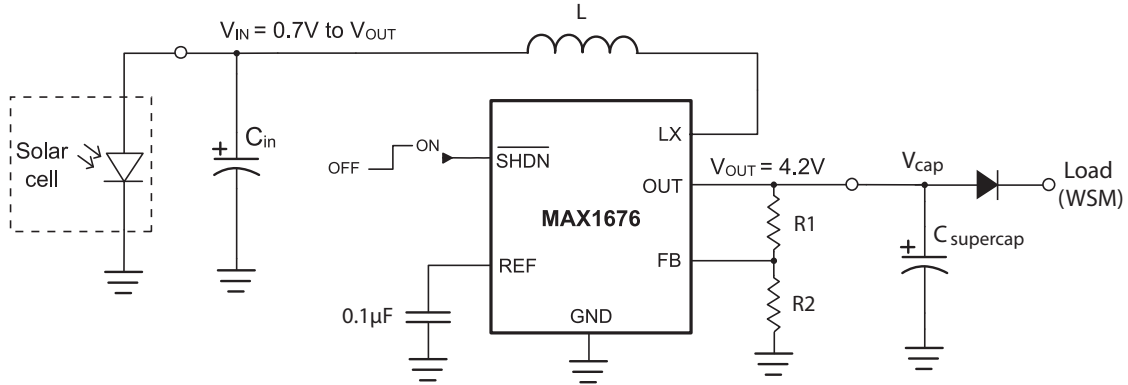
Figure 6.5: SEH subsystem circuit

The Maximum Power Point (MPP) circuitry is not included in Figure 6.5 to simplify explanation. The solar cell directly charges the small input capacitor, typically $1\mu F$. Depending on the status of the shutdown pin ($\overline{SHDN}$), determined by the MPP circuitry, the DC-DC converter will convert the voltage to the output voltage. The output voltage, 4.2V in this case, was determined by the ratio of resistors R1 and R2. An input from as little as 0.7V can be boosted to the output voltage while maintaining a fairly high efficiency. The output voltage is predetermined by adjusting the resistive ratio on pin FB. The output voltage of the DC-DC converter was set to 4.2V for two reasons; the 70F storage supercapacitors have a maximum voltage of 2.1V each, but due to their series connection, this allows for a maximum of 4.2V. Secondly, the storage capacitor of the solar subsystem circuit is part of the Storage Capacitor Array (SCA) as explained earlier. A diode at the output of the SEH subsystem is therefore needed to eliminate the supercapacitors charging other subsystem capacitors in the SCA and only supply energy to the load. The voltage drop across the diode reduces the output voltage to about 3.5V, which closely resembles the maximum operating voltage of the

WSM.

6.6.2   Maximum Power Point Tracking (MPPT) circuitry

MPPT can be achieved if a comparator controls the operation of the DC-DC switching regulator, by comparing a scaled version of the solar voltage (V_{solar}) and the output voltage of a sensing device (V_{sense}). A maximum power window is created, shown in Figure 6.6(a), by setting a predetermined hysteresis band (V_{HB}) with the comparator.
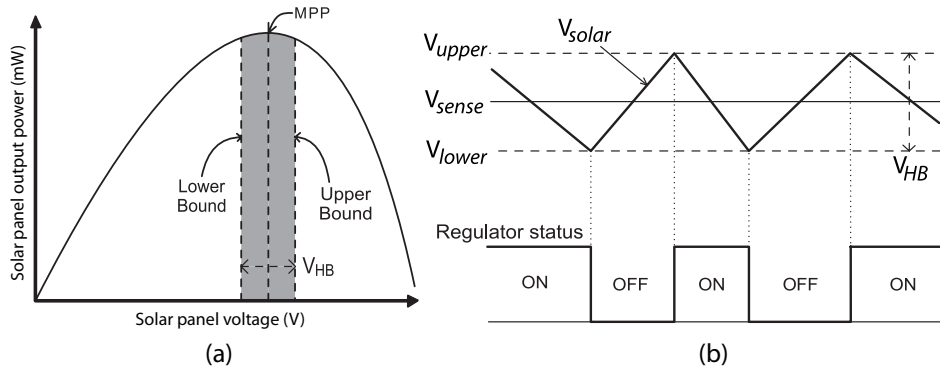
Figure 6.6: Solar panel maximum power window redrawn and adapted from Park & Chou (2006)

As V_{solar} reaches V_{upper}, the comparator turned the switching regulator on. By charging the storage capacitor, V_{solar} dropped until reaching V_{lower} where the comparator turned off the switching regulator and V_{solar} again started increasing, as detailed in Figure 6.6(b). With the regulator being constantly enabled and disabled, the output voltage oscillated around the MPP. Reducing the hysteresis band, the oscillation of the output voltage decreased and tracked the maximum power point more accurately. This averaged V_{solar} at the MPP and charged the small input capacitor (C_{in}) accordingly.

Previously proposed designs such as Simjee & Chou (2006), implemented MPP algorithms using microcontrollers that could possibly track the MPP more accurately but did not allow autonomous operation if the microcontroller went into a low-power sleep state. With the proposed analogue configuration the harvesting system can separately monitor and track the solar power with a sensing device. A photo resistor (VTB8440B) was implemented as the sensing device. Although some photo resistors feature higher linearity with respect to light intensity they are typically much more expensive. The VTB8440B proved to be an inexpensive solution with relative linearity to V_{solar} and V_{MPP}. Linearity was particularly evaluated for low outdoor light intensities (100 - 10,000 lux), since high levels of solar radiation produced sufficient energy even when the photo resistor's linearity deviated slightly. Fig. 6.7 shows the linearity between the photo sensor's resistive output, open-circuit voltage (V_{OC}) of the panel and V_{MPP} for light conditions between very dark overcast days (100 lux) and full

daylight (10,000 lux).
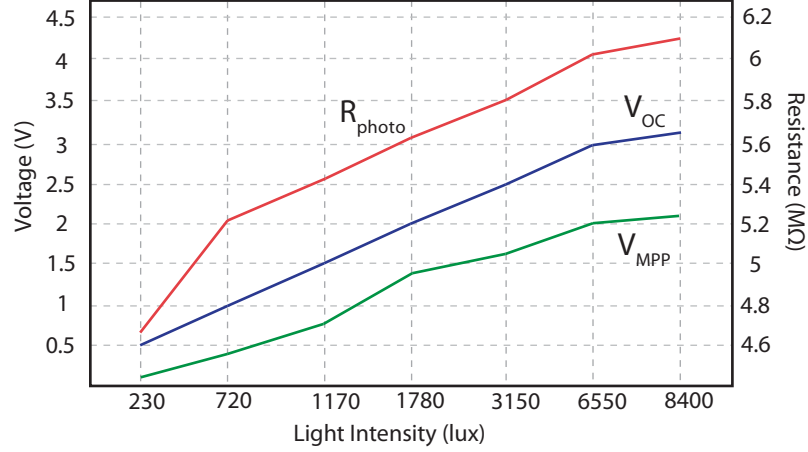
Figure 6.7: Linearity of sensor output and MPP

This linearity enabled V_{sense} to proportionally track the MPP of the solar panel. By constructing a simple high impedance voltage divider circuit, a variable voltage output (V_{sense}) can be obtained proportional to the MPP voltage of the solar panel. If V_{solar} is now also scaled accordingly, it can be fed into a comparator to control the on/off status of the regulator.

Different sized supercapacitors were implemented in series as the storage reservoir for the SEH subsystem. This configuration was necessary as each supercapacitor had a maximum voltage rating of 2.5V. The series connection had an additional benefit by reducing the average self-discharge rate of the 70F supercapacitor combination to 165μJ/s. The self-discharge rate was experimentally calculated by measuring the open circuit voltage across the supercapacitor over a 72 hour period. First the decrease in energy was calculated using equation (3.8):

$$E_{DEC} = \tfrac{1}{2}C\left[(V_{WV})^2 - (V_{MIN})^2\right] = \tfrac{1}{2}(35)(2.5^2 - 1.95^2)$$
$$= 42.83\text{J}$$

where: $C = 35$F, the working voltage $V_{WV} = 2.5$V and $V_{MIN} = 1.95$V.

From this the average self-discharge rate was determined over a 48 hour period with equation (3.3):

$$P_{avg} = \frac{E}{\Delta t} = \frac{42.83}{259200}$$
$$= 165\mu\text{J/s}$$

where: $E = 42.83$J and $\Delta t = (60\text{x}60\text{x}72)$s.

A detailed schematic diagram of the SEH subsystem is included in Appendix A.

6.7   Component selection

The respective resistor calculations for the prototype design are included in Appendix B. Additionally, a complete list of components implemented in the hybrid energy harvesting power management system is included in Appendix C.

6.8   Summary

This chapter presented an overview of the energy harvesting power management system. The configurations and characteristics of the system such as the modular architecture that allowed integration of additional energy harvesting sources were highlighted. Design choices and layout of the hybrid energy harvesting prototype were discussed. The power conditioning circuitry of both the VEH and SEH subsystems were explained respectively. With these principles of operation introduced, the performance of the prototype were evaluated as described in chapter 7.

Chapter 7

Prototype Evaluation

The proposed energy harvesting system was evaluated first as individual subsystems and then as a hybrid energy harvesting system. The performance of both the VEH and SEH subsystems were evaluated through their respective experimental setups discussed in sections 7.2 and 7.3.

The physical implementation of the hybrid energy harvesting circuit is shown in Figure 7.1 highlighting the VEH and SEH subsystems as well as featuring the main components and input and output interfaces. The energy harvesting PCB layout and a detailed CAD diagram of the prototype PCB fitted on the TelosB WSM are included in Appendix D and Appendix E.
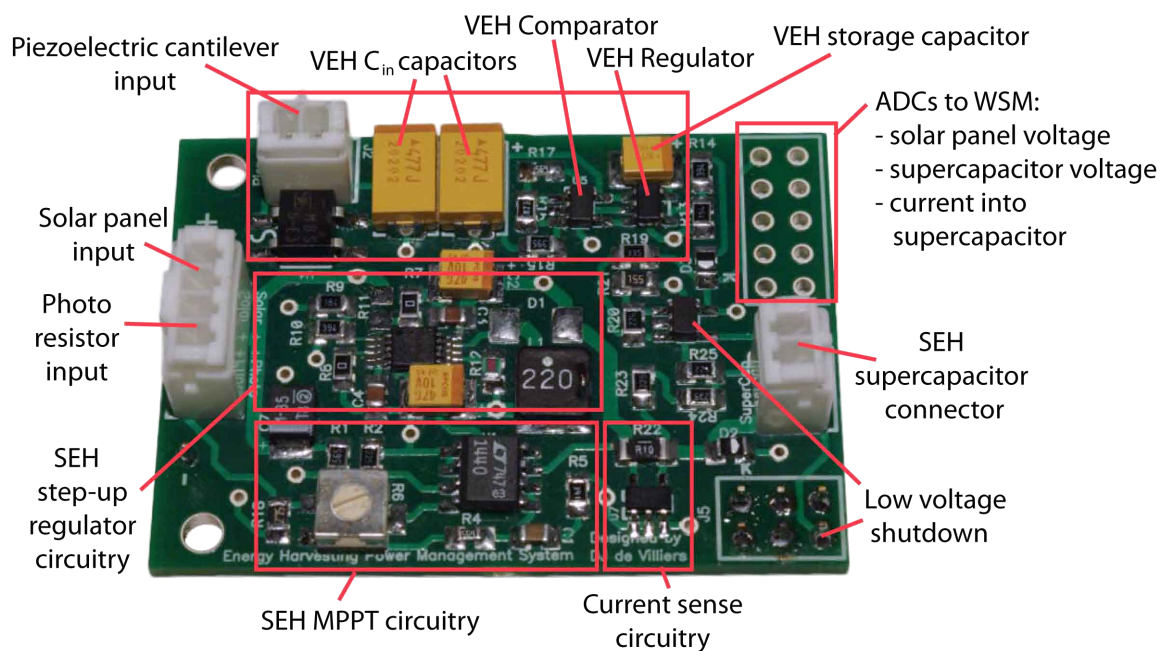
Figure 7.1: Hybrid energy harvesting power management PCB prototype

7.1 Load evaluation

The load is directly dependent on the application program operating on the WSM. Details on the application program are included in Appendix F. For experimental purposes the program took 10 measurements with a measurement period of 250ms. The collected values of the measurements were then transmitted every 2.5 seconds. This process was repeated as long as the program functioned.

The power consumption, as detailed in Figure 7.2, of the application program was evaluated by measuring the voltage across a 100Ω resistor connected in series between the power supply and the WSM. The graph revealed transmission peaks of around 33mW with a period of 10ms (t_a) and a transmission repeat interval of 2.5s. Ten measurements with a power consumption of 64μW per measurement and period of 40ms (t_b) were done at a measurement repeat interval of 250ms between transmissions. The power consumption of the transceiver start-up was evident prior to each transmission as indicated by *radio start-up* in Figure 7.2.
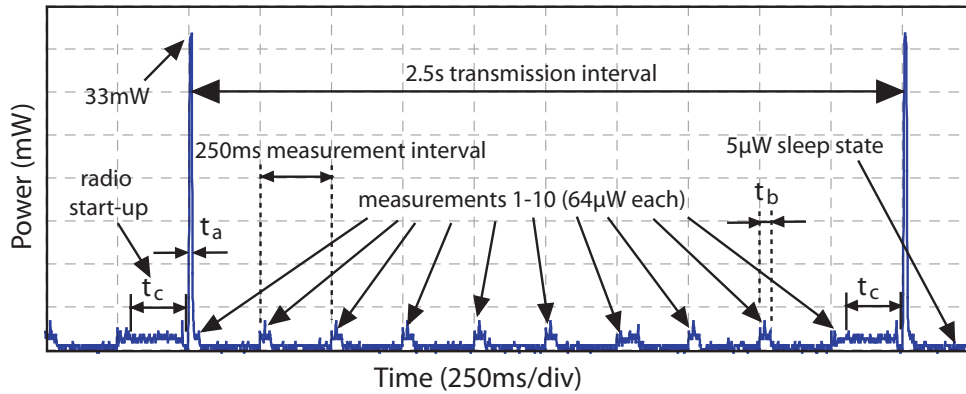
Figure 7.2: Power consumption of application program

Details of the type of measurements taken by the WSM is described in Table 7.1.

Table 7.1: Mote application measurements

Measurement no.	Peripheral
1 - 3	Internal voltage
4	ADC2 (V_{solar})
5	ADC1 (Current sensor)
6	ADC0 (V_{cap})
7	Relative humidity
8	Photosynthetic light
9	Total solar radiation
10	Temperature

The average power consumption of the mote was calculated using equation (7.1) and resulted in 150μW with the particular application program operating. It was assumed that t_b was constant for all measurements.

$$P_{avg} \times \Delta t = (P_{TX} \times t_a) + (P_m \times t_b \times n) + (P_{radiostart-up} \times t_c) + (P_{sleep} \times t_d) \qquad (7.1)$$

where: P_{TX} = transmit power (W)

t_a = active transmission period (s)

P_m = power consumption per measurement

t_b = measurement period (s)

n = number of measurements

$P_{radiostart-up}$ = power consumption of radio start-up (W)

t_c = radio start-up period (s)

P_{sleep} = average sleep power consumption (W)

t_d = total duration of sleep state per period (s)

$\Delta t = t_a + t_b + t_c + t_d$ (s) = repeat period (s)

$$
\begin{aligned}
P_{avg} \times (2.5) &= (33 \times 10^{-3})(10 \times 10^{-3}) + (64 \times 10^{-6})(40 \times 10^{-3})(10) + \\
& \quad (64 \times 10^{-6})(162 \times 10^{-3}) + (5 \times 10^{-6})(1.928) \\
&= 375.6 \mu J \\
P_{avg} &= 150 \mu W
\end{aligned}
$$

The estimated duty-cycle of the application program is the percentage ratio of $t_a/\Delta t$ and equals 0.4%. In section 6.4, an estimated average consumed power for a TelosB WSM with a 1% duty-cycle was given as $425\mu W$. If the duty-cycle of the application program would be increased to 1%, the measured power consumption (P_{avg}) would then be $375\mu W$ and would correlate closely with the 1% duty-cycle assumption made in section 6.4.

7.2   VEH subsystem

For experimental results, the piezoelectric generator was driven by the reference vibration of 10m/s^2 at 100Hz as discussed in section 4.6. The WSM was attached to the VEH circuit running the program from section 7.1. The experimental setup is shown in Figure 7.3.

Figure 7.4 displays the confirmation of actual transmitted data received by a nearby base station receive sensor mote connected to a PC. The transmit WSM was powered solely by the piezoelectric generator with no additional battery. The VEH circuitry effectively converted the energy harvested by the piezoelectric generator into usable energy to power the WSM. In addition, Figure 7.4 highlights received parameters such as ADC voltages, light, humidity and temperature.

The operation of the VEH circuit is shown in Figure 7.5: The top trace illustrates the charging and discharging of C_{in} with upper and lower thresholds of 5V and 4.3V respectively.
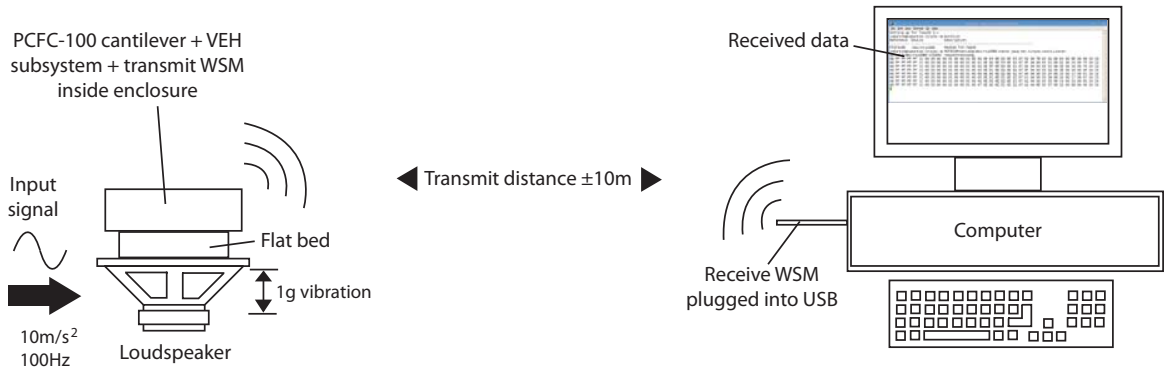
Figure 7.3: Experimental setup for confirmation of transmitted data
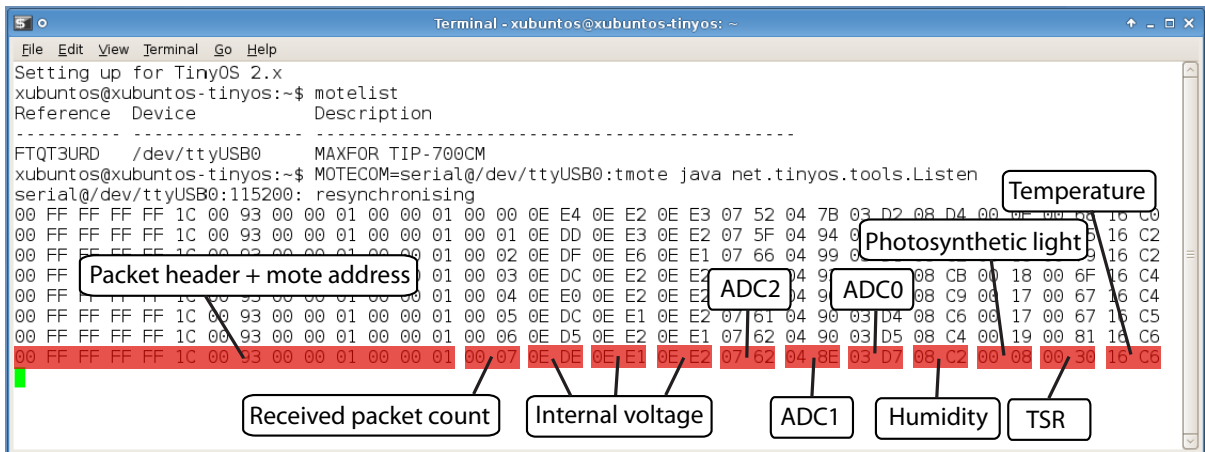
Figure 7.4: Verification of transmitted data

The bottom trace reveals the output voltage of the VEH circuit (V_{out}) with the mote connected. As mentioned in section 6.5, the storage capacitor of the VEH circuit is the output capacitor of the regulator due to the small output power of the piezoelectric cantilever. As C_{in} discharges, the circuit is capable of producing a 2.3s, 4.2V regulated pulse to supply the sensor mote. The duration of the pulse proved sufficient for one transmission consisting of ten measurements each. The same reference input signal enabled the circuit to repeat the regulated output pulse every 10.6 seconds.
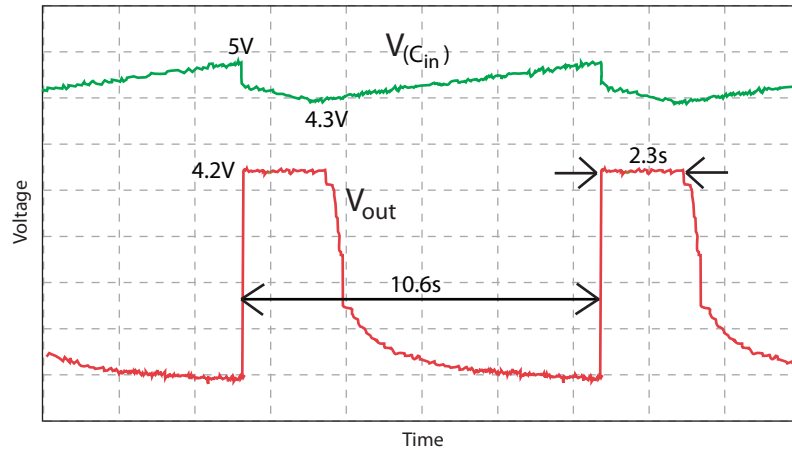
Figure 7.5: VEH circuit operation

A good agreement existed between the theoretical and measured power output of the piezoelectric cantilever into a resistive load. The theoretical power output, as detailed in section 4.6, was calculated to be 932μW. The actual measured power output, as calculated in section 4.7, was 897μW. However, the measured output power proved significantly lower for the capacitive load than for the resistive load, peaking at 368μW. According to Roundy (2003) even the best achievable power transfer is still lower for a capacitive load than for a resistive load even if the design is optimised for a capacitive load. Exactly how much lower is dependent on various parameters such as the output power of the piezoelectric generator, size of the capacitor C_{in} and the type of rectification implemented. Additionally, it is believed that the rectifying diodes together with the assumptions made in the generic vibration model further contribute to the discrepancies between the theoretical and measured power output.

The transfer of power through the VEH circuit is illustrated in Figure 7.6 highlighting the efficiency of the power conditioning circuitry.
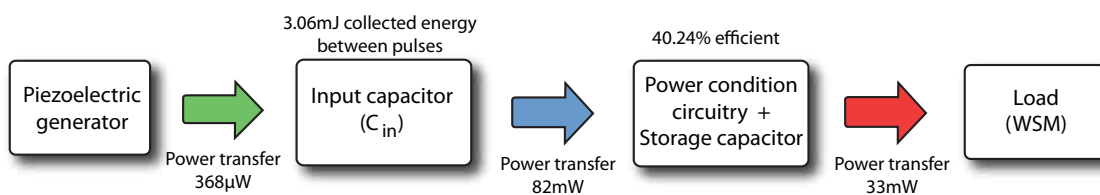
Figure 7.6: Power transfer in VEH subsystem

It took the piezoelectric generator 8.3s to charge $C_{in}(940\mu F)$ from 4.3V to 5V. The energy collected in C_{in} between pulses was calculated as 3.06mJ according to equation (3.8).

$$E = \tfrac{1}{2}C\left[(V_{MAX})^2 - (V_{MIN})^2\right] = \tfrac{1}{2}(940 \times 10^{-6})(5^2 - 4.3^2)$$
$$= 3.06\text{mJ}$$

From the charge duration of 8.3s the average power transfer from the piezoelectric generator to the storage capacitor C_{in} was calculated as $368.7\mu W$ using equation (3.3).

$$P_{avg} = \frac{E}{\Delta t} = \frac{3.06 \times 10^{-3}}{8.3}$$
$$= 368.7\mu W$$

This corresponded closely to the output power of $342.8\mu W$ into a capacitive load detailed in section 4.7. A rapid drop in voltage was evident in the top trace of Figure 7.5 when the regulator was enabled and the WSM transmitted the 10 measurements. C_{in} discharged from 5V to 4.6V in 22ms as the mote transmitted the data. Power transfer through the conditioning circuitry was calculated to be 82mW according to equations (3.8) and (3.3).

$$E = \tfrac{1}{2}C\left[(V_{MAX})^2 - (V_{MIN})^2\right] = \tfrac{1}{2}(940 \times 10^{-6})(5^2 - 4.6^2)$$
$$= 1.8\text{mJ}$$

$$P_{avg} = \frac{E}{\Delta t} = \frac{1.8 \times 10^{-3}}{22 \times 10^{-3}}$$
$$= 82\text{mW}$$

As previously mentioned, the power consumption of the WSM was found to be 33mW during transmission. The efficiency through the VEH conditioning circuitry can therefore be estimated by:

$$\text{Efficiency}(\eta) = \frac{P_{out}}{P_{in}}$$
$$= \frac{33 \times 10^{-3}}{82 \times 10^{-3}}$$
$$= 40.24\%$$

7.2.1 VEH subsystem performance

One approach to performance measurement of the VEH subsystem is by evaluating the maximum sustainable duty-cycle at respective frequencies and accelerations. This duty-cycle is a percentage value and refers to the ratio of total on- to off-time of the WSM. The performance measurement is important to assess how the VEH subsystem would operate if the input vibration source varied with respect to frequency and acceleration.

As verified in section 4.6, the piezoelectric generator is inherently a resonance structure. It is critical that the resonance frequency matches that of the input vibration. Figure 7.7(a) details the power output and Figure 7.7(b) the maximum sustainable duty-cycle at various vibration accelerations[1].

Figure 7.7: (a) Power output and (b) maximum duty-cycle vs acceleration

The output power and maximum sustainable duty-cycle were both calculated using the experimental setup discussed in section 4.6. For the graphs in Figure 7.7 the input vibration signal was kept at 100Hz and the acceleration magnitude was varied by altering the input voltage from the signal generator. The time to charge the input capacitor (C_{in}) from 0V to 5V was recorded at acceleration magnitudes ranging from 0.25g to 3g. As one example, the power output calculation for a 2g acceleration was calculated using equations (3.8) and (3.3):

$$E = \tfrac{1}{2}C\left[(V_{MAX})^2 - (V_{MIN})^2\right] = \tfrac{1}{2}(940 \times 10^{-6})(5^2)$$
$$= 11.75\text{mJ}$$

$$P_{avg} = \frac{E}{\Delta t} = \frac{11.75 \times 10^{-3}}{18.2}$$
$$= 645.6\mu\text{W}$$

where: $C_{in} = 940\mu\text{F}$, $V_{WV} = 5\text{V}$, $E = 11.75\text{mJ}$ and $\Delta t = 18.2\text{s}$.

The maximum sustainable duty-cycle at different accelerations is derived from reworking equation (6.2) into (7.2).

---

[1] In section 7.2.1 the symbol g denotes gravitational acceleration and not the SI symbol for mass.

$$\bar{P}_g \geq (1 - D)P_{sleep} + D.P_{active}$$

$$D_{max} = \frac{P_{avg} - P_{sleep}}{P_{active} - P_{sleep}} \% \qquad (7.2)$$

where: $P_{avg} = \bar{P}_g$

As one example, the maximum sustainable duty-cycle for a 2g acceleration is calculated using equation (7.2):

$$D_{max} = \frac{(645.6 \times 10^{-6}) - (5 \times 10^{-6})}{33 \times 10^{-3} - (5 \times 10^{-6})} \times 100$$
$$= 1.94\%$$

where: $P_{avg} = 645.6\mu W$, $P_{sleep} = 5\mu W$ and $P_{active} = 33mW$.

Figure 7.8(a) details the output power and Figure 7.8(b) the maximum sustainable duty-cycle at frequencies between 80Hz and 120Hz. The importance of matching the generator resonance frequency to the frequency of the input vibration is clearly visible.
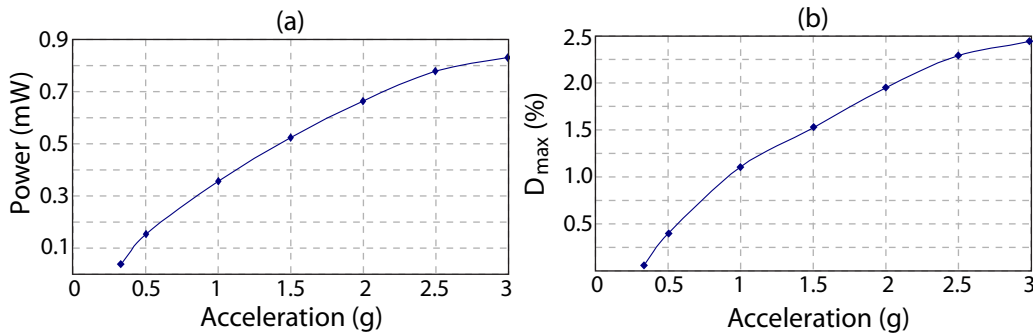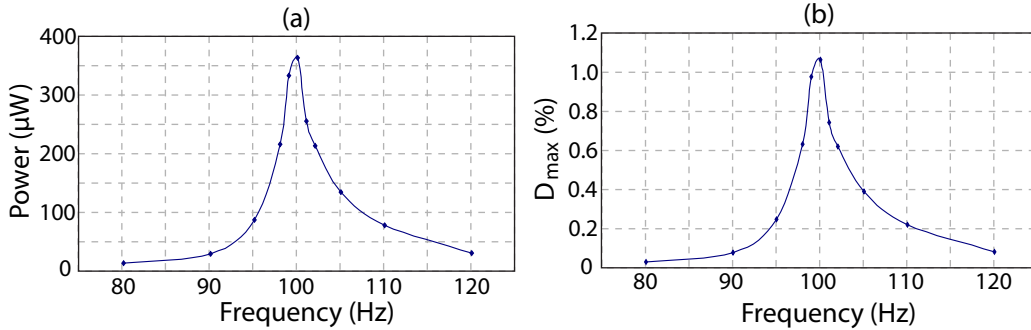

Figure 7.8: (a) Power output and (b) maximum duty-cycle vs frequency

The output power and maximum sustainable duty-cycle were both calculated using the experimental setup discussed in section 4.6. For the graphs in Figure 7.8 the input vibration signal was kept at an acceleration magnitude of 1g ($10m/s^2$) and the frequency was varied by altering the input frequency from the signal generator. The time to charge the input capacitor (C_{in}) from 0V to 5V was recorded at frequencies ranging from 80Hz to 120Hz. As one example, the power output at 110Hz was calculated using equation (3.3):

$$P_{avg} = \frac{E}{\Delta t} = \frac{11.75 \times 10^{-3}}{168}$$
$$= 69.94\mu W$$

where: $E = 11.75$mJ and $\Delta t = 168$s.

Using equation (7.2), the maximum sustainable duty-cycle at different frequencies was obtained. As one example, the maximum sustainable duty-cycle calculation for a 1g acceleration at 110Hz is calculated using equation (7.2):

$$D_{max} = \frac{(69.94 \times 10^{-6}) - (5 \times 10^{-6})}{33 \times 10^{-3}} \times 100$$
$$= 0.2\%$$

where: $P_{avg} = 69.94\mu$W, $P_{sleep} = 5\mu$W and $P_{active} = 33$mW.

Due to the operating characteristics of the VEH circuit, no power can be supplied to the WSM between the regulated output pulses. The mote would therefore draw power from the SEH circuit between the pulses for sustained operation.

7.3   SEH subsystem

The SEH circuitry was enclosed in a box with an ingress protection (IP) rating of 66. IP ratings are developed by the European Committee for Electro Technical Standardisation (CENELEC) specifying the environmental protection the enclosure provides (CENELEC, 2009). The first digit describes the level of protection from solid objects and the second digit the level of protection from liquids. With an IP66 rating, the enclosure is fully protected against dust and temporary flooding of water. The IP66 rating was necessary since the experiment was conducted outside so as to protect the WSM and power management circuitry against environmental elements such as wind and rain.

The enclosure was mounted outside on a wall as shown in Figure 7.9. The WSM was programmed to take 10 measurements and transmit the values back to a base station receive mote every 2.5 seconds. The same application program described in section 7.1 and Table 7.1 operated on the WSM. The base station receive mote was connected to a PC inside an office in the administration building of the Cape Peninsula University of Technology (CPUT, 2008). The experimental setup is shown in Figure 7.10.

Due to the ADC configuration on the mote, the measured voltage for both the WSM supply voltage (V_{WSM}) and the SEH supercapacitor voltage (V_{cap}) were originally constrained to an upper limit of 3V by the regulator due to the internal 1.5V reference. However, the supercapacitors could be charged to 4.2V. This posed a problem as no information on V_{WSM} and V_{cap} was available above 3V. The program was modified to enable one of the external ADCs into which a scaled version of V_{cap} was fed.

Figure 7.9: Solar experiment
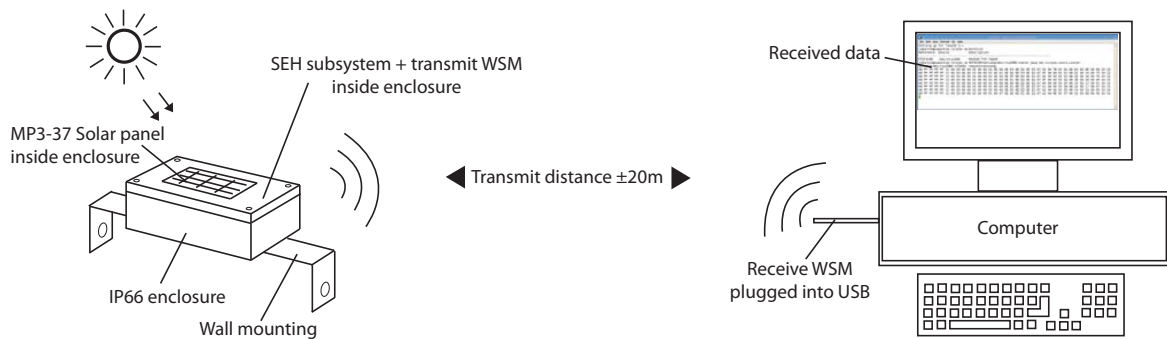
Figure 7.10: Experimental setup for SEH subsystem evaluation

Calculations reveal that the WSM, with this particular program, together with the power management circuitry and self-discharge of the supercapacitors consumed an average of 583μJ/s. This can be validated by referring to Figure 7.13(b). The discharge of the supercapacitors are clearly evident in the time frame 00:00 to 06:00. Due to the time, the SEH subsystem is harvesting no energy from the solar panel. The WSM and power management circuitry are operating exclusively from the supercapacitors. The decrease in energy can be calculated from equation (3.8) over the period of 6 hours:

$$E_{DEC} = \tfrac{1}{2}C\left[(V_{WV})^2 - (V_{MIN})^2\right] = \tfrac{1}{2}(35)(2.9375^2 - 2.8125^2)$$
$$= 12.6\text{J}$$

where: $C = 35$F, the working voltage $V_{WV} = 2.9375$V(at 00:00) and $V_{MIN} = 2.8125$V (at 06:00).

From the decrease in energy in the time frame 00:00 to 06:00, the average power consumption can be calculated from equation (3.3):

$$P_{avg} = \frac{E}{\Delta t} = \frac{12.6}{21600}$$
$$= 583\mu\text{W}$$

where: $E = 12.6$J and $\Delta t = (60\text{x}60\text{x}6)$s.

At an average power consumption of 583μW, the 35F supercapacitor combination is capable of sustaining the WSM and power management circuitry for almost 4 days without any sunlight if fully charged to 4.2V. Due to the diode configuration explained in section 6.3, the supply voltage across the WSM was 0.7V lower than the voltage across the supercapacitors. The minimum operating voltage of the WSM is 1.8V. Therefore, the supercapacitors can effectively power the WSM with a voltage down to 2.5V. Theoretically, the 4 day sustainability can be supported by calculating the hold-up time of the supercapacitors from 4.2V down to 2.5V at a power consumption of 583μW. First the decrease in energy is calculated using equation (3.8):

$$E_{DEC} = \tfrac{1}{2}C\left[(V_{WV})^2 - (V_{MIN})^2\right] = \tfrac{1}{2}(35)(4.2^2 - 2.5^2)$$
$$= 199\text{J}$$

where: $C = 35$F, the working voltage $V_{WV} = 4.2$V and $V_{MIN} = 2.5$V.

Reworking equation (3.3) and substituting the values yields:

$$\Delta t = \frac{E}{P_{avg}}$$
$$= \frac{199}{583 \times 10^{-6}}$$
$$= 341\ 337.9\text{s} = 3.95 \text{ days}$$

Experimental data collected over a period of 3 months are shown in Figure 7.11 where (a) shows temperature, (b) supercapacitor voltage (V_{cap}), (c) current into supercapacitor and (d) solar panel voltage (V_{solar}) over time. As confirmation of actual data transmission, all the data were sampled and transmitted by the WSM itself as detailed by the experimental setup shown in Figure 7.10.

In an effort to analyse the data, the first week in Figure 7.11 is data shown enlarged in Figure 7.12, highlighting the same parameters. Figure 7.12(a) reveals the temperature captured over the period of one week. The seven days are clearly evident as the temperature rises from a minimum night temperature to a midday maximum. On average the temperature altered between 10°C and 45°C.

Figure 7.12(b) shows the daily charging of the SEH supercapacitors. On average the voltage across the supercapacitors seldomly dropped below 2.75V. Figure 7.12(c) displays the current into the supercapacitors during charging. This corresponded well with the increase in voltage in Figure 7.12(b) as the supercapacitors charged. Higher values of current were observed on the forth day. Referring back to Figure 7.12(a), revealed a drop in temperature during the forth day. This supports the temperature characteristics statement of solar cells made in section 5.5.1 that the output power of solar cells increase with a corresponding drop in ambient temperature. Figure 7.12(d) shows the solar panel voltage captured over the period of one week. Much like the temperature values, the days were clearly visible as the voltage increased from a minimum at night to around 3.6V during each day.

It was at first believed that the drop in temperature on the forth day was due to overcast conditions. However, although the temperature dropped and the current into the supercapacitors increased, the voltage across the solar panel remained the same compared to the other days of the week. The conclusion was made that although not overcast, wind contributed to the decrease in ambient temperature. Checking the weather history for that day also confirmed that it was a clear sunny day with moderate wind present (Windguru, 2009).

For further analysis, the same parameters described in Figures 7.11 and 7.12 are shown over a 24 hour period in Figure 7.13. From Figure 7.13(b) a corresponding voltage increase is visible correlating with the current into the supercapacitors in Figure 7.13(c). It should be noted that the temperature readings in Figures 7.11, 7.12 and 7.13 were taken inside the sealed enclosure and therefore did not reflect the true outside ambient temperature. This however did not affect the performance of the SEH subsystem.
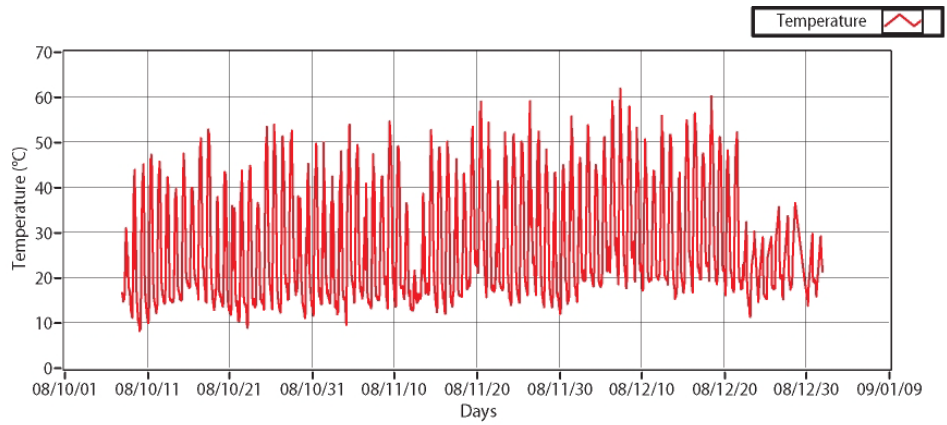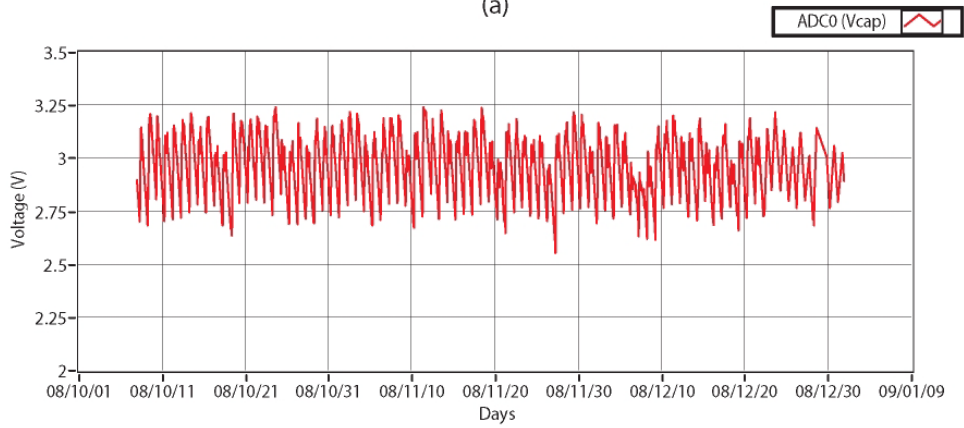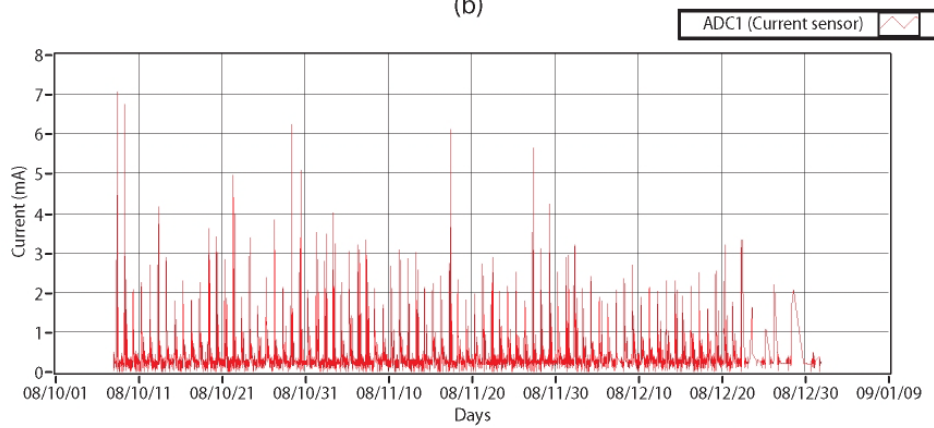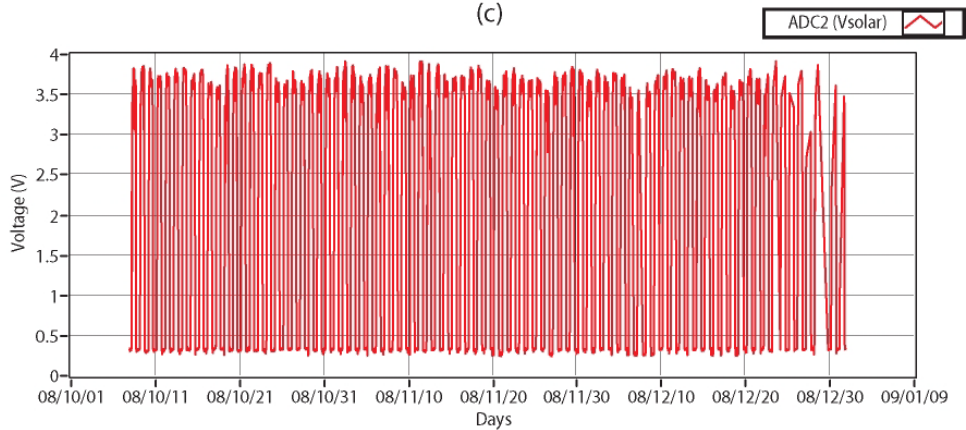
Figure 7.11: Data collected over a 3 month period
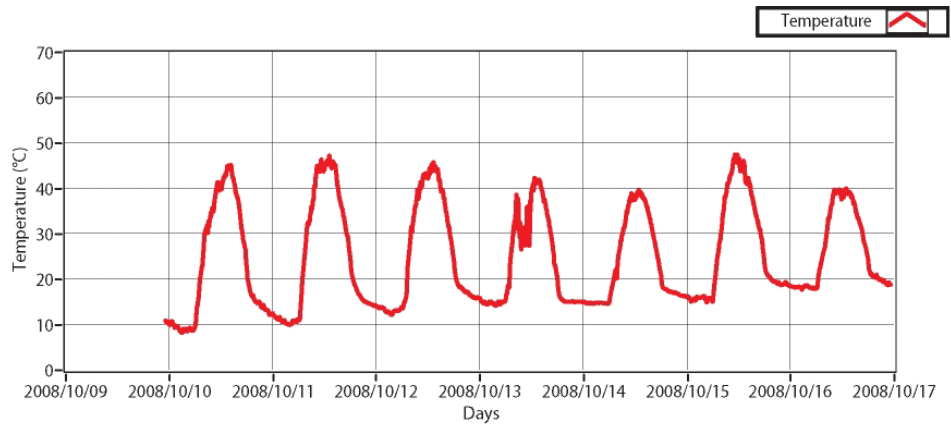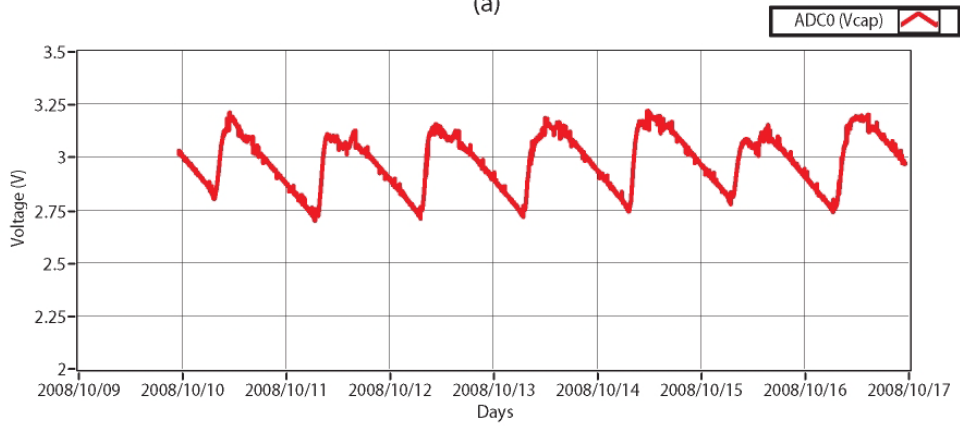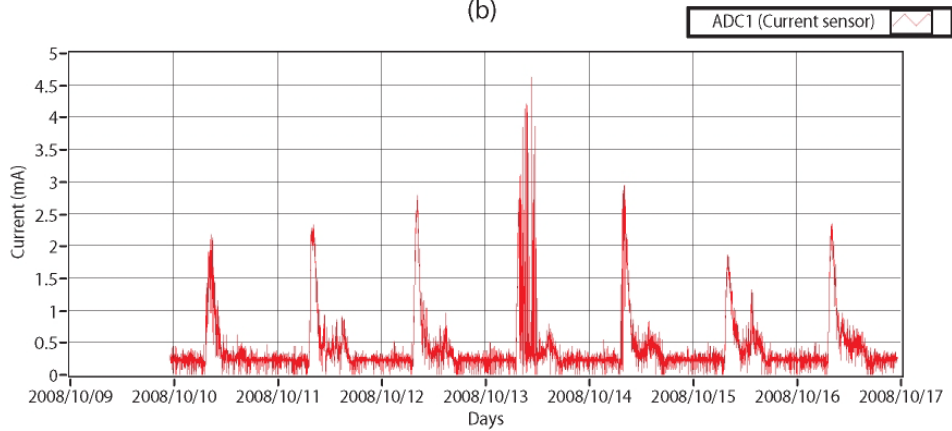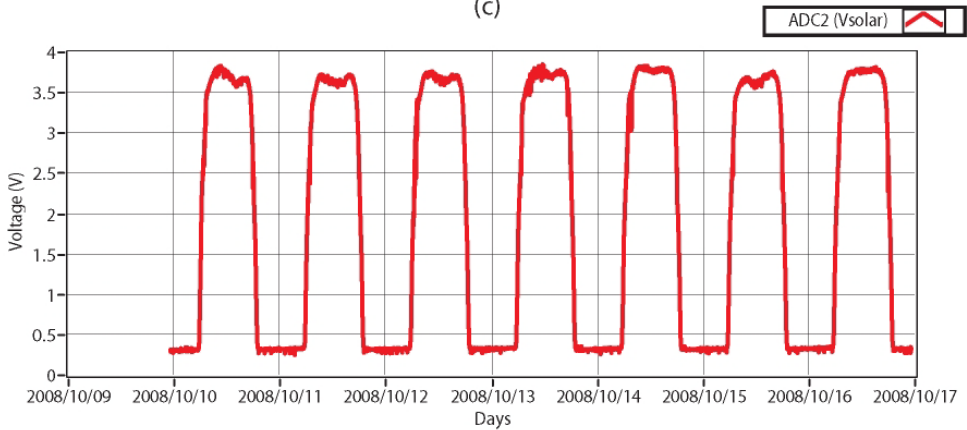
Figure 7.12: Data collected over a period of one week

The capacitance size of the supercapacitors determined the rate of charge. Although larger supercapacitors enabled longer sustained operation without sunlight, smaller supercapacitors charged more effectively in consecutive low lighting conditions. The size of the supercapacitors is therefore application driven. In the case of the present application, the series combination of two 70F supercapacitors proved sufficient for sustainable operation.

Since the proposed design featured no batteries, it was difficult to compare the performance to that of a system using a battery. As stated in section 3.2, the terms energy density and power density are used to compare capacities and performance of different systems.

According to Maxwell Technologies (2009), the maximum energy density (E_{max}) and maximum power density (P_{max}) for a supercapacitor are given by equations (7.3) and (7.4) respectively.

$$E_{max} = \frac{\frac{1}{2}CV^2}{3600 \times mass} \qquad Wh/kg \qquad (7.3)$$

$$P_{max} = \frac{V^2}{4 \times R \times mass} \qquad W/kg \qquad (7.4)$$

where C is the capacitance (farad), V the maximum applied voltage, the mass (kg) of the capacitor, R the equivalent series resistance (ESR) at 1 kHz and 1Wh = 3600J. For the series connection of two 70F supercapacitors, with a maximum applied voltage of 4.2V and combined mass of 32g, equation (7.3) for maximum energy density yielded:

$$E_{max} = \frac{\frac{1}{2}(35)(4.2)^2}{3600 \times 0.032}$$
$$= 2.68\text{Wh/kg}$$

The series supercapacitor combination had an ESR of 0.044Ω at 1kHz. Using equation (7.4), the maximum power density could be calculated.

$$P_{max} = \frac{(4.2)^2}{4 \times 0.044 \times 0.032}$$
$$= 3132\text{W/kg}$$

Although the energy density is typically one order of magnitude larger for rechargeable batteries in comparison with supercapacitors, the decision to incorporate a battery purely on higher energy density may not always be beneficial for long term performance and sustainability as discussed in chapter 3.
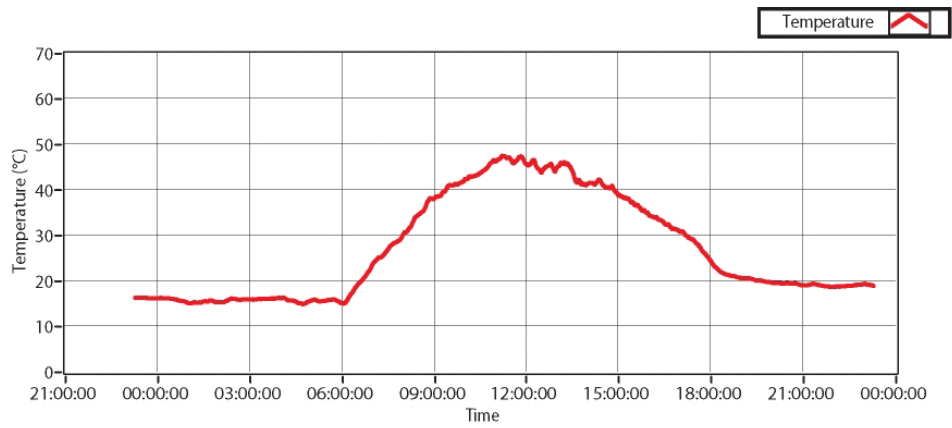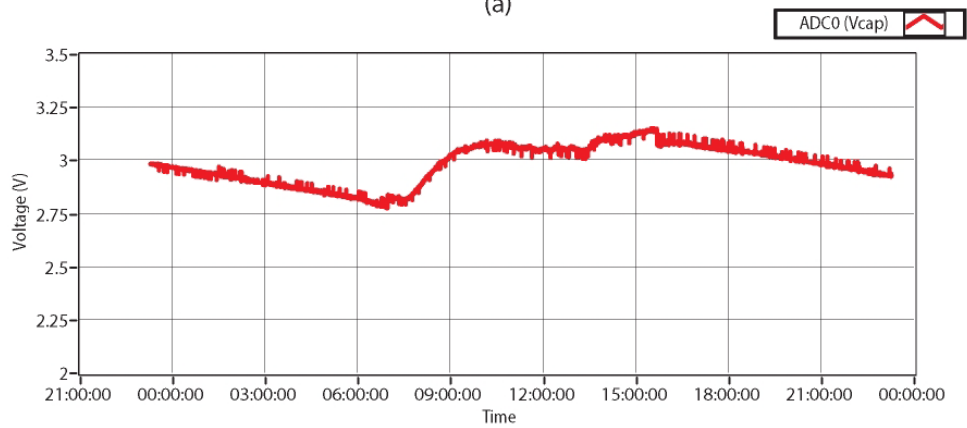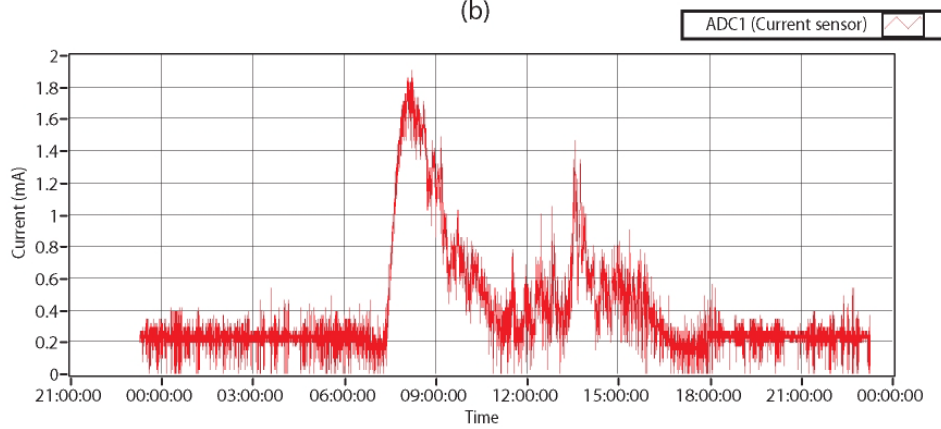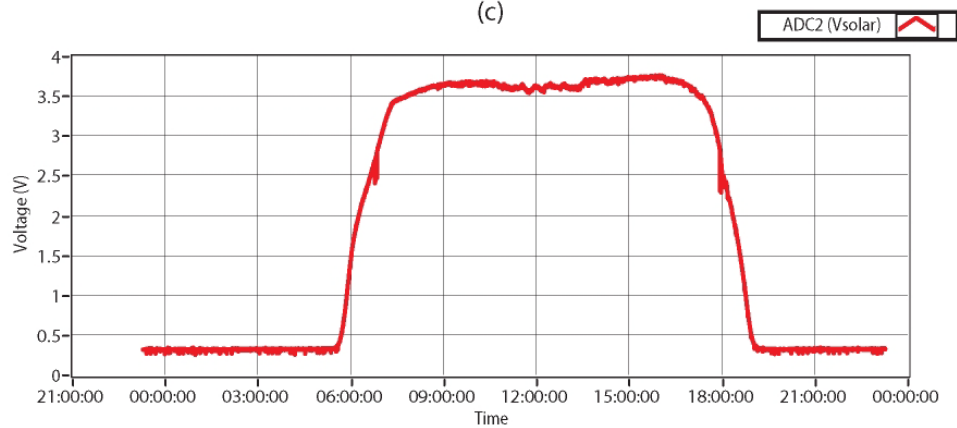
Figure 7.13: Data collected over a 24 hour period

85

7.3.1 SEH subsystem performance

The initial SEH prototype was installed and over the following 10 months various improvements were made. Advances were made on the accuracy of the MPPT by using low tolerance resistors. A low voltage shutdown circuit was introduced to prevent the transmission of erroneous data. The purpose of the implemented low voltage shutdown circuitry is extensively detailed in section 8.2. The battery-less SEH system's performance was considerably enhanced by these improvements. The SEH subsystem proved to be self-sustained operating autonomously over the entire period of evaluation.

The power output from the SEH subsystem into the supercapacitors is shown in Figure 7.14 over a 24 hour, one week and 3 month periods in (a), (b) and (c) respectively. The power transfer into the SEH supercapacitors was calculated with the current sense circuitry. A 0.1Ω current sense resistor together with the MAX9938 with a 100V/V gain were used. The MAX9938 is a precision current sense amplifier that produces an output voltage with reference to the measured current through the 0.1Ω resistor. Schematic details are included in Appendix A.

Through information on the power output from the SEH subsystem, the acquired energy over a defined period could be calculated. The collected energy is the integral of the continuous power curve $P(t)$ over a time frame T_a to T_b as given by (7.5) (Alippi & Galperti, 2008).

$$E = \int_{T_a}^{T_b} P(t)dt \qquad (7.5)$$

Due to the discrete nature of the power output data presented in Figure 7.14, discrete integration was performed on the sampled data. The discrete integration function in LabVIEW® was used to calculate the daily collected energy as given by the discrete summation in (7.6) (Jewett & Serway, 2008).

$$E = \left| \sum_{i=1}^{n} P(t_i)\Delta_i \right| \qquad (7.6)$$

where each term of the sum is the area of a rectangle with height equal to the function $P(t_i)$ at the distinguished sampled point as given by i, and where n is the total number of samples and $\Delta_i = t_i - t_{i-1}$.
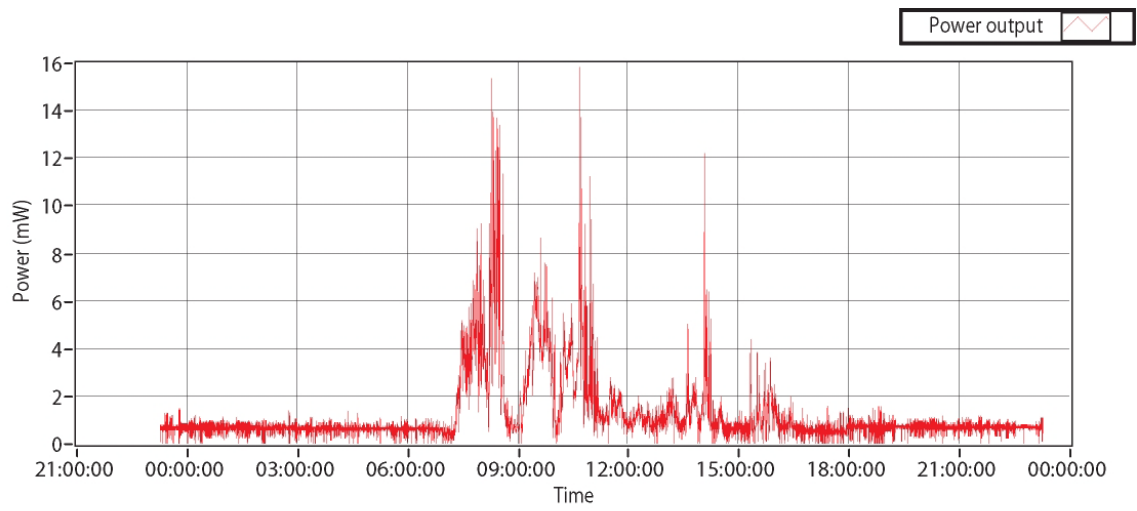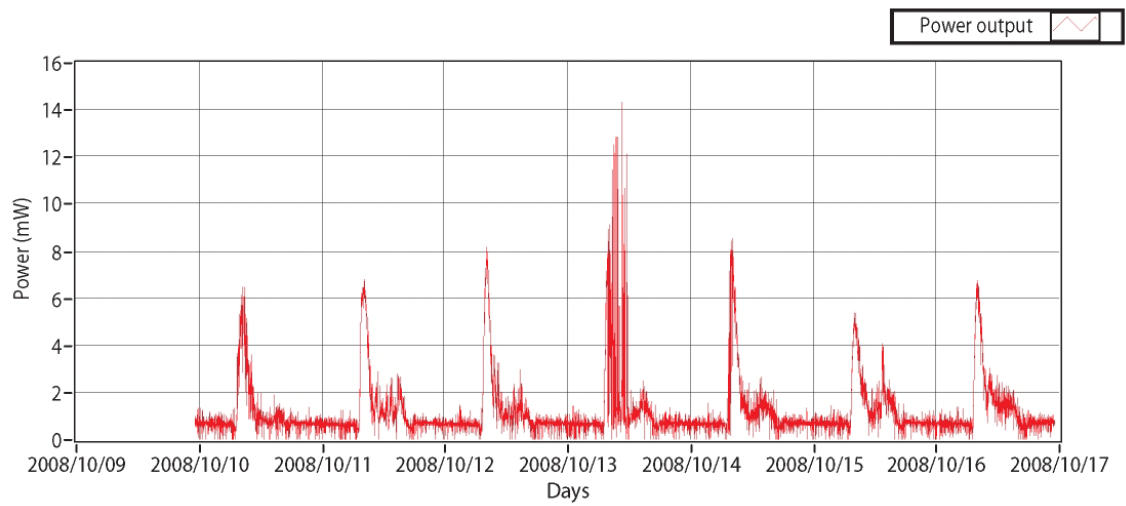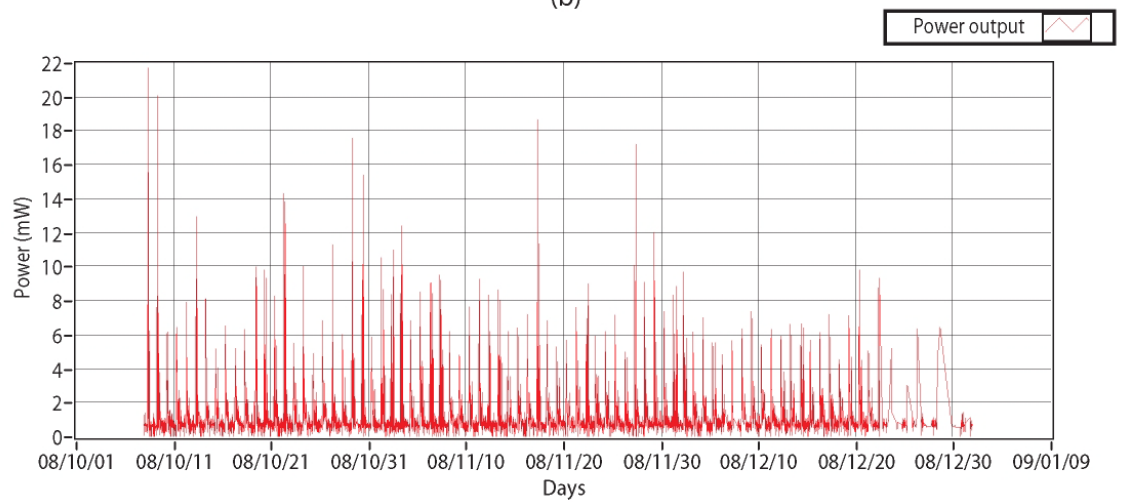
Figure 7.14: Power into supercapacitor

The daily collected energy (E) was calculated by the LabVIEW® integral function for Figure 7.14 (a) totalling 42.17J, where $n = 34560$. Since data samples were collected every 2.5s, that amounted to 24 samples per minute and a total of 34560 (24x60x24) samples over the 24 hour period. Figure 7.15 shows the daily collected energy plotted over a 75 day span. The energy was harvested by the SEH subsystem with the experimental setup described in Figure 7.10. Low daily collected energy is evident on days such as 6 and 7 December 2008. High temperatures were experienced inside the enclosure on those particular days. Checking the weather history also confirmed high ambient temperatures (Windguru, 2009). The low daily generated energy is a result of the inefficiency of the solar panel at high temperature as detailed in section 5.5.1.
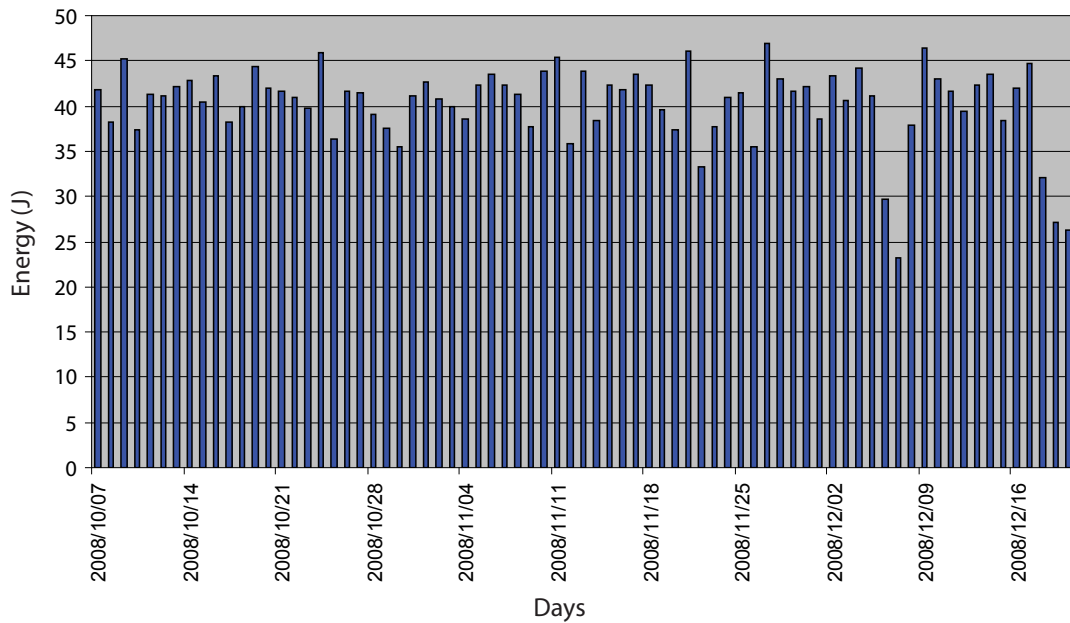
Figure 7.15: Daily collected energy over a 75 day period

The WSM transmitted 10 measurements every 2.5 seconds as discussed in section 7.1. Each transmission consisted of a data payload string of 20 bytes. This amounted to a large number of received data that complicated post processing. An excess of 340 000 data samples were received each day accumulating to over 10 million samples collected each month. Various LabVIEW® programs were written to combine the data and enable more manageable file sizes by scaling the amount of data captured. Another LabVIEW® program extracted relevant data for plotting the respective graphs such as Figures 7.11, 7.12, 7.13 and 7.14. These programs are included in Appendix G.

It is important to note that although the daily acquired energy was calculated externally via post processing with LabVIEW® on a PC, these calculations are simple mathematical functions and could be carried out on the sensor mote. With the knowledge of daily acquired energy, predictions can be made in terms of expected energy levels enabling intelligent and energy efficient routing in larger networks.

7.4 Hybrid power management evaluation

The word hybrid refers to the dual energy harvesting architecture of the power management system described in section 6.3. The system is capable of simultaneously powering the WSM from energy harvested from vibrations and solar radiation as described in chapter 6. This was verified with the experimental setup shown in Figure 7.16.
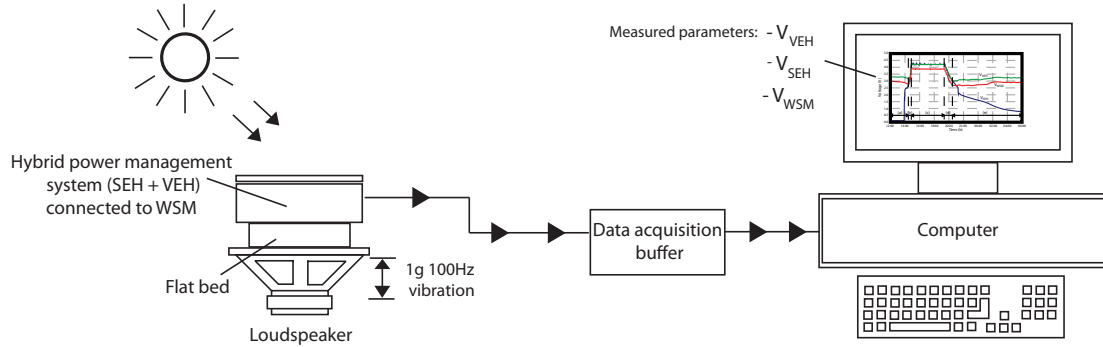
Figure 7.16: Hybrid power management experimental setup

The hybrid energy harvesting prototype was evaluated running a combined experiment of that presented in sections 7.2 and 7.3. The VEH subsystem was subjected to the reference vibration of 10m/s^2 at 100Hz and the SEH subsystem to available sunlight through the laboratory window. Output voltages of both subsystems, V_{SEH} and V_{VEH}, together with the sensor mote voltage (V_{WSM}) were collected over 18 hours. The voltages were buffered and sampled with the PCI 730 data acquisition card from Eagle Technologies (2003) at 1 minute intervals. The PCI 730 is a 16 channel, 100kHz ADC data acquisition card.

Figure 7.17 shows the parallel operation of the SEH and VEH subsystems both supplying power to the WSM. Due to the operating characteristics of the VEH subsystem explained in section 6.5, no power can be supplied to the WSM between the regulated output pulses. Since the voltages were sampled at fixed 1 minute intervals with the data acquisition card, V_{VEH} and V_{WSM} would at times be measured between the regulated output pulses acquiring a lower voltage reading than that of measurements done on the output pulses. A moving average was applied to the data of both V_{VEH} and V_{WSM} in Figure 7.17 to smooth out short-term fluctuations and highlight longer-term trends in the data.

The graphs in Figure 7.17 are divided into intervals (a) through (e) for explanatory purposes. The experiment is started at (a) operating solely on vibration with the SEH storage capacitor completely discharged. Towards the end of (a), V_{SEH} increases due to sunlight exposure. Interval (b) reveals the dual contribution of energy to the WSM from both subsystems as voltages V_{SEH} and V_{VEH} rise equally. During time period (c) the SEH capacitor is fully charged and supplies the majority of the energy to the WSM. Interval (d) shows the parallel discharge of the SCA consequent to decreasing solar radiation. The discharging curves of V_{SEH} and V_{VEH} are almost identical, confirming that the hybrid system powers the WSM together. During interval (e), the SCA voltage decreases to 3V, causing
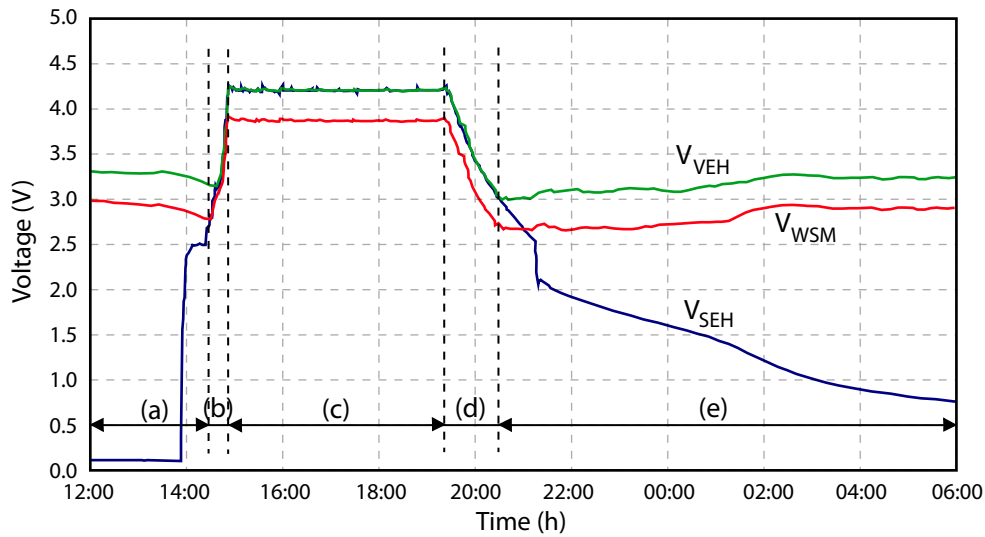
Figure 7.17: Hybrid operation

the system to fall back on the VEH subsystem.

For the evaluation of the hybrid experimental setup detailed in Figure 7.16, the size of the SEH supercapacitor was decreased to 0.22F. This was done to demonstrate the switch-over between both subsystems in a shorter time frame since the smaller supercapacitor stored less energy. For field deployment the value of the SEH supercapacitor would be much larger, with a typical value depending on the application. In the case of the present prototype design, the supercapacitors had a combined series value of 35F.

7.5 Summary

This chapter discussed the performance of both the VEH and SEH subsystems individually as well as together in a hybrid fashion. Subjected to a reference vibration of 10m/s^2 at 100Hz, the VEH subsystem could sustain an operational duty-cycle of 1.1%. The SEH subsystem performed well over the last 6 months due to the alterations mentioned. In the time of deployment, the voltage across the supercapacitor (V_{cap}) on average maintained a minimum of 2.7V. The prototype as a hybrid solution performed as expected powering the WSM with a seamless transition between respective subsystems.

Chapter 8

Conclusions

8.1   General conclusions

Methods to harvest available energy from the environment and the high voltage power transformer were examined. A hybrid prototype design consisting of two subsystems has been successfully implemented which demonstrated the feasibility of operating a WSM without using batteries. The system was capable of simultaneously harvesting energy from vibration and solar ambient power sources allowing self-sustained operation.

Potential types of energy reservoirs for the mote such as supercapacitors and batteries were investigated. Limitations with battery powered designs such as restricted charge cycles, operating life and complex charging circuitry hindered previous designs from truly autonomous operation. The proposed system featured no batteries and was therefore not constrained to any such limitations. Supercapacitors as an alternative energy storage device were implemented.

Upon the completion of the main objectives as detailed in section 1.3, a low cost and feasibly sized power management prototype was developed that allowed sustained sensor mote operation. The SEH subsystem was optimised by introducing MPPT as discussed in section 6.6.2. The VEH subsystem was optimised by tuning the piezoelectric cantilever to resonate at the fundamental vibration frequency as detailed in section 4.6.

The optimised prototype was capable of harvesting sufficient energy from either the SEH or the VEH subsystems individually to sustain the WSM at a minimum operating duty-cycle of 1.1% as described in section 7.2.1. The VEH subsystem therefore not only assisted in the continual operation of the system, but created diversity that ensured true autonomous operation in the event of failure of any input sources.

The energy harvesting, monitoring and controlling of the power management system were done completely independent of the WSM. This enabled the power management system to harvest and store available energy irrespective of whether the WSM was in a low-power, sleep or shutdown state. The size of the overall system was primarily dependent on the power demand from the WSM. The average power of the WSM is a function of it's operating duty-cycle. Smaller supercapacitors can be used if the specific application required less frequent monitoring.

Designing a generic energy harvesting power management solution proved challenging as each application had diverse requirements and conditions with the availability of multiple options of environmental energy to power the WSM. The transducer for energy conversion together with the energy storage device must be tailored to the specific application. This was especially true for vibration energy harvesting as it was crucial to harvest energy at the fundamental vibration frequency to achieve maximum power output as detailed in section 4.6.

The modular architecture of the proposed system allowed expandability to incorporate additional energy harvesting sources. This feature enabled the system to be utilised in various applications with minimal alterations to the present design.

Although the daily acquired energy was calculated via post processing as detailed in section 7.3.1, the calculations could be carried out on the sensor mote. With the knowledge of information such as the daily acquired energy, average and peak power consumptions and the rate of charge of the supercapacitors, predictions could be made on a network level in terms of expected energy levels of each sensor mote. From this intelligent energy efficient routing protocols could be implemented for larger networks.

8.2   Problems encountered

The methods and techniques for low power energy harvesting are considerably different from that of medium to high power energy harvesting systems. With low power energy harvesting systems the choice of every component is vitally important in terms of power consumption as the load or WSM typically consumes less than 1mW on average as confirmed in section 7.1. In medium to high power energy harvesting systems the thought of introducing a component consuming an additional 20mA has little effect on the performance of the overall system. However, such a component in a low power system can hinder the performance and efficiency of such a system.

The power management system experienced difficulty charging the SEH supercapacitors properly. The problem arose every time the supply voltage of the WSM dropped below the lower threshold of 1.8V. Tests revealed that the microprocessor still operated down to around 1.5V but not the radio transceiver of the mote. Each morning the voltage would rise across

the SEH supercapacitors as would be expected owing to increased solar radiation on the panel but struggled to charge beyond 1.9V and only effectively increased when subjected to direct sunlight at midday. This was due to a continuous 20mA current being drawn by the WSM. The relatively high current consumption level suggested similar current levels when the WSM was in constant receive mode. However, this was unlikely due to the nature of the program operating on the WSM as detailed in section 7.1.

It is believed that the problem existed due to incorrect initialisation of the transceiver by the microcontroller, because the problem would be rectified once the reset button was pressed on the mote. A problem that was originally thought to be a hardware issue was found to be software related. To prevent this situation from recurring, a low voltage hardware shutdown was implemented to force the WSM into shutdown mode when the supply voltage dropped below 1.8V. The WSM was only enabled when a threshold of 2V was reached.

The post processing of a large number of data sets posed a real challenge as described in section 7.3.1. More than 340 000 data samples were received every day and over 10 million every month. Conventional applications such as Microsoft® Office Excel were simply not adequate to process such large data sets. LabVIEW® programs were written that enabled more manageable data file sizes. Additional programs performed functions such as extracting and converting of relevant data for post processing.

8.3   Proposed future work and recommendations

Further enhanced system performance can be obtained by improving efficiencies of the VEH and SEH subsystems, currently around 48% and 40% respectively. Overall system performance could be enhanced in several areas such as investigating different switching regulators, PCB layouts, lowering the user defined voltages and utilising ultra-low power components.

To harvest every available joule of energy, the accuracy of the MPPT can be improved by implementing non-standard valued precision resistors in the photo resistor section and comparator circuitry. Intelligent MPPT can be investigated to allow effective operation with various solar panels that are capable of adapting according to changing temperatures and internal changes of the solar panels over time. A major area for improvement is the rectifier stage in the VEH subsystem due to the large loss of power. New techniques need to be researched to efficiently transfer energy through the bridge rectifier.

As a future design thought, it might be considered to implement a dual supercapacitor array in the SEH subsystem. This feature would allow the system to automatically switch between larger supercapacitors when ample sunlight is available and smaller supercapacitors when subjected to successive overcast and low light conditions. When switched to the smaller supercapacitors, the average supply voltage would increase much faster allowing for more consecutive transmissions.

Other harvesting techniques can also be investigated that could contribute to the overall harvesting system. Energy harvesting techniques such as capacitive and inductive coupling to the high voltage transmission lines might be considered. Due to the proper grounding of the outer tank of the transformer, little magnetic flux exists on the outside except where the transmission lines enter the transformer. Electromagnetic energy harvesting can also be investigated. Although values for output power are typically much lower than that of piezoelectric energy harvesters, electromagnetic energy harvesting is not constrained to a narrow band of frequencies for optimal power generation. This can be useful especially due to vibration frequency variations around the transformer as described in section 4.4.

Contrary to challenges of designing an energy harvesting system capable of efficiently extracting, storing and transferring harvested energy to the load, is the issue of adapting harvesting aware power management for communication scheduling and routing. It is important to develop techniques capable of adapting the performance and power consumption of the WSM in response to variations in harvested energy. Such techniques could include monitoring the rate of charge from energy stored in the energy reservoirs. The duty-cycle of the WSM can then be dynamically adjusted according to the ratio of charge and available energy. From this, intelligent decisions can be made on a network level to optimise the amount of collected data and time intervals of transmissions with respect to total available energy in the network.

Sensor networks are envisioned to operate autonomously by harvesting available energy in their surrounding environments while executing intricate, consistent tasks maintenance-free. It is anticipated that current research relating to self-sustained wireless sensor systems is an emerging area of future research. Concepts such as energy harvesting open the way to application fields previously unattainable and expanding sensor network deployment even further.

References

Advanced Cerametrics Incorporated, 2009, *Energy harvesting evaluation system*, URL `http://www.advancedcerametrics.com/` [4 June 2007].

Alippi, C. & Galperti, C., 2008, *An adaptive system for optimal solar energy harvesting in wireless sensor network nodes*, IEEE Transactions on Circuits and Systems I, 55(6):1742–1750.

Ang, R., Tan, Y. & Panda, S., 2007, *Energy harvesting for autonomous wind sensor in remote area*, Proceedings of the 33rd Annual IEEE Industrial Electronics Society Conference (IECON '07), 1:2104–2109.

Arch Rock, 2008, URL `http://www.archrock.com/` [17 June 2009].

Bartoletti, C., Desiderio, M., Di Carlo, D., Fazio, G., Muzi, F., Sacerdoti, G. & Salvatori, F., 2004, *Vibro-acoustic techniques to diagnose power transformers*, IEEE Transactions on Power Delivery, 19(1):221–229.

Bharathidasan, A. & Ponduru, V.A.S., 2003, *Sensor networks: An overview*, IEEE Potentials, 22(2):20–23.

Biggs, J., 2007, *Hands on with horizon fuel cells*, URL `http://www.crunchgear.com/2007/10/03/hands-on-with-horizon-fuel-cells/` [3 October 2007].

Buric, M., Kusic, G., Clark, W. & Johnson, T., 2006, *Piezo-electric energy harvesting for wireless sensor networks*, Proceedings of the Annual IEEE Wireless and Microwave Technology Conference (WAMICON '06), 1:1–5.

Cap-XX, 2008, *Cap-XX: Digital power for the next generation of mobile devices*, URL `http://www.cap-xx.com/` [9 September 2007].

CENELEC, 2009, *European Committee for Electro Technical Standardization*, URL `http://www.cenelec.eu/Cenelec/Homepage.htm` [26 May 2009].

Chalard, L., Helal, D., Verbaere, L., Wellig, A. & Zory, J., 2007, *Wireless sensor networks devices: Overview, issues, state-of-the-art and promising technologies*, ST Journal of Research, 4(1):4–8.

Chao, L., Tsui, C. & Ki, W., 2007, *A batteryless vibration-based energy harvesting system for ultra low power ubiquitous applications*, Proceedings of the IEEE International Symposium on Circuits and Systems (ISCAS 2007), 1:1349–1352.

Cooper Electronic Technologies, 2005, *Design considerations in selecting aerogel supercapacitors*, URL `http://www.cooperet.com/` [19 May 2006].

CPUT, 2008, *Cape Peninsula University of Technology*, URL `http://www.cput.ac.za/` [26 May 2009].

Crompton, T.R., 2000, *Battery reference book*, 3rd edition, Newnes.

Crossbow® Technology, 2009, *Next generation wireless technology*, URL `http://www.xbow.com/` [17 June 2009].

Cuadras, A., Gasulla, M., Ghisla, A. & Ferrari, V., 2006, *Energy harvesting from pzt pyroelectric cells*, Proceedings of the IEEE Instrumentation and Measurement Technology Conference (IMTC 2006), 1:1668–1672.

Discenzo, F.M. & Chung, D., 2006, *Power scavenging enables maintenance-free wireless sensor nodes*, Proceedings of the NECSI International Conference on Complex Systems, 1:1–8.

Duncan, J., 2005, *A Global Maximum Power Point Tracking DC-DC Converter*, Master's thesis, Massachusetts Institute of Technology (MIT), Cambridge.

Eagle Technologies, 2003, *Data acquisition hardware and software*, URL `http://www.eagledaq.com/` [2 June 2008].

Enocean®, 2009, *Self-powered wireless sensors*, URL `http://www.enocean.com/` [17 June 2009].

Flipsen, S., 2005, *Alternative power sources for portables & wearables*, Technical Report 1.2005, Delft University of Technology, Netherlands.

Fogiel, M., 2004, *Basic Electricity*, USA: Research & Education Association.

Guilar, N., Chen, A., Kleeburg, T. & Amirtharajah, R., 2006, *Integrated solar energy harvesting and storage*, Proceedings of the 2006 IEEE International Symposium on Low Power Electronics and Design (ISLPED'06), 1:20–24.

Harper, D., 2009, *Energy*, Online Etymology Dictionary, URL `http://dictionary.reference.com/browse/energy` [07 May 2008].

Horizon Fuel Cell Technologies, 2007, URL `http://www.horizonfuelcell.com/` [3 June 2008].

Huang, T., Jiang, J., Hsiao, Y. & Chen, C., 2005, *Maximum power tracking for photovoltaic power systems*, Tamkang Journal of Science and Engineering, 8:147–153.

IEEE Computer Society, 2007, *IEEE Standard: 802.15.4™a-2007*, Technical report, The Institute of Electrical and Electronics Engineers, Inc., 3 Park Avenue, New York, NY.

James, E., Tudor, M., Beeby, S., Harris, N., Glynne-Jones, P., Ross, J. & White, N., 2004, *An investigation of self-powered systems for condition monitoring applications*, Sensors and Actuators, 110:171–176.

Jansen, A., Fridstedt, S. & Weernink, A., 2000, *A batteryless remote control for volvo, results of a feasibility study*, Proceedings of the ISATA Conference on Automotive Technology and Automation, 1:1–9.

Jensen, J. & Sørensen, B., 1984, *Fundamentals of energy storage*, Canada: John Wiley & Sons, Inc.

Jewett, J.W. & Serway, R.A., 2008, *Physics for scientists and engineers*, volume 1, 7th edition, Cengage Learning EMEA.

Jiang, X., Polastre, J. & Culler, D., 2005, *Perpetual environmentally powered sensor networks*, Proceedings of the 4th International Symposium on Information Processing in Sensor Networks (IPSN '05), 1:463–468.

Kansal, A., Hsu, J., Zahedi, S. & Srivastava, M.B., 2007, *Power management in energy harvesting sensor networks*, ACM Transactions on Embedded Computing Systems (TECS), 6(32):1–9.

Lal, A., Duggirala, R. & Li, H., 2005, *Pervasive power: a radioisotope-powered piezoelectric generator*, IEEE Pervasive Computing, 4(1):53–61.

Leland, E.S., Lai, E.M. & Wright, P.K., 2004, *A self-powered wireless sensor for indoor environmental monitoring*, Proceedings of the Wireless Networking & Communications Symposium (WNCG 2004), 1:1–5.

Masti, R.S., Desmet, W. & Heylen, W., 2004, *On the influence of core laminations upon power transformer noise*, Proceedings of the International Conference on Noise & Vibration Engineering (ISMA 2004), 1:3851–3862.

Matsuo, O., Matsuo, H., Tuji, M., Kobayashi, K. & Sekine, Y., 2006, *A hybrid type dc-dc converter with new control strategy for a micro-fuel cell power supply system*, Proceedings of the 28th Annual International Telecommunications Energy Conference (INTELEC '06), 1:1–6.

Maxim Integrated Products, 2009, *Innovation delivered*, URL `http://www.maxim-ic.com/` [16 August 2006].

Maxwell Technologies, 2009, *Power series ultracapacitors*, URL `http://www.maxwell.com/ultracapacitors` [20 September 2009].

Mechefske, C.K., 1995, *Correlating power transformer tank vibration characteristics to winding looseness*, Insight, 37(8):599–604.

Mehraeen, S., Jagannathan, S. & Corzine, K., 2008, *Energy harvesting using piezoelectric materials and high voltage scavenging circuitry*, Proceedings of the IEEE International Conference on Industrial Technology (ICIT 2008), 1:1–8.

Midya, P., Krein, P.T., Turnbull, R.J., Reppa, R. & Kimball, J., 1996, *Dynamic maximum power point tracker for photovoltaic applications*, Proceedings of the 27th Annual IEEE Power Electronics Specialists Conference (PESC), 2:1710–1716.

Morias, R., Fernandes, M.A., Matos, S.G., Serodio, C., Ferreira, P. & Reis, M., 2008, *A zigbee multi-powered wireless acquisition device for remote sensing applications in precision viticulture.*, Computers and Electronics in Argiculture, 62:94–106.

Ottman, G.K., Bhatt, H.H.A.C. & Lesieutre, G.A., 2002, *Adaptive piezoelectric energy harvesting circuit for wireless remote power supply*, IEEE Transactions on Power Electronics, 17:669–676.

Panasonic, 1998, *Solar cells technical handbook '98/99*, Technical report, Matsushita Battery Industrial Co. Ltd.

Park, C. & Chou, P.H., 2006, *Ambimax: Autonomous energy harvesting platform for multi-supply wireless sensor nodes*, Proceedings of the Sensor and Ad Hoc Communications and Networks (SECON), 1:168–177.

Peebles, P.Z. & Giuma, T.A., 1991, *Principles of Electrical Engineering*, McGraw-Hill.

Penella, M. & Gasulla, M., 2007, *A review of commercial energy harvesters for autonomous sensors*, Proceedings of the 2007 IEEE Instrumentation and Measurement Technology Conference (IMTC 2007), 1:1–5.

Polastre, J., Szewczyk, R. & Culler, D., 2005, *Telos: Enabling ultra-low power wireless reseach*, Proceedings of the 4th International Symposium on Information Processing in Sensor Networks 2005 (IPSN 2005), 1:364–369.

Pottie, G.J. & Kaiser, W., 2000, *Wireless integrated network sensors*, Communications of the ACM, 43(5):51–58.

PowerFilm®, 2009, *The world's leading thin film photovoltaics*, URL http://www.powerfilmsolar.com/ [6 August 2006].

Priya, S., 2007, *Advances in energy harvesting using low profile piezoelectric transducers*, Journal of Electroceramics, 19(1):165–182.

Raghunathan, V., Kansal, A., Hsu, J., Friedman, J. & Srivastava, M., 2005, *Design considerations for solar energy harvesting wireless embedded systems*, Proceedings of the 4th International Symposium on Information Processing in Sensor Networks 2005 (IPSN 2005), 1:457–462.

Roundy, S., Otis, B.P., Chee, Y. & Rabaey, J.M., 2004, *Power sources for wireless sensor networks*, in *Proceedings of the 1st European Workshop on Wireless Sensor Networks (EWSN)*, Berlin, Germany.

Roundy, S., Otis, B.P., Chee, Y., Rabaey, J.M. & Wright, P., 2003, *A 1.9GHz RF transmit beacon using environmentally scavenged energy*, Proceedings of the 2003 IEEE International Symposium on Low Power Electronics and Devices (ISLPED '03), 1:1–6.

Roundy, S.J., 2003, *Energy Scavenging for Wireless Sensor Nodes with a Focus on Vibration to Electricity Conversion*, Ph.D. thesis, The University of California, Berkeley.

Sample, A., Yeager, D., Smith, J., Powledge, P. & Mamishev, A., 2006, *Energy harvesting in RFID systems*, Proceedings of the International Conference on Actual Problems of Electron Devices Engineering, 1:445–449.

Sentilla™, 2009, *Energy management solutions*, URL `http://www.sentilla.com/` [17 June 2009].

Shenck, N. & Paradiso, J., 2001, *Energy scavenging with shoe-mounted piezoelectrics*, IEEE Micro, 21(3):30–42.

Shengchang, J., Yongfen, L. & Yanming, L., 2006, *Research on extraction technique of transformer core fundamental frequency vibration based on olcm*, IEEE Transactions on Power Delivery, 21(4):1981–1988.

Shu, Y. & Lien, I., 2006, *Analysis of power output for piezoelectric energy harvesting systems*, Smart Materials and structures, 15:1499–1512.

Simjee, F. & Chou, P.H., 2006, *Everlast: Long-life, supercapacitor-operated wireless sensor node*, Proceedings of the 2006 IEEE International Symposium on Low Power Electronics and Design (ISLPED'06), 197–202.

Taneja, J., Jeong, J. & Culler, D., 2008, *Design, modeling, and capacity planning for microsolar power sensor networks*, Proceedings of the 2008 International Conference on Information Processing in Sensor Networks (IPSN '08), 407–418.

Taylor, G.W., 1985, *Piezoelectricity*, Taylor & Francis.

Texas Instruments, 2009, URL `http://www.ti.com/` [4 June 2007].

Thomson, W.T., 1972, *Theory of Vibration with Applications*, Eaglewood Cliffs: Prentice-Hall.

Thurston, M.O., 2003, *Battery technology handbook*, 2nd edition, New York: Marcel Dekker, Inc.

TinyOS, 2004, *An open source OS for the networked sensor regime*, URL `http://www.tinyos.net/` [24 June 2009].

Vijayaraghavan, K. & Rajamani, R., 2007, *Active control based energy harvesting for battery-less wireless traffic sensors*, Proceedings of the American Control Conference (ACC '07), 1:3106–3111.

Williams, C. & Yates, R., 1995, *Analysis of a micro-electric generator for microsystems*, IEEE Transactions on Solid-state Sensors and Actuators, 1:369–372.

Windguru, 2009, *Weather forecasts*, URL `http://www.windguru.com/` [25 June 2009].

Wu, W., Chen, Y., Chen, Y., Wang, C. & Chen, Y., 2006, *Smart wireless sensor network powered by random ambient vibrations*, Proceedings of the IEEE International Conference on Systems, Man and Cybernetics (SMC '06), 4:2701–2708.

Yafaoui, A., Wu, B. & Cheng, R., 2007, *Implementation of maximum power point tracking algorithm for residential photovoltaic systems*, Proceedings of the 2nd Canadian Solar Buildings Conference, 1:1 – 6.

Appendix A

Power management system schematics

SOLAR_VOUT_4.2V

C2
47uF
+

C3
100N

R10
390K

R9
180K

C5
47uF
+

D1
open

L1
22uH

Input to regulator

U2
MAX1676

9 LX
10 OUT
4 CLSEL
1 FB
6 SHDN
3 LBO
8 GND
7 BATT
2 LBI
5 REF

LBO

R8
0 Ohm

C4
100N

R12
200

R11
open

R7
0 Ohm

Regulator
shutdown

U1
LTC1440

7 V+
8 OUT
1 GND
2 V−
3 IN+
4 IN−
5 HYST
6 REF

SOLAR_VOUT_4.2V

VCC_LOAD

D2
TS4148

C9
35F
+

VCAP

D3
TS4148

PIEZO_VOUT_4.2V

C1
1uF

R5
390

R6
1M

R18
2M7

R4
560K

R3
VTB8440B
2M7

1.18VREF

PHOTO_RES

R1
5M6

R2
2M2

ADC2

C7
1uF
+

VSOLAR

Supercapacitor Energy Reservoir:
2x 22F parallel combination

Low battery detection not used: Ground LBI and LBO

Theoretical output of 4.2V for MAX1676: R9 = 180k, R10 = 390k

Title: Solar Energy Harvesting (SEH) Subsystem

Number: 201009846

Rev: 1.3

Drawn by: DJ de V

Sheet 1 of 3

Size: A4

Date: April 2009

Filename:

102

PIEZO_VOUT_4.2V

C8
100uF

R14 390K
R13 150K

U3 TPS76301
OUT 5
FB 4
GND 2
IN 1
EN 3

Values of R13 and R14 produce 4.2V output

C8 (1uF – 100uF) decrease C8 enable extended on–time
but longer duration between on–cycles

U5 MAX6433
LBO 4
GND 2
VDD 5
LTHIN 3
HTHIN 1

R15 3M9
R16 82K
R17 560K

C6 470uF
C10 470uF

U4 MB2S RECTIFIER
AC 1
AC 2
+ 3
- 4

PIEZO_PIN1
PIEZO_PIN2

MAX6433
R15 = 4M for theoretical calculation
Vtriphigh = 5V
Vtriplow = 4.3V

Cstore = C10 +C6
(Size dependent on application
increase total capacitance for longer operation)

Title	Vibration Energy Harvesting (VEH) Subsystem		
Size A4	Number 201009846	Rev	1.3
Date	April 2009	Drawn by	DJ de V
Filename		Sheet 2 of 3	

Force mote shutdown at 1.8V

MOTE_RESET

Values of R19, R20, R21
produce Vht = 1.95V and Vlt = 1.79V

VCC_LOAD

R19 3M3
R20 220K
R21 1M5

U6
MAX6433
VDD 5
LTHIN 3
HTHIN 1
LBO 4
GND 2

J1
1 GND
2 VSOLAR
3 PHOTO_RES
4 GND
4-pin Solar connector

J2
1 PIEZO_PIN1
2 PIEZO_PIN2
2-pin piezo connector

J3
1 2
3 4
5 6
7 8
9 10
10-pin header
VCC_LOAD
ADC0
ADC1
ADC2
GND

J4
1 GND
2 VCAP
2-pin supercapacitor connector

J5
1 2
3 4
5 6
6-pin header
MOTE_RESET

Scale Vcap due to 1.5Vref of MSP430

VCAP
R23 2M2
R24 2M2
R25 2M2
ADC0

SOLAR_VOUT_4.2V

R22 0.1 Ohm

U7
MAX9938
RS- 4
RS+ 5
OUT 3
GND 2
GND 1
ADC1

Title Low voltage shutdown and current sense circuitry
Size A4
Number 201009846
Rev 1.3
Date April 2009
Drawn by DJ de V
Filename
Sheet 3 of 3

Appendix B

Component selection

B.1 Low voltage shutdown resistor selection

As described in section 7.3.1, a low voltage shutdown circuit was introduced to prevent the transmission of erroneous data. Further explanations on the purpose for such an implementation are detailed in section 8.2. The WSM was disabled when a bottom threshold supply voltage of 1.8V was reached and would only be enabled when the supply voltage across the the WSM increased above 2V. This was achieved by incorporating the MAX6433 low-power battery monitor. It featured user-adjustable threshold voltages and required no dedicated supply pin.

The values for the resistor divider network were calculated according to steps detailed in the datasheet of the MAX6433 (Maxim Integrated Products, 2009). A total resistance value, given by equation (B.1) with a maximum of 5MΩ should be chosen for the three resistors R19, R20 and R21 as detailed in Appendix A:

$$R_{TOTAL} = R19 + R20 + R21 \tag{B.1}$$

R21 was calculated according to equation (B.2):

$$R21 = \frac{V_{REF} \times R_{TOTAL}}{V_{TRIPHIGH}} \tag{B.2}$$

where $V_{REF} = 585$mV.

R_{TOTAL} was chosen as 5MΩ and $V_{TRIPHIGH}$ was selected as 2V and substituted into equation (B.2):

R21 $= \frac{(585 \times 10^{-3}) \times (5 \times 10^6)}{2}$

$\quad = 1.46\text{M}\Omega \approx 1.5\text{M}\Omega$

R20 was calculated based on equation (B.3):

$$R20 = \frac{V_{REF} \times R_{TOTAL}}{V_{TRIPLOW}} - R21 \tag{B.3}$$

where $V_{REF} = 615\text{mV}$.

$V_{TRIPLOW}$ was selected as 1.8V. The values of R_{TOTAL}, R19 and $V_{TRIPLOW}$ were substituted in equation (B.3) from where R20 was calculated accordingly:

R20 $= \frac{(615 \times 10^{-3}) \times (5 \times 10^6)}{1.8} - (1.5 \times 10^6)$

$\quad = 208\text{k}\Omega \approx 220\text{k}\Omega$

R19 was calculated referring back to equation (B.1):

R19 $= R_{TOTAL} - R20 - R21$

$\quad = (5 \times 10^6) - (220 \times 10^3) - (1.5 \times 10^6)$

$\quad = 3.28\text{M}\Omega \approx 3.3\text{M}\Omega$

Therefore, with the resistor-divider network of R19 as 3.3MΩ, R20 as 220kΩ and R21 as 1.5MΩ the MAX6433 disabled the WSM at voltages below 1.8V and only enabled the WSM again when the supply voltage increased above 2V.

B.2 VEH subsystem resistor selection

It was necessary to implement a buffer in the VEH subsystem so C_{in} could charge as explained in section 6.5. This was achieved by introducing the MAX6433 dual-level user-adjustable comparator. The upper trip voltage ($V_{TRIPHIGH}$) was selected to be 5V and the lower trip voltage ($V_{TRIPLOW}$) 4.3V. The choices regarding the selected voltages were discussed in section 6.5.

R17 was calculated according to equation (B.2) with R_{TOTAL} selected as 4.5MΩ, V_{REF} as 585mV and $V_{TRIPHIGH}$ as 5V:

$R17 = \frac{(585 \times 10^{-3}) \times (4.5 \times 10^6)}{5}$

$ = 526.5\text{k}\Omega \approx 560\text{k}\Omega$

R16 was calculated based on equation (B.3) with $V_{TRIPLOW}$ as 4.3V and V_{REF} as 615mV:

$R16 = \frac{(615 \times 10^{-3}) \times (4.5 \times 10^6)}{4.3} - (560 \times 10^3)$

$ = 83.6\text{k}\Omega \approx 82\text{k}\Omega$

Using equation (B.1) R15 was calculated:

$R15 = R_{TOTAL}$ - R16 - R17

$ = (4.5 \times 10^6) - (82 \times 10^3) - (560 \times 10^3)$

$ = 3.858\text{M}\Omega \approx 3.9\text{M}\Omega$

Therefore, with the resistor-divider network of R15 as 3.9MΩ, R16 as 82kΩ and R17 as 560kΩ the MAX6433 enabled the LDO regulator at a voltage of 5V and disabled the regulator at 4.3V as detailed in sections 6.5 and 7.2.

The TPS76301 low-power LDO step-down voltage regulator was selected for the VEH subsystem as detailed in section 6.5. To coincide with the SEH subsystem's output voltage a resistor-divider network was connected on the output of the TPS76301 to produce the defined 4.2V. Investigating the datasheet of the TPS76301, the output voltage (V_O) is given by equation (B.4) (Texas Instruments, 2009).

$$V_O = 0.995 \times V_{ref} \times \left(1 + \frac{R14}{R13}\right) \tag{B.4}$$

where V_{ref} is 1.192V (typical internal reference voltage) and 0.995 is a constant used to center the load regulator (1%).

The recommended design procedure was to choose R13 equal to 169kΩ to set the divider current at 7μA. A standard resistance value of 150kΩ was selected for R13. Resistor R14 was calculated by reworking equation (B.4) and substituting V_O, V_{ref} and R13:

$R14 = \left(\frac{V_O}{0.995 \times V_{ref}} - 1\right) \times R13$

$ = \left(\frac{4.2}{0.995 \times 1.192} - 1\right) \times (150 \times 10^3)$

$ = 381.18\text{k}\Omega \approx 390k\Omega$

To calculate the deviated output voltage from the original 4.2V, V_O was calculated by substituting R13 as 150kΩ and R14 as 390kΩ into equation (B.4).

$$V_O = 0.995 \times (1.192) \times \left(1 + \frac{(390 \times 10^3)}{(150 \times 10^3)}\right)$$
$$= 4.269\text{V}$$

Therefore, when using the standard resistance values for R13 and R14 as indicated, a slightly higher output voltage of 4.269V can be expected from the TPS76301 instead of the defined 4.2V.

B.3   SEH subsystem resistor selection

To charge the supercapacitors of the SEH subsystem to the defined 4.2V, it was necessary to connect a resistor-divider network on the output of the MAX1676 step-up DC-DC converter from the pins V_{OUT} to FB to GND. The output voltage was determined by equation (B.5) detailed in the MAX1676 datasheet (Maxim Integrated Products, 2009):

$$R10 = R9 \left[\left(\frac{V_{OUT}}{V_{REF}}\right) - 1\right] \tag{B.5}$$

where $V_{REF} = 1.3$V and R9 < 260kΩ.

A standard resistance value of 180kΩ was chosen for R9. This was substituted in equation (B.5) with $V_{OUT} = 4.2$V and $V_{REF} = 1.3$V and yielded:

$$R10 = (180 \times 10^3) \left[\left(\frac{4.2}{1.3}\right) - 1\right]$$
$$= 401 \text{ k}\Omega \approx 390k\Omega$$

To calculate the deviated output voltage from the original 4.2V, V_{OUT} was calculated by substituting R9 as 180kΩ and R10 as 390kΩ into equation (B.5).

$$V_{OUT} = (V_{REF}) \left[\left(\frac{R10}{R9}\right) + 1\right]$$
$$= (1.3) \left[\left(\frac{390 \times 10^3}{180 \times 10^3}\right) + 1\right]$$
$$= 4.12\text{V}$$

An output voltage from the MAX1676 of 4.12V can therefore be expected instead of the defined 4.2V when using the standard resistance values for R9 and R10 as indicated.

Since the voltage across the supercapacitors was capable of a maximum of 4.2V, the voltage had to be scaled when measuring the supercapacitor voltage through the ADC port on the WSM. The ADC port could read a full-scale voltage 1.5V determined by the internal 1.5V reference on the microcontroller. The voltage was scaled using a high impedance resistor-divider network to minimise power dissipation. The supercapacitor voltage was scaled with a ratio of 0.33 using three 2.2MΩ resistor in series:

$$\text{Scaling ratio} = \frac{(2.2 \times 10^6)}{(2.2 \times 10^6) \times 3} = 0.3\dot{3}$$

Therefore a maximum supercapacitor voltage of 4.2V will be scaled down to 1.4V such that the maximum ADC input voltage of 1.5V was not exceeded.

Appendix C

Prototype bill of materials

Count	ComponentName	RefDes	PatternName	Value	Description	Source	Stock no.
1	4PIN_CONNECTOR	J1	4PIN_CONNECTOR		4-pin connector	Store room	
2	2PIN_CONNECTOR	J2	2PIN_CONNECTOR		2-pin connector	Store room	
		J4					
1	10PIN_HEADER	J3	10PIN_HEADER		10-pin header	Store room	
1	6PIN_HEADER	J5	6PIN_HEADER		6-pin header	Store room	
1	CAP_0805	C1	SMT_0805	1uF	Ceramic SMT 0805	Store room	
2	CAP_0805	C3	SMT_0805	100N	Ceramic SMT 0805	Store room	
		C4					
1	CAP_TANTALUM	C7	CASE_B	1uF	Tantalum SMT Case B	Mantech (Farnell)	
2	CAP_TANTALUM	C2	CASE_B	47uF	Tantalum SMT Case B	Mantech (Farnell)	
		C5					
1	CAP_TANT_SMT_CA	C8	CASE_B	100uF	Tantalum SMT 6.3V Case B	RS components	547-9502
2	CAP_TANT_SMT_CA	C6	CASE_D	470uF	Tantalum SMT 6.3V Case D	RS components	547-9518
		C10					
1	CURRENT_RES	R 22	CURRENT_RES	0.1 Ohm	Current sense resistor SMT 1206	RS components	219-936
2	DIODE_SMT	D2	SMB	TS4148	Low power signal diode SMT 0805	Mantech (Farnell)	815-0206
		D3					
1	LTC1440	U1	8-LEAD_S8		LTC1440CMS8 (MSOP package)	Avnet/RS components	
1	MAX1676	U2	MAX1676_PCAD2002		MAX1676EUB (10 uMAX)	CST electronics	
2	MAX6433	U5	SOT-23_5		MAX6433EUR (SOT23-5)	CST electronics	
		U6					
1	MAX9938	U7	SOT-23_5		MAX9938HEUK SOT23-5 (100 V/V gain)	CST electronics	
1	MB2S RECTIFIER	U4	MB2S_Rectifier		SMT Bridge rectifier (MB6S)	RS components	652-7501
1	PHOTO_RES	R 3	CONNECTOR 1	VTB8440B	Photodiode VTB8440B (Light sensor)	Mantech	
1	POT	R 6	JUMPER_PCAD2002	1M	Pot SMT 4mm sealed	RS components	100-1240
1	POWER_INDUCTOR	L1	POWER_INDUCTOR	22uH	SMT Inductor (VLCF5020T-220MR58)	RS components	614-2841
2	RES_0805	R 7	SMT_0805	0 Ohm	1% tolerance SMT 0805	Mantech	
		R 8					
1	RES_0805	R 21	SMT_0805	1M5	1% tolerance SMT 0805	Store room	
4	RES_0805	R 2	SMT_0805	2M2	1% tolerance SMT 0805	Store room	
		R 23					
		R 24					
		R 25					
1	RES_0805	R 18	SMT_0805	2M7	1% tolerance SMT 0805	Store room	
1	RES_0805	R 19	SMT_0805	3M3	1% tolerance SMT 0805	Store room	
1	RES_0805	R 15	SMT_0805	3M9	1% tolerance SMT 0805	Store room	
1	RES_0805	R 1	SMT_0805	5M6	1% tolerance SMT 0805	Store room	
1	RES_0805	R 16	SMT_0805	82k	1% tolerance SMT 0805	Store room	
1	RES_0805	R 13	SMT_0805	150k	1% tolerance SMT 0805	Store room	
1	RES_0805	R 9	SMT_0805	180k	1% tolerance SMT 0805	Store room	
1	RES_0805	R 12	SMT_0805	200	1% tolerance SMT 0805	Mantech	
1	RES_0805	R 20	SMT_0805	220k	1% tolerance SMT 0805	Store room	
1	RES_0805	R 5	SMT_0805	390	1% tolerance SMT 0805	Store room	
2	RES_0805	R 10	SMT_0805	390k	1% tolerance SMT 0805	Store room	
		R 14					
2	RES_0805	R 4	SMT_0805	560k	1% tolerance SMT 0805	Store room	
		R 17					
1	RES_0805	R 11	SMT_0805	open	1% tolerance SMT 0805	n/a	
1	SCH_DIODE	D1	CASE_B	open		n/a	
1	SUPERCAP_CONNECTOR	C9	PIEZO	35F	Panasonic supercaps (2x 70F in series)	Mantech (Farnell)	
1	TPS76301	U3	DBV_TI_PCAD2002		SOT-23 (DBV) package	RS components	517-3096
1	MP3-37				Solar panel	PowerFilm	
1	PCFC-100				Piezoelectric cantilever	Advanced Cerametrics	

Figure C.1: Prototype bill of materials

Appendix D

Power management system PCB layout

Drill Table			
Hole Dia (mm)	Symbol	Quantity	Plated
0.600	+	19	Yes
1.000	×	26	Yes
2.500	Y	2	Yes

TOP SILK LAYER
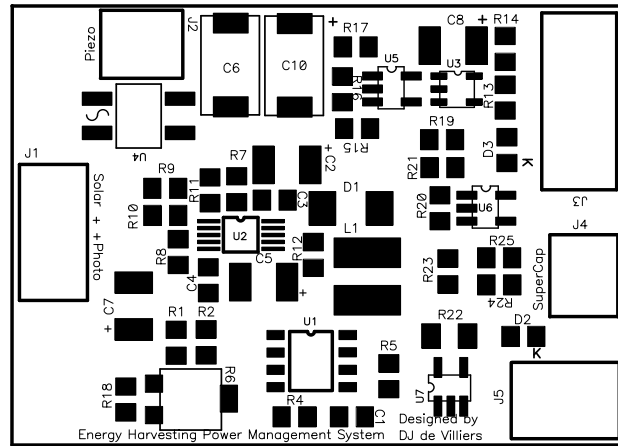
TOP TRACE LAYER
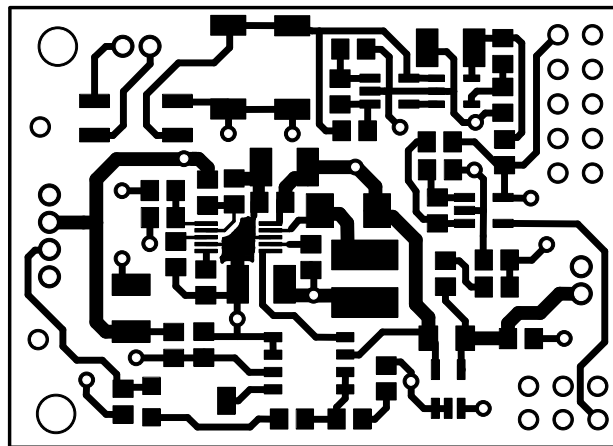
BOTTOM TRACE LAYER

Appendix E

Prototype PCB model
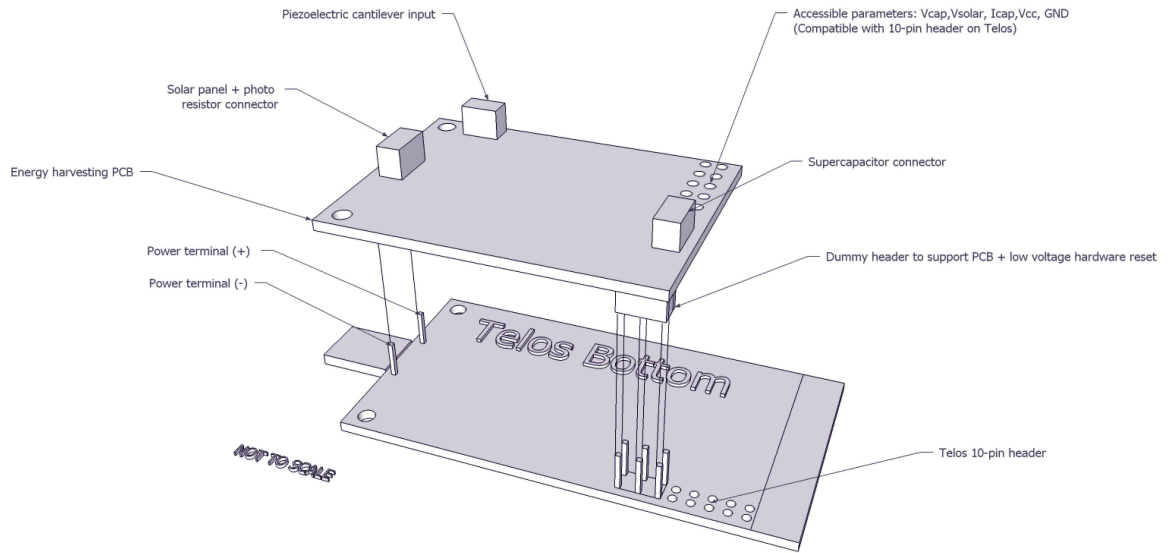
(a)
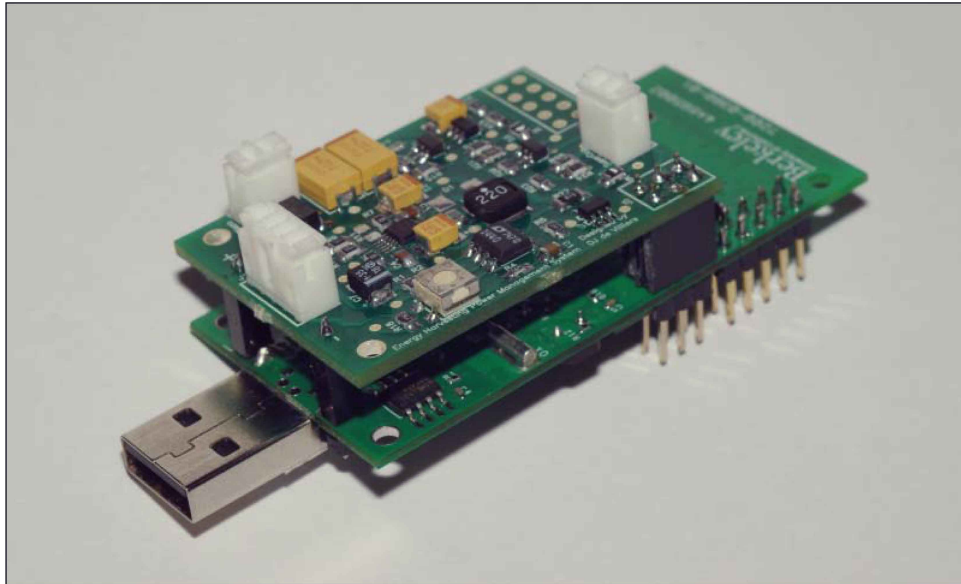
(b)

Figure E.1: (a) Prototype CAD representation (b) Final PCB integration on WSM

Appendix F

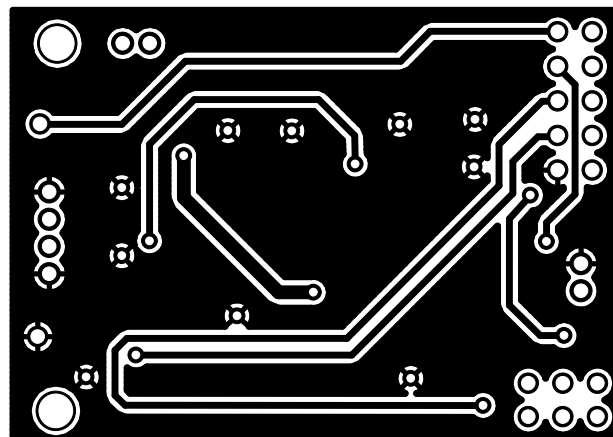# Application program source code

The application program is a modified version of the original program *Oscilloscope* available with TinyOs. The program was modified to read external values from ADC channels 0, 1 and 2. The source code is detailed in `OscilloscopeC.nc`, `OscilloscopeAppC.nc`, `ODemoSensorC.nc`, `ExternalSensor1ParC.nc` and `ExternalSensor1ParP.nc`

```
/**
 * Modified Oscilloscope demo application with ADC0, ADC1 and ADC2 enabled
 * for external sensors.
 *
 *
 *
 */
#include "Timer.h"
#include "Oscilloscope.h"

module OscilloscopeC
{
  uses {
    interface Boot;
    interface SplitControl as RadioControl;
    interface AMSend;

    interface Timer<TMilli>;

    interface Read<uint16_t> as MyPhotoRead;
    interface Read<uint16_t> as MyVoltageRead;
    interface Read<uint16_t> as MyTSRRead;
    interface Read<uint16_t> as MyTemperatureRead;
    interface Read<uint16_t> as MyHumidityRead;
    interface Read<uint16_t> as MyExternalSensor1Read;
    interface Read<uint16_t> as MyExternalSensor2Read;
    interface Read<uint16_t> as MyExternalSensor3Read;

    interface Leds;
  }
}
implementation
{
  message_t sendbuf;
  bool sendbusy = FALSE;

  /* Current local state - interval, version and accumulated readings */
  oscilloscope_t local;

  uint8_t reading; /* 0 to NREADINGS */

  /* When we head an Oscilloscope message, we check it's sample count. If
     it's ahead of ours, we "jump" forwards (set our count to the received
     count). However, we must then suppress our next count increment. This
     is a very simple form of "time" synchronization (for an abstract
     notion of time). */
  bool suppress_count_change;

  // Use LEDs to report various status issues.
  void report_problem() {  }
  void report_sent() {  }
  void report_received() {  }


// ---------------------------
  void startTimer() {
    call Timer.startPeriodic(local.interval);
    reading = 0;
  }


// ---------------------------
// At boot start periodic timer
  event void Boot.booted() {
    local.interval = DEFAULT_INTERVAL;
    local.id = TOS_NODE_ID;
    startTimer();
  }

// ----------------------------------------
// When radio is on, compile packet and send
  event void RadioControl.startDone(error_t error) {
    if (!sendbusy && sizeof local <= call AMSend.maxPayloadLength())
      {
        //memcpy(call AMSend.getPayload(&sendbuf), &local, sizeof local);
        memcpy(call AMSend.getPayload(&sendbuf, sizeof(local)), &local, sizeof local);
```

117

```
          if (call AMSend.send(AM_BROADCAST_ADDR, &sendbuf, sizeof local) == SUCCESS)
            sendbusy = TRUE;
//          call Leds.led2Toggle();
      }
    if (!sendbusy)
      report_problem();
    local.count++;
    reading = 0;
  }


// ---------------------------------
  event void RadioControl.stopDone(error_t error) {
  }


// --------------------------------------------------------
  /* At each sample period:
     - if local sample buffer is full, send accumulated samples
     - read next sample
  */
// When timer fires and readings buffer is full turn on radio.
  event void Timer.fired() {
    if (reading == NREADINGS)
      {
//turn on radio, send data, turn off radio
    if (call RadioControl.start() != SUCCESS)
      report_problem();
//        call Leds.led0Toggle();
      }

    if(reading == 3)
      {
      if (call MyExternalSensor3Read.read() != SUCCESS)
        report_problem();
      }

    else if(reading == 4)
      {
      if (call MyExternalSensor2Read.read() != SUCCESS)
        report_problem();
      }

    else if(reading == 5)
      {
      if (call MyExternalSensor1Read.read() != SUCCESS)
        report_problem();
      }

    else if(reading == 6)
      {
      if (call MyHumidityRead.read() != SUCCESS)
        report_problem();
      }

    else if(reading == 7)
      {
      if (call MyPhotoRead.read() != SUCCESS)
        report_problem();
//      call Leds.led1Toggle();
      }
    else if(reading == 8)
      {
      if (call MyTSRRead.read() != SUCCESS)
        report_problem();
      }
    else if(reading == 9)
      {
      if (call MyTemperatureRead.read() != SUCCESS)
        report_problem();
      }
      else
      {
      if (call MyVoltageRead.read() != SUCCESS)
        report_problem();
      }
```

```
  }

// -----------------------------------------------------
// Once packet is sent over the radio, shutdown radio.
   event void AMSend.sendDone(message_t* msg, error_t error) {
      if (error == SUCCESS)
        report_sent();
      else
        report_problem();

      sendbusy = FALSE;

      if (call RadioControl.stop() != SUCCESS)
        report_problem();

   }


// -----------------------------------------------------
   event void MyVoltageRead.readDone(error_t result, uint16_t data) {
      if (result != SUCCESS)
        {
      data = 0xffff;
      report_problem();
        }
      local.readings[reading++] = data;
   }

// -----------------------------------------------------
   event void MyPhotoRead.readDone(error_t result, uint16_t data) {
      if (result != SUCCESS)
        {
      data = 0xffff;
      report_problem();
        }
      local.readings[reading++] = data;
   }

// -----------------------------------------------------
   event void MyTSRRead.readDone(error_t result, uint16_t data) {
      if (result != SUCCESS)
        {
      data = 0xffff;
      report_problem();
        }
      local.readings[reading++] = data;
   }

// -----------------------------------------------------
   event void MyTemperatureRead.readDone(error_t result, uint16_t data) {
      if (result != SUCCESS)
        {
      data = 0xffff;
      report_problem();
        }
      local.readings[reading++] = data;
   }

// -----------------------------------------------------
   event void MyHumidityRead.readDone(error_t result, uint16_t data) {
      if (result != SUCCESS)
        {
      data = 0xffff;
      report_problem();
        }
      local.readings[reading++] = data;
   }

// -----------------------------------------------------
   event void MyExternalSensor1Read.readDone(error_t result, uint16_t data) {
      if (result != SUCCESS)
        {
      data = 0xffff;
      report_problem();
        }
```

```
      local.readings[reading++] = data;
  }

// --------------------------------------------------------
  event void MyExternalSensor2Read.readDone(error_t result, uint16_t data) {
    if (result != SUCCESS)
      {
    data = 0xffff;
    report_problem();
      }
      local.readings[reading++] = data;
  }

// --------------------------------------------------------
  event void MyExternalSensor3Read.readDone(error_t result, uint16_t data) {
    if (result != SUCCESS)
      {
    data = 0xffff;
    report_problem();
      }
      local.readings[reading++] = data;
  }

}
```

```
/*
 * Copyright (c) 2006 Intel Corporation
 * All rights reserved.
 *
 * This file is distributed under the terms in the attached INTEL-LICENSE
 * file. If you do not find these files, copies can be found by writing to
 * Intel Research Berkeley, 2150 Shattuck Avenue, Suite 1300, Berkeley, CA,
 * 94704.  Attention:  Intel License Inquiry.
 */

/**
 * Oscilloscope demo application. Uses the demo sensor - change the
 * new DemoSensorC() instantiation if you want something else.
 *
 * See README.txt file in this directory for usage instructions.
 *
 * @author David Gay
 */
configuration OscilloscopeAppC { }
implementation
{
  components OscilloscopeC, MainC, ActiveMessageC,
    new TimerMilliC(), new ODemoSensorC() as Sensor,
    new AMSenderC(AM_OSCILLOSCOPE), LedsC;

  OscilloscopeC.Boot -> MainC;
  OscilloscopeC.RadioControl -> ActiveMessageC;
  OscilloscopeC.AMSend -> AMSenderC;

  OscilloscopeC.Timer -> TimerMilliC;
  OscilloscopeC.MyVoltageRead -> Sensor.VoltageRead;
  OscilloscopeC.MyPhotoRead -> Sensor.PhotoRead;
  OscilloscopeC.MyTSRRead -> Sensor.TSRRead;
  OscilloscopeC.MyTemperatureRead -> Sensor.TemperatureRead;
  OscilloscopeC.MyHumidityRead -> Sensor.HumidityRead;
  OscilloscopeC.MyExternalSensor1Read -> Sensor.ExternalSensor1Read;
  OscilloscopeC.MyExternalSensor2Read -> Sensor.ExternalSensor2Read;
  OscilloscopeC.MyExternalSensor3Read -> Sensor.ExternalSensor3Read;

  OscilloscopeC.Leds -> LedsC;


}
```

```nc
/*
 * Copyright (c) 2005-2006 Arch Rock Corporation
 * All rights reserved.
 *
/**
 * DemoSensorC is a generic sensor device that provides a 16-bit
 * value. The platform author chooses which sensor actually sits
 * behind DemoSensorC, and though it's probably Voltage, Light, or
 * Temperature, there are no guarantees.
 *
 * This particular DemoSensorC on the telosb platform provides a
 * voltage reading, using VoltageC.
 *
 * To convert from ADC counts to actual voltage, divide this reading
 * by 4096 and multiply by 3.
 *
 * @author Gilman Tolle <gtolle@archrock.com>
 * @version $Revision: 1.4 $ $Date: 2006/12/12 18:23:45 $
 *
 * HamamatsuS1087ParC is a driver for a photosynthetically-active
 * radiation sensor available on the telosb platform.
 * HamamatsuS10871TsrC is a driver for a total solar radiation sensor
 * available on the telosb platform.
 * SensirionSht11C is a top-level access component for the Sensirion
 * SHT11 model humidity and temperature sensor, available on the
 * telosb platform. Because this component represents one physical
 * device, simultaneous calls to read temperature and humidity will be
 * arbitrated and executed in sequential order. Feel free to read both
 * at the same time, just be aware that they'll come back
 * sequentially.
 */

generic configuration ODemoSensorC()
{
  provides interface Read<uint16_t> as PhotoRead;
  provides interface Read<uint16_t> as VoltageRead;
  provides interface Read<uint16_t> as TSRRead;
  provides interface Read<uint16_t> as TemperatureRead;
  provides interface Read<uint16_t> as HumidityRead;
  provides interface Read<uint16_t> as ExternalSensor1Read;
  provides interface Read<uint16_t> as ExternalSensor2Read;
  provides interface Read<uint16_t> as ExternalSensor3Read;
}
implementation
{
  components new HamamatsuS1087ParC() as PhotoSensor;
  components new VoltageC() as VoltageSensor;
  components new HamamatsuS10871TsrC() as TSRSensor;
  components new SensirionSht11C() as TemperatureSensor;
  components new ExternalSensor1ParC() as ExternalSense1;
  components new ExternalSensor2ParC() as ExternalSense2;
  components new ExternalSensor3ParC() as ExternalSense3;

  PhotoRead = PhotoSensor;
  VoltageRead = VoltageSensor;
  TSRRead = TSRSensor;
  TemperatureRead = TemperatureSensor.Temperature;
  HumidityRead = TemperatureSensor.Humidity;
  ExternalSensor1Read = ExternalSense1;
  ExternalSensor2Read = ExternalSense2;
  ExternalSensor3Read = ExternalSense3;
}
```

```
/*
 * Copyright (c) 2005-2006 Arch Rock Corporation
 * All rights reserved.
 *
 * Redistribution and use in source and binary forms, with or without
 * modification, are permitted provided that the following conditions
 * are met:
 * - Redistributions of source code must retain the above copyright
 *   notice, this list of conditions and the following disclaimer.
 * - Redistributions in binary form must reproduce the above copyright
 *   notice, this list of conditions and the following disclaimer in the
 *   documentation and/or other materials provided with the
 *   distribution.
 * - Neither the name of the Arch Rock Corporation nor the names of
 *   its contributors may be used to endorse or promote products derived
 *   from this software without specific prior written permission.
 *
 * THIS SOFTWARE IS PROVIDED BY THE COPYRIGHT HOLDERS AND CONTRIBUTORS
 * ``AS IS'' AND ANY EXPRESS OR IMPLIED WARRANTIES, INCLUDING, BUT NOT
 * LIMITED TO, THE IMPLIED WARRANTIES OF MERCHANTABILITY AND FITNESS
 * FOR A PARTICULAR PURPOSE ARE DISCLAIMED.  IN NO EVENT SHALL THE
 * ARCHED ROCK OR ITS CONTRIBUTORS BE LIABLE FOR ANY DIRECT, INDIRECT,
 * INCIDENTAL, SPECIAL, EXEMPLARY, OR CONSEQUENTIAL DAMAGES
 * (INCLUDING, BUT NOT LIMITED TO, PROCUREMENT OF SUBSTITUTE GOODS OR
 * SERVICES; LOSS OF USE, DATA, OR PROFITS; OR BUSINESS INTERRUPTION)
 * HOWEVER CAUSED AND ON ANY THEORY OF LIABILITY, WHETHER IN CONTRACT,
 * STRICT LIABILITY, OR TORT (INCLUDING NEGLIGENCE OR OTHERWISE)
 * ARISING IN ANY WAY OUT OF THE USE OF THIS SOFTWARE, EVEN IF ADVISED
 * OF THE POSSIBILITY OF SUCH DAMAGE
 */

/**
 * * ExternalSensor1ParP is a driver for any external sensor
 * connected to ADC0 available through header pin 3 on the 10-pin expansion connector
on the telosb platform.
 *
 * @author Gilman Tolle <gtolle@archrock.com>
 * @version $Revision: 1.5 $ $Date: 2007/04/13 21:46:18 $
 */

generic configuration ExternalSensor1ParC() {
  provides interface DeviceMetadata;
  provides interface Read<uint16_t>;
  provides interface ReadStream<uint16_t>;
}
implementation {
  components new AdcReadClientC();
  Read = AdcReadClientC;

  components new AdcReadStreamClientC();
  ReadStream = AdcReadStreamClientC;

  components ExternalSensor1ParP;
  DeviceMetadata = ExternalSensor1ParP;
  AdcReadClientC.AdcConfigure -> ExternalSensor1ParP;
  AdcReadStreamClientC.AdcConfigure -> ExternalSensor1ParP;
}
```

```
/*
 * Copyright (c) 2005-2006 Arch Rock Corporation
 * All rights reserved.
 *
 * Redistribution and use in source and binary forms, with or without
 * modification, are permitted provided that the following conditions
 * are met:
 * - Redistributions of source code must retain the above copyright
 *   notice, this list of conditions and the following disclaimer.
 * - Redistributions in binary form must reproduce the above copyright
 *   notice, this list of conditions and the following disclaimer in the
 *   documentation and/or other materials provided with the
 *   distribution.
 * - Neither the name of the Arch Rock Corporation nor the names of
 *   its contributors may be used to endorse or promote products derived
 *   from this software without specific prior written permission.
 *
 * THIS SOFTWARE IS PROVIDED BY THE COPYRIGHT HOLDERS AND CONTRIBUTORS
 * ``AS IS'' AND ANY EXPRESS OR IMPLIED WARRANTIES, INCLUDING, BUT NOT
 * LIMITED TO, THE IMPLIED WARRANTIES OF MERCHANTABILITY AND FITNESS
 * FOR A PARTICULAR PURPOSE ARE DISCLAIMED.  IN NO EVENT SHALL THE
 * ARCHED ROCK OR ITS CONTRIBUTORS BE LIABLE FOR ANY DIRECT, INDIRECT,
 * INCIDENTAL, SPECIAL, EXEMPLARY, OR CONSEQUENTIAL DAMAGES
 * (INCLUDING, BUT NOT LIMITED TO, PROCUREMENT OF SUBSTITUTE GOODS OR
 * SERVICES; LOSS OF USE, DATA, OR PROFITS; OR BUSINESS INTERRUPTION)
 * HOWEVER CAUSED AND ON ANY THEORY OF LIABILITY, WHETHER IN CONTRACT,
 * STRICT LIABILITY, OR TORT (INCLUDING NEGLIGENCE OR OTHERWISE)
 * ARISING IN ANY WAY OUT OF THE USE OF THIS SOFTWARE, EVEN IF ADVISED
 * OF THE POSSIBILITY OF SUCH DAMAGE
 */

#include "Msp430Adc12.h"

/**
 * ExternalSensor1ParP is a driver for any external sensor
 * connected to ADC0 available through header pin 3 on the 10-pin expansion connector
on the telosb platform.
 *
 * @author Gilman Tolle <gtolle@archrock.com>
 * @version $Revision: 1.5 $ $Date: 2007/04/13 21:46:18 $
 */

module ExternalSensor1ParP {
  provides interface DeviceMetadata;
  provides interface AdcConfigure<const msp430adc12_channel_config_t*>;
}
implementation {

  msp430adc12_channel_config_t config = {
    inch: INPUT_CHANNEL_A0,
    sref: REFERENCE_VREFplus_AVss,
    ref2_5v: REFVOLT_LEVEL_1_5,
    adc12ssel: SHT_SOURCE_ACLK,
    adc12div: SHT_CLOCK_DIV_1,
    sht: SAMPLE_HOLD_4_CYCLES,
    sampcon_ssel: SAMPCON_SOURCE_SMCLK,
    sampcon_id: SAMPCON_CLOCK_DIV_1
  };

  command uint8_t DeviceMetadata.getSignificantBits() { return 12; }

  async command const msp430adc12_channel_config_t* AdcConfigure.getConfiguration() {
    return &config;
  }
}
```

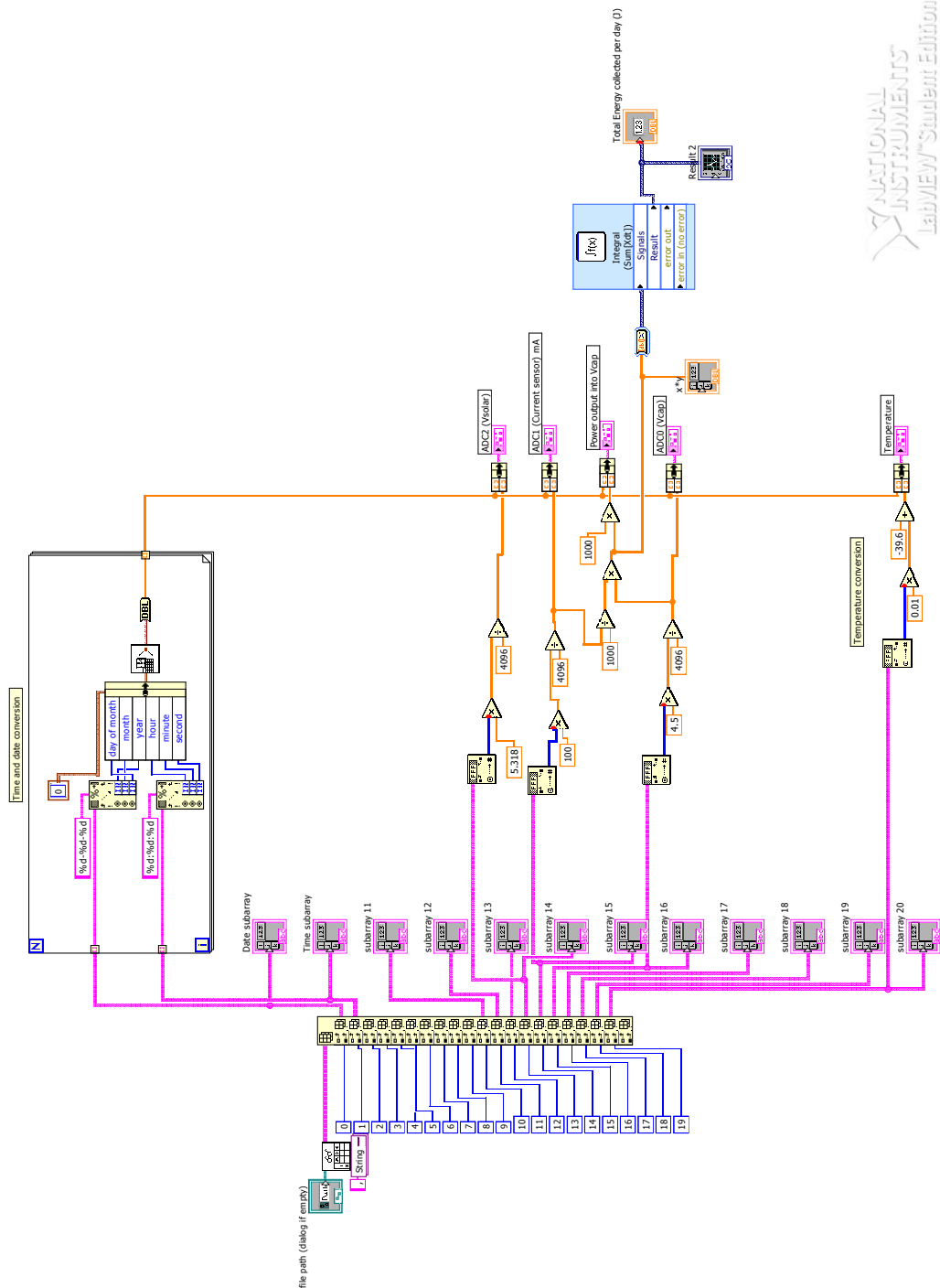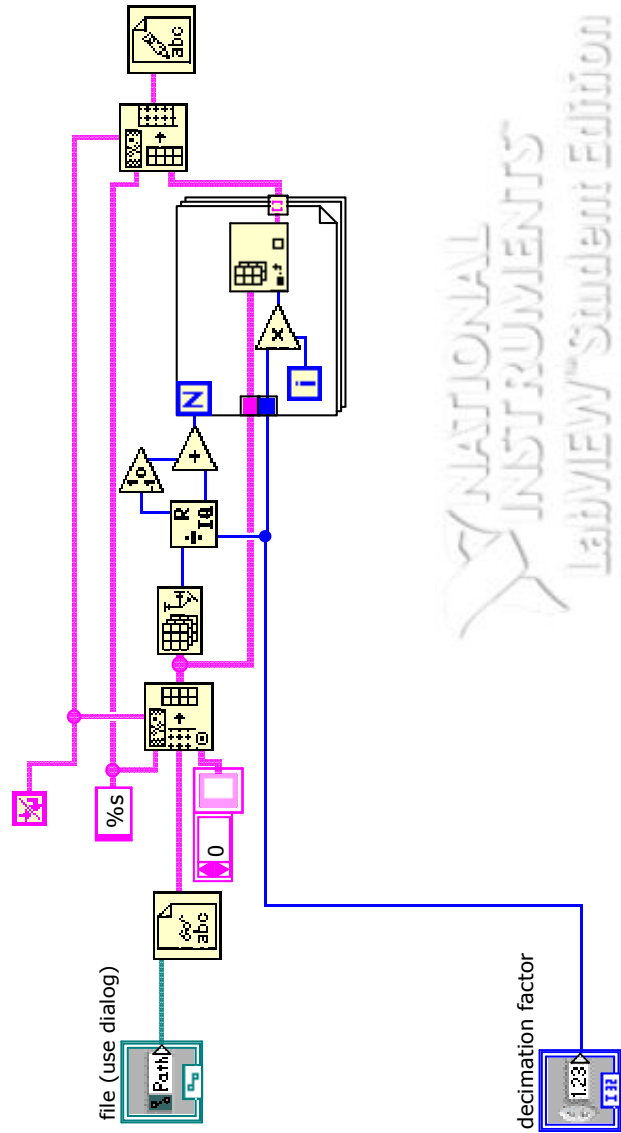# Appendix G

LabVIEW® block diagrams

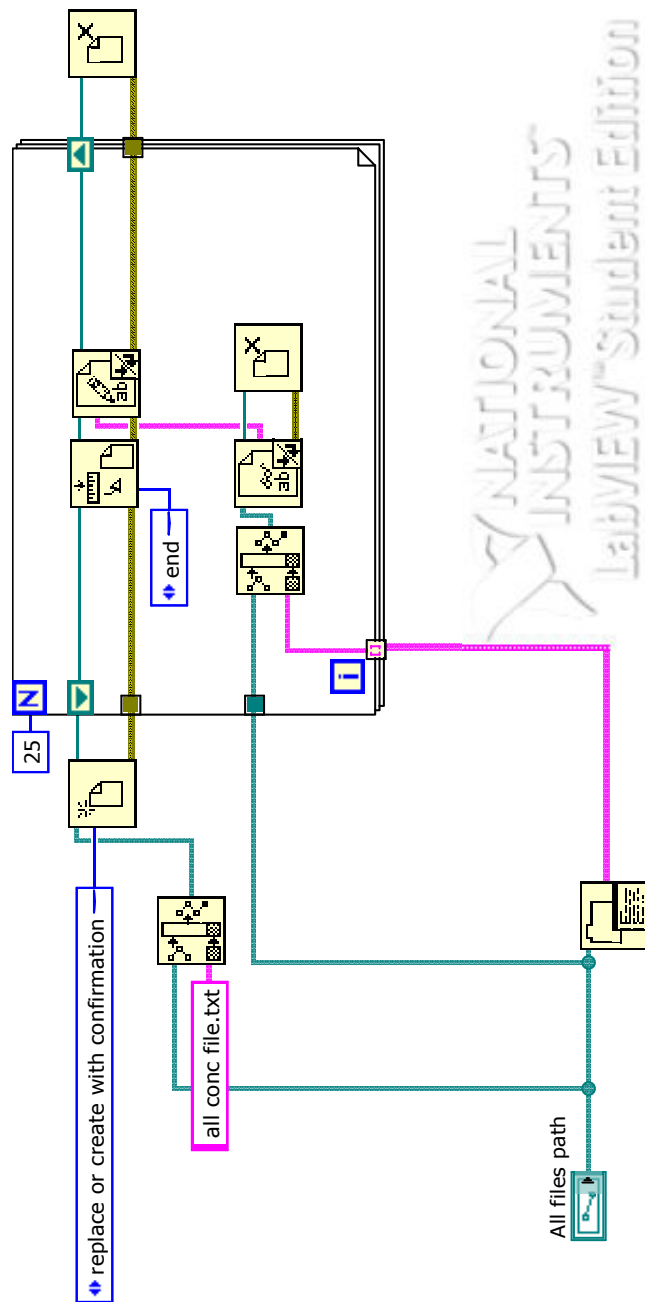Figure G.1: Data extraction from text files

Figure G.2: Decimate data points to reduce file size

Figure G.3: Concatenate data text files